UNIVERSIDADE ESTADUAL DE CAMPINAS

INSTITUTO DE QUÍMICA

GABRIEL FLORIANO COSTA

ON THE ACTIVITY OF COPPER-BASED MATERIALS FOR ELECTROCATALYTIC NITRATE REDUCTION TO AMMONIA

ATIVIDADE DE MATERIAIS DE COBRE PARA A REDUÇÃO ELETROCATALÍTICA DE NITRATO PARA FORMAÇÃO DE AMÔNIA

CAMPINAS

2024

GABRIEL FLORIANO COSTA

ON THE ACTIVITY OF COPPER-BASED MATERIALS FOR ELECTROCATALYTIC NITRATE REDUCTION TO AMMONIA

ATIVIDADE DE MATERIAIS DE COBRE PARA A REDUÇÃO ELETROCATALÍTICA DE NITRATO PARA FORMAÇÃO DE AMÔNIA

Tese de Doutorado apresentada ao Instituto de Química da Universidade Estadual de Campinas como parte dos requisitos exigidos para a obtenção do título de Doutor em Ciências.

Doctor's Thesis presented to the Institute of Chemistry of the University of Campinas as part of the requirements to obtain the title of Doctor in Sciences.

Supervisor: Raphael Nagao de Sousa

O arquivo digital corresponde à versão final da Tese defendida pelo aluno Gabriel Floriano Costa e orientado pelo Prof. Dr. Raphael Nagao de Sousa.

CAMPINAS

2024

Ficha catalográfica
Universidade Estadual de Campinas (UNICAMP)
Biblioteca do Instituto de Química
Simone Luiz Alves - CRB 8/9094

Costa, Gabriel Floriano, 1996-
C823o On the activity of copper-based materials for electrocatalytic nitrate reduction to ammonia / Gabriel Floriano Costa. – Campinas, SP : [s.n.], 2024.

Orientador: Raphael Nagao de Sousa.
Tese (doutorado) – Universidade Estadual de Campinas (UNICAMP), Instituto de Química.

1. Eletroquímica. 2. Eletrocatálise. 3. Nitratos. 4. Cobre. 5. Amônia. I. Sousa, Raphael Nagao de, 1984-. II. Universidade Estadual de Campinas (UNICAMP). Instituto de Química. III. Título.

Informações Complementares

Título em outro idioma: Atividade de materiais de cobre para a redução eletrocatalítica de nitrato para formação de amônia
Palavras-chave em inglês:
Electrochemistry
Electrocatalysis
Nitrates
Copper
Ammonia
Área de concentração: Físico-Química
Titulação: Doutor em Ciências
Banca examinadora:
Raphael Nagao de Sousa [Orientador]
Rene Alfonso Nome Silva
Juliana Ferreira de Brito
Janaina de Souza Garcia
Marcos Roberto de Vasconcelos Lanza
Data de defesa: 05-07-2024
Programa de Pós-Graduação: Química

Identificação e informações acadêmicas do(a) aluno(a)
- ORCID do autor: https://orcid.org/0000-0003-1632-0562
- Currículo Lattes do autor: http://lattes.cnpq.br/6254788887446111

BANCA EXAMINADORA

Prof. Dr. Raphael Nagao de Sousa (Orientador)

Prof. Dr. Rene Alfonso Nome Silva (IQ / Unicamp)

Profa. Dra. Juliana Ferreira de Brito (UNESP)

Profa. Dra. Janaina de Souza Garcia (UFABC)

Prof. Dr. Marcos Roberto de Vasconcelos Lanza (IQSC – USP)

A Ata da defesa assinada pelos membros da Comissão Examinadora, consta no SIGA/Sistema de Fluxo de Dissertação/Tese e na Secretaria do Programa da Unidade.

Este exemplar corresponde à redação final da Tese de Doutorado defendida pelo aluno GABRIEL FLORIANO COSTA, aprovada pela Comissão Julgadora em 5 de julho de 2024.

I dedicate this thesis to the memory of my beloved brother Felipe, whose support and radiant presence inspired and propelled me.

Acknowledgments

Firstly, I thank all my family members, especially my parents Maria José and Carlos for their support throughout my PhD. I deeply thank my life and work partner Maria for being so supportive during my PhD journey, both in the lab routine and daily life. I thank all my friends from Campinas and the ones from Ann Arbor for being essential for a better life-work balance during this PhD.

I thank Prof. Dr. Raphael Nagao from the Institute of Chemistry of the University of Campinas for his thoughtful supervision over the entire PhD and Prof. Dr. Nirala Singh from the University of Michigan for his supervision throughout the research internship in the USA, from July/2022 to June/2023.

I also acknowledge the collaborators of the works presented in this thesis: Dr. Manuel Winkler, Dr. Thiago Mariano, MSc. Maria R. Pinto, MSc. Igor Messias, Dr. João B. S. Júnior, Dr. Itamar Neckel, Dr. Maria F. C. Santos and Prof. Dr. Cláudio F. Tomena.

The São Paulo Research Foundation (FAPESP) is acknowledged for funding this PhD project conducted at the Institute of Chemistry of the University of Campinas, located in Campinas/SP, Brazil from March/2020 to July/2024 through grant number 2019/18847-6. FAPESP is also acknowledged for the Research Internship Abroad from July/2022 to June/2023 conducted at the University of Michigan, in Ann Arbor/MI, USA, funded by grant number 2022/01799-1.

The Coordenação de Aperfeiçoamento de Pessoal de Nível Superior – Brasil (CAPES) – Financial Code 001 is acknowledged for the scholarship from August/2019 to February/2020.

Resumo

O ciclo do nitrogênio está modificado globalmente pelo uso excessivo de fertilizantes na produção de alimentos. Um dos sintomas mais prejudiciais dessa variação é o acúmulo de espécies nitrogenadas reativas no meio ambiente, especialmente o nitrato, a forma mais oxidada das espécies nitrogenadas, sendo um preocupante poluente em águas subterrâneas, rios e lagos. Além disso, a produção de amônia pelo processo de Haber-Bosch é o processo industrial que mais emite dióxido de carbono, devido ao uso de gás natural para obtenção de hidrogênio. Com isso o desenvolvimento de alternativas sustentáveis para produção de amônia é crucial para avançar em direção a um futuro livre de combustíveis fósseis. A redução eletroquímica de nitrato é uma alternativa sustentável tanto para remover nitratos de sistemas aquáticos e águas residuais industriais, quanto para sintetizar amônia com uma menor pegada de carbono. Esta tese tem como objetivo avaliar aspectos relacionados ao catalisador e ao eletrólito na redução eletroquímica de nitrato em materiais à base de cobre. Investigamos cinética e espectroscopicamente como as condições catódicas eletroquímicas para a conversão de nitrato em amônia impactam a estrutura e a composição de um eletrodepósito de Cu/Cu_2O. Combinando a avaliação cinética de catalisadores Cu/Cu_2O pré-reduzidos durante diferentes tempos em comparação com cobre puro, juntamente com espectroscopias Raman e de absorção de raios-X *in situ*, descobrimos que, como o óxido de cobre se reduz durante a redução do nitrato, as vacâncias de oxigênio impulsionam a produção de amônia em sobrepotenciais mais brandos (de −0,6 a −0,77 V vs. SHE), enquanto cobre metálico é ativo a −1,1 V vs. SHE. Usando eletrólito neutro não tamponado, detectamos um aumento no pH do católito de 5,8 para até 12,0, já que a redução do nitrato para amônia envolve o consumo de 8 mols de prótons para cada mol de nitrato. Também investigamos o impacto do pH da solução na redução eletroquímica de nitrato para amônia em cobre dentro de uma faixa de pH de 4,4 a 9,3. Através de experimentos eletroquímicos e medições de espectrometria de massas eletroquímica diferencial, elucidamos como o pH da solução em condições levemente ácidas e básicas modula tanto a taxa de redução de nitrato quanto a distribuição de produtos da reação. Nossos resultados oferecem importantes informações a respeito do papel da escolha dos eletrólitos na modulação dos mecanismos de redução de nitrato, especialmente dentro da faixa crítica de pH de 4,4 a 9,3, contribuindo para um entendimento mais profundo deste importante processo eletrocatalítico.

Abstract

The nitrogen cycle is globally disturbed by the excessive use of fertilizers for food production. One of the most harmful symptoms of such disturbance is the accumulation of reactive nitrogen into the environment, especially nitrate, the most oxidized nitrogenous species, being a serious pollutant in groundwater, rivers, and lakes. Additionally, the ammonia production from Haber-Bosch is the most carbon dioxide-emitting industrial process due to the use of natural gas to obtain hydrogen, and the development of sustainable alternatives for ammonia production is crucial to moving toward an electrified future. The electrochemical nitrate reduction is a sustainable alternative to remove nitrates from aquatic systems and industrial wastewater, as well as to synthesize ammonia with a lower carbon footprint. This work aims to evaluate both catalyst and electrolyte aspects of the nitrate electrochemical reduction on copper-based materials. We kinetically and spectroscopically investigate how electrochemical cathodic conditions for nitrate conversion to ammonia impact the structure and content of Cu/Cu_2O composite. Combining the kinetic evaluation of differently pre-reduced Cu/Cu_2O catalysts compared with pure Cu alongside *in-situ* Raman and X-ray absorption spectroscopies, we found that since copper oxide reduces during nitrate reduction, oxygen vacancies boost ammonia production at lower overpotentials (from −0.6 to −0.77 V *vs.* SHE), while copper itself is active at −1.1 V *vs.* SHE. Using neutral non-buffered electrolyte, we detected an increase in catholyte's pH from 5.8 to up to 12.0, since nitrate reduction to ammonia involves the consumption of 8 moles of protons for each mole of nitrate. We also investigated the impact of the solution pH on the nitrate electrochemical reduction to ammonia on copper catalysts within a pH range of 4.4 to 9.3. Through electrochemical experiments and differential electrochemical mass spectrometry measurements, we elucidate how variation in solution pH at mildly acidic and basic conditions modulate both the rate of nitrate reduction and distribution of reaction products. Our findings provide valuable insights into the role of electrolyte in modulating nitrate reduction mechanisms, particularly within the critical pH range from 4.4 to 9.3, contributing to a deeper understanding of this important electrocatalytic process.

List of Figures

and pure Cu (orange). The results for (a) and (b) were obtained from 10 minutes of potentiostatic electrolysis with the catalyst as WE, graphite rod as CE and Ag/AgCl as RE, electrolyte containing 0.5 mol L^{-1} Na_2SO_4 adding 0.05 mol L^{-1} $NaNO_3$ in the catholyte. Rate orders shown in (c) were extracted from electrolysis under the same conditions as in (a) but with varying $NaNO_3$ concentrations from 0.005 to 0.05 mol L^{-1}. The error bars denote the standard deviation of at least three separate experiments.

Figure 2.4. Cu/Cu_2O *ex-situ* spectroscopic characterizations. (a,b) Cu and (c) O XPS spectra and (d) EDS spectra for as-prepared Cu/Cu_2O (a, blue line in c, d) and after NO_3RR (b, orange line in c, d). Inset in (d) zoom in the O peak of EDS spectra. The electrolysis was conducted for 1 hour at −0.77 V *vs.* SHE, electrolyte consisting of 0.5 mol L^{-1} Na_2SO_4 and catholyte with addition of 2.35 mmol L^{-1} $NaNO_3$.

Figure 2.5. Cu/Cu_2O *ex-situ* characterizations. (a-b) SEM images and (c-d) AFM topology maps of the Cu/Cu_2O catalyst before (a,c) and after (b,d) NO_3RR. The electrolysis was conducted for 1 hour at −0.77 V *vs.* SHE, electrolyte consisting of 0.5 mol L^{-1} Na_2SO_4 and catholyte with addition of 2.35 mmol L^{-1} $NaNO_3$.

Figure 2.6. *In-situ* spectroscopies for Cu/Cu_2O characterizations. (a) Raman spectroscopy of Cu/Cu_2O under NO_3RR conditions from 0.0 to −1.0 V *vs.* SHE (shades of green), with the peaks related to Cu_2O highlighted in blue. (b) Punctual Cu *K*-edge XANES spectra for Cu foil (orange line), Cu_2O (blue line) and for Cu/Cu_2O (shades of green) under different applied potentials. All measurements were conducted using Cu/Cu_2O on Au as WE with electrolyte containing 0.1 mol L^{-1} $NaNO_3$ and 0.5 mol L^{-1} Na_2SO_4.

Figure 2.7. XANES maps for the distribution of oxidation states of Cu^+ (a,c) and Cu^0 (b-d) of 50 x 50 μm area of the catalyst obtained at (a,b) −0.8 and (c,d) −1.0 V vs. SHE. The measurements were conducted using Cu/Cu_2O on Au as WE with electrolyte containing 0.1 mol L^{-1} $NaNO_3$ and 0.5 mol L^{-1} Na_2SO_4.

Figure 2.8. *In-situ* FTIR spectra for (a) Cu/Cu_2O and (b) a Cu rod as WE. Electrolyte consists of 0.1 mol L^{-1} $NaNO_3$ and 0.5 mol L^{-1} Na_2SO_4. The peak centered at 1111 cm^{-1} (yellow) related to -NH_2 from NH_2OH is highlighted in yellow.

Figure 2.9. pH of the catholyte measured after the NO_3RR (a), NH_3 FEs (b) and NO_3^- rate orders to NH_3 for alkalized (dark red), non-buffered (light red) 0.5 mol L^{-1} Na_2SO_4 and 0.2 mol L^{-1} PB (golden) electrolytes in terms of applied potential. Electrolysis conditions: 10 min, with the

addition of 5 to 50 mmol L^{-1} $NaNO_3$ in the catholyte stirring rate at 700 rpm. The black arrow and shaded area in (a) indicate the alkaline pH shift in the non-buffered Na_2SO_4 electrolyte.

Figure 3.1. Ions' concentration and the solution pH of 0.2 mol L^{-1} $Na_xH_{3-x}PO_4$ (black line) electrolytes from pH 4.4 to 9.3.

Figure 3.2. The fifth cathodic scans of CVs for Cu RDE recorded at different pHs in the absence (a) and presence (b) of 0.05 mol L^{-1} $NaNO_3$. Electrolyte containing 0.2 mol L^{-1} $Na_xH_{3-x}PO_4$ at pHs 4.4, 5.7, 7.1, 8.3 and 9.3, the scan rate of 20 mV s^{-1}, the rotation rate of 1600 rpm, potential range between -0.2 and -0.8 V vs. RHE. (c) Evolution of the NO_3RR peak position in function of electrolyte pH.

Figure 3.3. Potential dependence of the steady-state current of 1-minute chronoamperometric experiments conducted in different electrolytes using a copper mesh as WE. The electrolyte consists of 0.2 mol L^{-1} $Na_xH_{3-x}PO_4$ at pHs 4.4 (a), 7.1 (b) and 9.3 (c) with the absence (gray lines) and the presence of 0.05 mol L^{-1} $NaNO_3$ (navy lines) or 0.05 mol L^{-1} $NaNO_2$ (orange lines). Figures d-f show the pH influence on the activity of Cu for the electrolyte containing 0.2 mol L^{-1} $Na_xH_{3-x}PO_4$ with the absence (d) and presence of 0.05 mol L^{-1} $NaNO_3$ (e) or 0.05 mol L^{-1} $NaNO_2$ (f). The experiments were conducted in a 2-compartment H-cell separated by a Nafion 424 membrane, saturated Ag/AgCl RE, and a Pt plate as CE under argon atmosphere. The catholyte was stirred at 700 rpm to minimize the mass transport limitation of the recorded currents. The error bars denote the standard deviation of at least two separate experiments.

Figure 3.4. Potential dependence on RHE scale of the steady-state current of 1-minute chronoamperometric experiments conducted in different electrolytes using a copper mesh as WE. pH influence on the activity of Cu for the electrolyte containing 0.2 mol L^{-1} $Na_xH_{3-x}PO_4$ with the absence (a) and presence of 0.05 mol L^{-1} $NaNO_3$ (b) or 0.05 mol L^{-1} $NaNO_2$ (c). The experiments were conducted under the same conditions as in Figure 3.3. The error bars denote the standard deviation of at least two separate experiments.

Figure 3.5. Scheme of the reaction mechanisms through which the nitrate reduction to nitrite can occur depending on the pH: acidic one highlighted in blue and neutral/alkaline one highlighted in red.

Figure 3.6. Differential Electrochemical Mass Spectrometry results. (a) Potential steps applied over time. Variation of ionic current related to m/z = 29 (b), 30 (c), 32 (d), 33 (e), 44 (f) for nitrate electrochemical reduction on Cu at pHs 4.4 (blue line) and 9.3 (red line). Experiments were

conducted in a 1-compartment electrochemical cell containing 0.2 mol L^{-1} NaH_2PO_4 (pH 4.4) or Na_2HPO_4 (pH 9.3) + 0.1 mol L^{-1} $NaNO_3$, a Cu mesh as working electrode, Pt as counter electrode and a leak-less Ag/AgCl as reference electrode.

Figure 3.7. Scheme of the reaction mechanisms for nitrite conversion to NO at acidic (blue) and alkaline (red) pHs.

Figure 3.8. Differential Electrochemical Mass Spectrometry results. (a) Potential steps applied over time. Variation of ionic current related to m/z = 17 (b) and 18 (c) for nitrate electrochemical reduction on Cu at pHs 4.4 (blue line) and 9.3 (red line). Experiments were conducted in a 1-compartment electrochemical cell containing 0.2 mol L^{-1} NaH_2PO_4 (pH 4.4) or Na_2HPO_4 (pH 9.3) + 0.1 mol L^{-1} $NaNO_3$, a Cu mesh as working electrode, Pt as counter electrode and a leak-less Ag/AgCl as reference electrode.

Figure A1. Linear sweep voltammetries conducted from 0.2 to −1.2 V vs. SHE, scan rates of 20 mV s^{-1} for Au substrate (golden lines) and Cu/Cu_2O catalyst (blue lines). Electrolyte containing 0.5 mol L^{-1} Na_2SO_4 in the presence (solid lines) and absence (dotted lines) of 0.05 mol L^{-1} $NaNO_3$.

Figure A2. Photos of the electrochemical cells, including labels for their elements: WE for working electrode, RE for reference electrode, and CE for counter electrode. (a) 2-compartment electrochemical cell employed for kinetic experiments. (b) Spectro-electrochemical cell for *in-situ* FTIR. (c) Spectro-electrochemical cell for *in-situ* Raman spectroscopy measurements.

Figure A3. UV-Vis spectra of (a) NH_3 and (c) NO_2^- quantifications. Linear regression for (b) NH_3 and (d) NO_2^- with the relationship between maximum absorbance and product concentration.

Figure A4. ^1H NMR spectra for $^{15}NH_4^+$ at δH 6.98 (d, 73.2 Hz) (black curve) and $^{14}NH_4^+$ at δH 6.97 (t, 52.3 Hz) (red curve) obtained after 1 h electrolysis in 0.5 mol L^{-1} Na_2SO_4 and (a) 2.4 mmol L^{-1} and (b) 24 mmol L^{-1} of $^{15}NaNO_3$ and $^{14}NaNO_3$, respectively, at −0.8 V vs. SHE.

Figure A5. Electrochemically active surface area (ECSA) measurements. (a) Metallic flat Cu specific capacitance measurements. (b) Cyclic voltammetries of Cu/Cu_2O catalyst at different scan rates (10 to 100 mV s^{-1}). Electrolyte containing 0.5 mol L^{-1} Na_2SO_4. Red line indicates the capacitive double-layer current that was used for the (c) linear relationship (black line) for the modulus of the average of double-layer current and the scan rate.

Figure A6. NH_3 partial current densities normalized by geometric areas for as-prepared, 10 min-reduced and 10 h-reduced Cu/Cu_2O (shades of blue) and pure Cu (orange). The results were obtained from 10 minutes of potentiostatic electrolysis with the catalyst as WE, graphite rod as CE

and Ag/AgCl as RE, electrolyte containing 0.5 mol L^{-1} Na_2SO_4 adding 0.05 mol L^{-1} $NaNO_3$ in the catholyte.

Figure A7. Cu double-layer capacitance (C_{dl}) before (gray bar) after electrolysis at different applied potentials. Electrolyte containing 0.5 mol L^{-1} Na_2SO_4 and 0.05 mol L^{-1} $NaNO_3$.

Figure A8. Faradaic efficiencies towards nitrite (pink) and ammonia (blue) obtained from 10 min-electrolysis with [$NaNO_3$] = 50 mmol L^{-1} for as-prepared Cu/Cu_2O composite. Data extracted from chronoamperometric electrolysis for 10 minutes with electrolyte containing 0.5 mol L^{-1} Na_2SO_4 (pH_0 = 5.8) and stirred at 700 rpm.

Figure A9. Faradaic efficiencies toward nitrite (pink) and ammonia (blue) obtained from 10 min-electrolysis with [$NaNO_3$] = 50 mmol L^{-1} for pure metallic copper. Data extracted from chronoamperometric electrolysis for 10 minutes with electrolyte containing 0.5 mol L^{-1} Na_2SO_4 (pH_0 = 5.8) and stirred at 700 rpm.

Figure A10. Surface contact potential maps recorded with Kelvin Probe AFM for the Cu/Cu_2O before (a) and after (b) NO_3RR. Electrolysis conditions: 1h-electrolysis at −0.77 V vs. SHE; electrolyte containing 0.5 mol L^{-1} Na_2SO_4 and catholyte with addition of 2.35 mmol L^{-1} $NaNO_3$.

Figure A11. Evolution of electrolyte (catholyte and anolyte) pHs over the time for an electrolysis at −0.93 V vs. SHE. Electrolyte containing 0.5 mol L^{-1} Na_2SO_4 and catholyte with 0.05 mol L^{-1} $NaNO_3$.

Figure A12. Relationship between nitrate rate orders for ammonia production and applied potential (in V vs. RHE) for alkalized (dark red), non-buffered (light red) 0.5 mol L^{-1} sodium sulfate, and 0.2 mol L^{-1} phosphate buffer (yellow) electrolytes. Data extracted from chronoamperometric using the as-prepared Cu/Cu_2O catalyst as working electrode for 10-min electrolysis varying [NO_3^-] from 5 to 50 mmol L^{-1}, stirred at 700 rpm.

Figure A13. (a) Voltammetries from 0.2 to −1.2 V vs. SHE, scan rates of 20 mV s^{-1} for non-buffered (light red) 0.5 mol L^{-1} sodium sulfate, and 0.2 mol L^{-1} phosphate buffer (yellow) electrolytes the presence (solid lines) and absence (dashed lines) of 0.05 mol L^{-1} $NaNO_3$. (b) Zoom of voltammetries region to identify peaks related to Cu_2O reduction.

Figure A14. Photo of the electrochemical cell used for DEMS experiments indicating its components.

List of abbreviations

HB	Haber-Bosch
GHG	Greenhouse gas
BTX	Benzene, toluene, xylene
NO_3RR	Electrochemical nitrate reduction reaction
NOx	Oxidation number
RDS	Rate-determining step
LUMO	The lowest unoccupied molecular orbital
DFT	Density functional theory
DEMS	Differential electrochemical mass spectrometry
HER	Hydrogen evolution reaction
SHE	Standard hydrogen electrode
WE	Working electrode
CE	Counter electrode
RE	Reference electrode
CV	Cyclic voltammetry
OCP	Open circuit potential
PB	Phosphate buffer
FE	Faradaic efficiency
RHE	Reversible hydrogen electrode
NMR	Nuclear magnetic resonance
ECSA	Electrochemically active surface area
LNNano	Brazilian Nanotechnology National Laboratory
CNPEM	Brazilian Center for Research in Energy Materials
SEM	Scanning electron microscopy
TEM	Transmission electron microscopy
STEM	Scanning transmission electron microscopy
AFM	Atomic force microscopy
KPFM	Kelvin probe force microscopy

XPS	X-ray photoelectron spectroscopy
SEC	Spectro-electrochemical cell
XANES	X-ray absorption near edge spectroscopy
LNLS	Brazilian laboratory of synchrotron light
XRF	X-ray fluorescence
PCA	Principal component analysis
FTIR	Fourier transform infrared spectroscopy
MCT	Mercury-cadmium-telluride
FIB	Focused ion beam
EDS	Energy dispersive X-ray spectroscopy
RDE	Rotating disk electrode
NO_2RR	Electrochemical nitrate reduction reaction
EPR	Electron paramagnetic resonance
EXAFS	Extended X-ray adsorption fine structure
SECM	Scanning electrochemical microscopy
RRDE	Rotating ring-disk electrodes
ATR-SEIRAS	Attenuated total reflectance-surface-enhanced infrared spectroscopy

List of symbols

π^*	π antibonding molecular orbital
pKa	Acid dissociation constant
j_{NH3}	Ammonia partial current density
k	Rate constant
α	Rate order
E_{SHE}	Potential corrected *vs.* SHE
$E_{Ag/AgCl}$	Applied potential *vs.* Ag/AgCl
$E_{Ag/AgCl}^0$	Standard potential for the Ag/AgCl RE *vs.* SHE at 25°C
E_{RHE}	Potentials corrected *vs.* RHE
n	Number of electrons transferred
F	Faraday constant
[P]	Product`s concentration
V_{cat}	The volume of the catholyte
Q_{total}	Total charge from an electrolysis
C_{dl}	Double-layer capacitance
$C_{specific}$	Specific capacitance
A_{geo}	Geometric area
m/z	Mass charge ratio
I_{ionic}	Ionic current
h	Planck constant
υ	Electron paramagnetic resonance frequency
g	Electron paramagnetic resonance spectroscopy constant
β	Bohr magneton
B	Applied magnetic field by electron paramagnetic resonance

Table of Contents

Chapter 1. Introduction

This chapter introduces some key concepts of this thesis. We discuss how electrocatalysis can be an alternative to handle the harmful accumulation of nitrate in the ecosystems and to minimize the carbon footprint of the ammonia industry. Additionally, we present some key factors that govern the electrocatalytic nitrate reduction reaction and outline the objectives of this thesis.

1.1 The Disturbance in the Nitrogen Cycle

Early in the 20th century, humanity faced one of the main challenges along its existence: how could we feed such a growing population with limited arable lands and resources?[1] The Industrial Revolution allowed us to manage energy toward industrial processes and transportation, saving humans time and workforce. The transformations arising from the Industrial Revolution coupled with the establishment of a capitalist mode of production demanded a constantly growing population to maintain the increase of profits and consumption.[2] Although the population was increasing to respond to this demand, food production did not grow at the same rate, due to the limited availability of nutrients, mainly nitrogenous compounds that were by then only fixed through biological processes.[1,3] At that time, there was an increasing demand to find alternative ways to obtain such important nitrogenous compounds.

To address this problem, the Prussian scientist Fritz Haber in 1905 reported the production of small amounts of ammonia (NH_3) by mixing dinitrogen (N_2) with hydrogen (H_2) gases at 1000°C using iron as a catalyst.[4] Later on, by further increasing the operating pressure to 150 – 200 atmospheres he was able to improve the process and obtain a more significant amount of NH_3 at 500°C. Afterward, Carl Bosch industrialized this reaction,[5] naming the process of the catalytic hydrogenation of N_2 to ammonia as Haber-Bosch (HB).[1] Together, they developed a way to catalytic hydrogenate the N_2, highly abundant in the earth's atmosphere, fixing it into a compound that could be used as a fertilizer in agricultural activities.[1] The principle of catalytically conducting reactions at high pressures and temperatures led to the synthesis of several compounds, such as methyl alcohol[6] and nitric acid.[7] The discovery of the reaction earned Fritz Haber the Nobel Prize in Chemistry in 1918 "for the synthesis of ammonia from its elements"[4] and for its industrialization, Carl Bosch was awarded the Nobel Prize in Chemistry in 1931.[5]

Comparing the number of humans fed per hectare of arable land from 1908 to 2008, it has increased from 1.9 to 4.3 persons over these 100 years.[2] This huge improvement in agricultural productivity is mainly attributed to the development of the HB process, which allow fixing N_2 into NH_3.[1] Since the end of the 20th century, over 40% of the global population has depended on fertilizers which are produced by the HB process.[8] Figure 1.1 illustrates how our dependency on the HB process increased over the last 120 years.

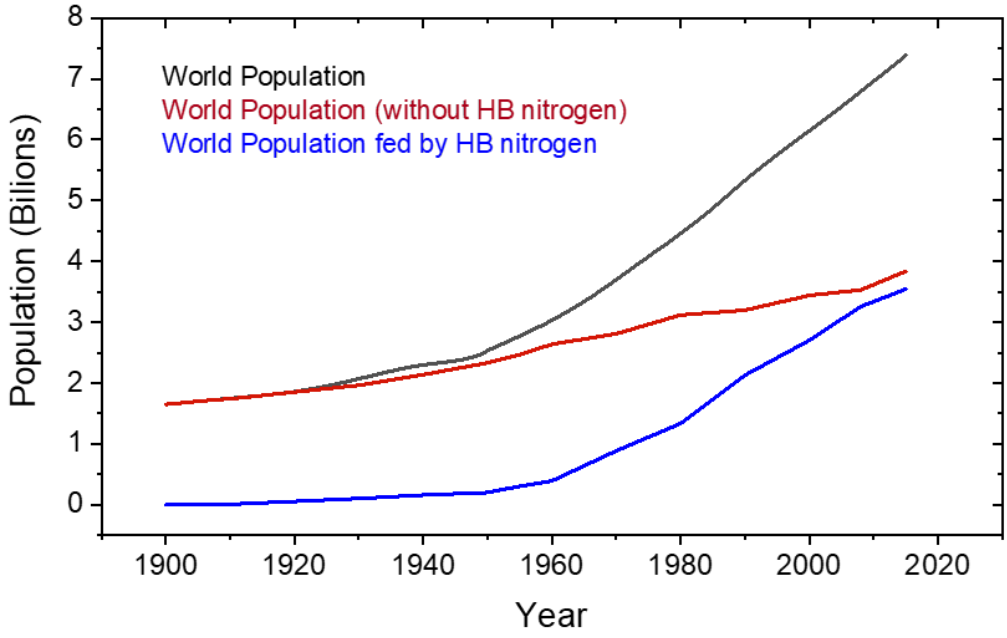

Figure 1.1. Evolution of the global population growth (black line) estimated population fed by Haber-Bosch nitrogenous fertilizers (blue line), and the predicted population growth without Haber-Bosch nitrogen (red line) over the years from 1900 to 2015. Data extracted from [9].

Figure 1.1 shows the world population growth over the 20th century, in which the black line represents how it has increased from 1.65 billion in 1900 to 7.4 billion people in 2015. The blue line in Figure 1.1 estimates how many births were enabled by HB nitrogen from the decade of 1910 onwards,[1,2] while the red line shows how the population would increase over the century without the HB process. Erisman *et al.*[1] estimated that 48% of the global population was fed by HB nitrogenous fertilizers in 2015. Thus, without the HB process, the current world population would be around 3.5 to 4 billion people.

Although the HB process has enabled this drastic population growth, the fixation of N_2 at industrial scales to supply the intensive use of fertilizers caused a global imbalance in the nitrogen cycle.[10,11] It fixes around 10^8 tons of nitrogen into reactive species per year,[12] which accumulate in the aquatic systems over time. In 2017, the National Academy of Engineering recognized the management of the nitrogen cycle as a grand challenge for engineers.[13] Therefore, it is urgent to develop improved technologies for wastewater treatment to minimize the increasing concentrations of nitrogenous species in water streams.

Among the nitrogen-containing contaminants, nitrate (NO_3^-) is the most oxidized species and the main pollutant of wastewater.[14] The accumulation of NO_3^- in aquatic systems leads to harmful environmental consequences, such as algal blooms, and the poisoning of fishes and their predators, possibly creating "dead zones".[15] Additionally, the consumption of nitrate through the ingestion of contaminated water can lead to the development of diseases, such as cancer and methemoglobinemia.[16,17] Fertilizers are the main source of nitrogenous contaminants, from which we can establish a clear correlation between NO_3^- contamination in groundwater and rivers with areas in which more agricultural activities are conducted.[18,19] Besides agriculture, some industrial processes have NO_3^- as one of the components of their wastewater.[20] Thus, the accumulation of NO_3^- is an alarming problem that needs to be addressed to restore the disturbed nitrogen cycle. The development of technologies that convert NO_3^- into benign (N_2) or more valuable (NH_3) nitrogenous species is crucial to dealing with this issue.[20–24]

1.2 Electrochemical Nitrate Reduction for Wastewater Remediation and Sustainable Ammonia Synthesis

Humanity is currently moving toward an energy transition in which we seek to convert and store energy from renewable sources into electricity to replace the use of fossil fuels to drive industrial processes.[25] The cost of renewable electricity is expected to drop significantly in the next decades, which will potentially make the use of electrochemical alternatives viable to convert pollutants in water streams into benign or valuable chemicals.[26] In the case of NO_3^-, we can promote its electrochemical conversion into NH_3, which would be an alternative to sustainably restore the disturbed nitrogen cycle by using a pollutant as feedstock to produce fertilizers.[20]

Although HB is a centenarian industrial process that has been extensively used to produce fertilizers, there have been few significant changes from initial to current plants, that until now operate at high temperatures (400 – 500°C) and pressures (150 – 300 bar).[8] Even for the low-energy Kellogg ammonia plants, developed by the year 1995, the energy required to operate at high pressures corresponds to 40% of the total energy consumption during the reaction.[8] Additionally, the H_2 gas used for N_2 hydrogenation is produced by the steam reforming of fossil-fuel feedstock, such as methane, which emits large amounts of carbon dioxide (CO_2), the main greenhouse gas (GHG) in the atmosphere.[25] Figure 1.2 illustrates how GHG emissions from the HB process are compared to other chemical industries.

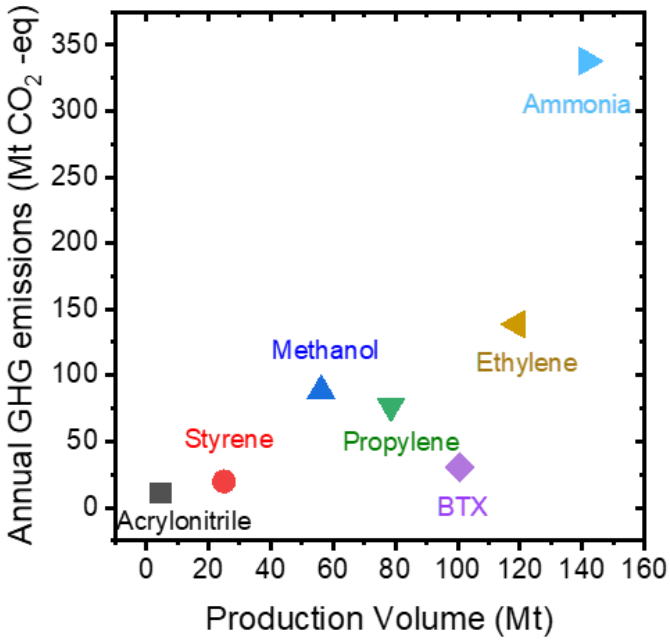

Figure 1.2. Greenhouse gas emissions for selected high production volume chemicals in 2010. BTX = benzene, toluene, xylene (aromatic chemicals). The data to produce this graph was extracted from [25].

Figure 1.2 shows the annual GHG emissions of the main chemical industries in CO_2-equivalent quantities of different chemicals in terms of their production volume. NH_3 is the most produced chemical in the chart, but its GHG emission is disproportionally higher than the other chemicals, since for each ton of NH_3 produced, 1.9 tons of CO_2 are emitted.[25] Considering all the processes of synthesizing and transporting ammonia, they consume 2% of overall global energy production.[12] Thus, the development of cleaner processes to supply the production of NH_3 has been attracting growing attention from the scientific community in the last few years.[21]

The electrification of NH_3 synthesis is crucial to minimize the high carbon footprint of the HB process.[3,27] In this regard, several alternatives to electrochemically mimic HB through the hydrogenation of N_2 have been studied, since atmospheric N_2 is the most abundant nitrogenous species and the ideal feedstock.[27] For this objective, many challenges need to be addressed, such as electrolyte engineering to improve N_2 solubility, and reducing the applied overpotential, since activating N_2 requires 946 kJ mol^{-1}, the energy of the strong triple N≡N bond.[28]

The high carbon footprint of the NH_3 industry combined with the alarming problem of increasing NO_3^- concentrations in water streams makes the electrochemical NO_3^- reduction reaction (NO_3RR) to NH_3 an interesting alternative to overcome both environmental problems.[14,17,26,28] Although NO_3^- is not as abundant as N_2, by using a pollutant to produce a valuable fertilizer, we would be managing nitrogenous species toward a circular economy, which could help the reestablishment of the disturbed nitrogen cycle.[26] In the next session, we will go deeper into key variables governing NO_3RR that can be studied to enable it as a solid alternative to both wastewater remediation and NH_3 synthesis.

1.3 Fundamental Aspects of the Electrocatalytic Nitrate Reduction

Electrocatalysis is a crucial science field to enable the electrification of industrial processes.[25] An electrolytic process consists of controlled electron transfer to drive electrochemical reactions. The flux of electrons is generated through the application of an electric potential, which correlates with the energy required for the electrochemical reaction to occur (overpotential).[29] The recorded current represents the amount of charge that is transferred per unit of time, which reflects the reaction rate of an electrochemical reaction.[30]

An electrocatalyst not only enables electron transfer but actively catalyzes the reaction by selectively adsorbing intermediates, leading to a significant enhancement of the electrochemical reaction rate.[29,31] For a better design of electrocatalysts, we must comprehend what are the active sites that promote the adsorption of the key intermediates that lead to the formation of the target product. What an electrochemist who aims to explore electrocatalytic aspects of an electrochemical reaction must do is explore how modifying the electrocatalyst material can impact the reaction rates to form the desired product.[30,31] One way of doing so is to perform electrolysis experiments on different materials under the same conditions to be able to compare their activity and selectivity toward a desirable product for a given electrochemical reaction.[30–32]

Not only is the electrocatalyst important to an electrochemical reaction but also the electrolyte conditions play a central role in how the reaction occurs.[14,33,34] For aqueous electrolytes, certain aspects of the solution, such as its pH, the ions' concentration, and the mass transport of the electroactive species are crucial to understanding the paths through which a given electrochemical reaction will follow.[30,35] The presence of some ions within the electric double layer can either promote or hinder an electrochemical reaction, depending on how they influence

the adsorption of reaction intermediates.[34,36,37] Especially for proton-consuming electrochemical reactions occurring in aqueous electrolytes, such as the NO_3RR, the pH is a key factor governing the mechanisms the reaction undergoes.[30,36] For a better electrolyte design, it is important to understand how the reaction rates are impacted by varying the pH.

Being NO_3^- the most oxidized nitrogenous contaminant in water streams, the electron-driven conversion of NO_3^- into NH_3 would require its reduction through the transfer of 8 electrons to shift oxidation number (NOx) of nitrogen from +5 to −3.[14] The global conversion of NO_3^- to NH_3 can be summarized as the following equations for acidic and alkaline media (Equations 1.1 and 1.2, respectively):[17,38]

$$NO_3^-{}_{(aq)} + 10H_3O^+{}_{(aq)} + 8e^- \rightarrow NH_4^+{}_{(aq)} + 13H_2O \qquad \text{(Eq. 1.1)}$$

$$NO_3^-{}_{(aq)} + 7H_2O + 8e^- \rightarrow NH_4OH_{(aq)} + 9OH^-{}_{(aq)} \qquad \text{(Eq. 1.2)}$$

Eq. 1.1 represents the global reaction for the protons transfer through an acidic mechanism, in which there is a high concentration of protons to be transferred, while Eq. 1.2 exemplifies the mechanism by which NO_3RR to NH_3 would undergo in an alkaline environment.[17] Depending on the solution pH, NH_3 can be protonated to ammonium (NH_4^+), as shown in Eq. 1.1, or react with water to form ammonium hydroxide (NH_4OH), as shown in Eq. 2.[14] These species would be in equilibrium with NH_3, as the following Equations 1.3 and 1.4 show respectively:

$$NH_{3\,(aq)} + H_3O^+_{(aq)} \rightleftharpoons NH_4^+{}_{(aq)} + H_2O \qquad \text{(Eq. 1.3)}$$

$$NH_{3\,(aq)} + H_2O \rightleftharpoons NH_4OH_{(aq)} \qquad \text{(Eq. 1.4)}$$

Although we can simplify the overall reaction of NO_3RR to NH_3 as shown in Eqs. 1.1 and 1.2, we need to describe several elementary steps to comprehend the electrocatalytic NO_3RR on a catalyst surface. There is a myriad of nitrogenous byproducts that can be formed from NO_3RR, such as nitrite (NO_2^-), N_2, nitrous oxide (N_2O), hydrazine (N_2H_4), nitric oxide (NO), etc.[17,38] The product distribution from NO_3RR depends on how the electrocatalyst binds key intermediates, whether they are susceptible to desorb or reduce them, their adsorbing orientation and hydrogenation, the coverage of the adsorbates, etc.[39] Understanding how those interactions are influenced by both catalyst and electrolyte is crucial to designing better electroactive materials and electrolyte solutions for NO_3RR.[40] A successful electrochemical process must employ a highly active and selective electrocatalyst to form the desired product and be stable under the reaction's

conditions. Subsections 1.3.1 and 1.3.2 will present some of the key aspects of the catalyst and electrolyte that influence the NO_3RR electrocatalytic activity and selectivity to produce NH_3.

1.3.1 Electrocatalysts for Nitrate Reduction

To understand what makes a good catalyst for NO_3RR, we must first comprehend how kinetically and thermodynamically favorable are the binding and charge transfer between the electrode surface and NO_3^- species.[41] In this thesis, we will focus on the electrocatalysis of NO_3RR on metals and oxides electrodes, although there are several other alternatives, such as sulfides,[42] hydrides,[43] and molecular catalysts.[44]

The adsorption of NO_3^- and its reduction to NO_2^- is reported to be the rate-determining step (RDS) of the NO_3RR, due to the high energy of the lowest unoccupied molecular orbital (LUMO) π^* of NO_3^-, which hinders the charge injection into this orbital.[14,17,28,40] NO_3^- species adorbs onto two atoms of platinum (Pt) with bidentate adsorption: two oxygens atoms binding two atoms of Pt, which was detected first with surface-enhanced infrared adsorption.[45] The adsorption energy of NO_3^- on the catalyst active site is the first and very important step to obtain high activity for NO_3RR.[40] Although the high energy of the LUMO π^* of NO_3^- represents the main barrier to be overcome by the electrocatalysts, the metals that have highly occupied *d*-orbitals, such as copper (Cu), silver (Ag), and Pt, present similar *d*-band energy levels to NO_3^- LUMO π^*, favoring the charge transfer between them.[14]

Once NO_3^- is adsorbed, the conversion of $NO_3^-{}_{(ads)}$ into $NO_2^-{}_{(ads)}$ can occur via two different mechanisms, depending on the hydrogen coverage onto the catalyst surface under reaction conditions. Figure 1.3 illustrates how this conversion can happen through a hydrogen-assisted reduction (in blue) or a direct reduction (in green). The first one would occur with the previous reduction of water to form $H_{(ads)}$ onto the catalyst surface, which reacts with $NO_3^-{}_{(ads)}$ to form $NO_2^-{}_{(ads)}$ through the release of one water molecule.[28] This path was suggested to occur on strained ruthenium (Ru) by the formation of a reductive environment that forms hydrogen radicals.[46] The direct reduction (highlighted in green in Figure 1.3) involves two electron transfers assisted by 2 water molecules, which would be the case for Pt and tin (Sn).[47,48] The formation of $NO_2^-{}_{(ads)}$ is followed by its reduction to $NO_{(ads)}$, that can be both direct or H-assisted.[28] The $NO_{(ads)}$ is a divergent central intermediate whose mode of protonation is key to determining the selectivity of the NO_3RR.[28,39]

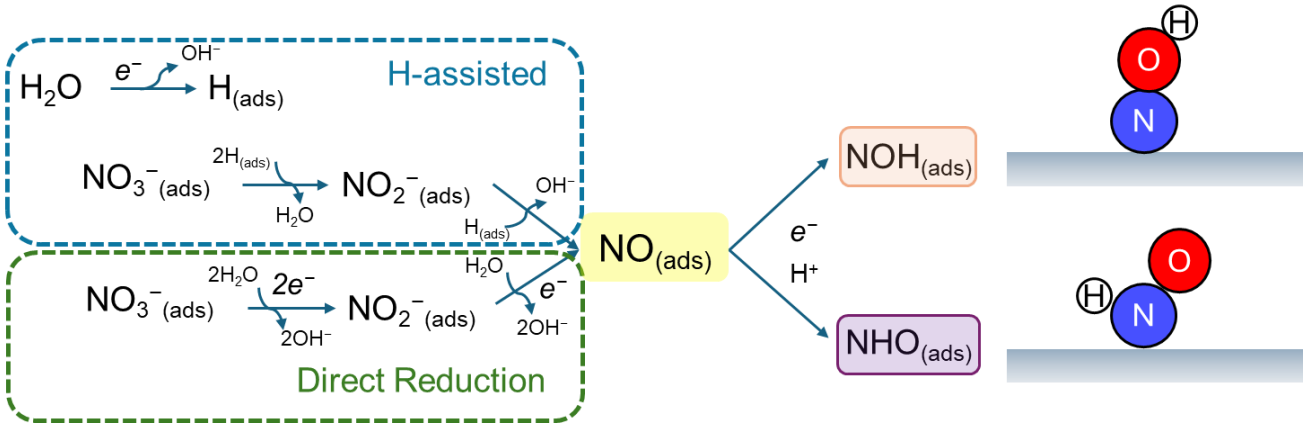

Figure 1.3. Scheme for the possible mechanisms for NO_3RR to $NO_{(ads)}$ (hydrogen-assisted one is highlighted in blue and the direct reduction is highlighted in green), and consequent protonation of $NO_{(ads)}$ leading to the species illustrated on the right.

Considering that $NO_{(ads)}$ is a divergent intermediate of NO_3RR, its adsorption energy is a critical parameter that dictates the product's selectivity.[28] The protonation of $NO_{(ads)}$ can lead to two different species: $NOH_{(ads)}$ (highlighted in orange in Figure 1.3), in which hydrogen binds the O atom, or $NHO_{(ads)}$ (highlighted in purple in Figure 1.3), in which H binds the N atom.[39,49] Romeo *et al.*[39] demonstrated with catalytic matrices that the mode of the hydrogenation of $NO_{(ads)}$ depends on the identity of the metal site and its coordination number. They showed that $NHO_{(ads)}$ is expected to form on Cu, Ag, and Au (metals of group 11), while either only $NOH_{(ads)}$ or both $NHO_{(ads)}$ and $NOH_{(ads)}$ are formed on metals from groups 9 and 10 (Ni, Pd, Pt, Co, Rh, and Ir).[39] Regarding the structure influence on $NO_{(ads)}$ hydrogenation, they report that for elements of group 11, especially for Cu, less coordinated sites are more likely to promote $NHO_{(ads)}$.[39] Whether the protonation of $NO_{(ads)}$ leads to $NOH_{(ads)}$ or $NHO_{(ads)}$ dictates the selectivity of NO_3RR, as shown in Figure 1.4.

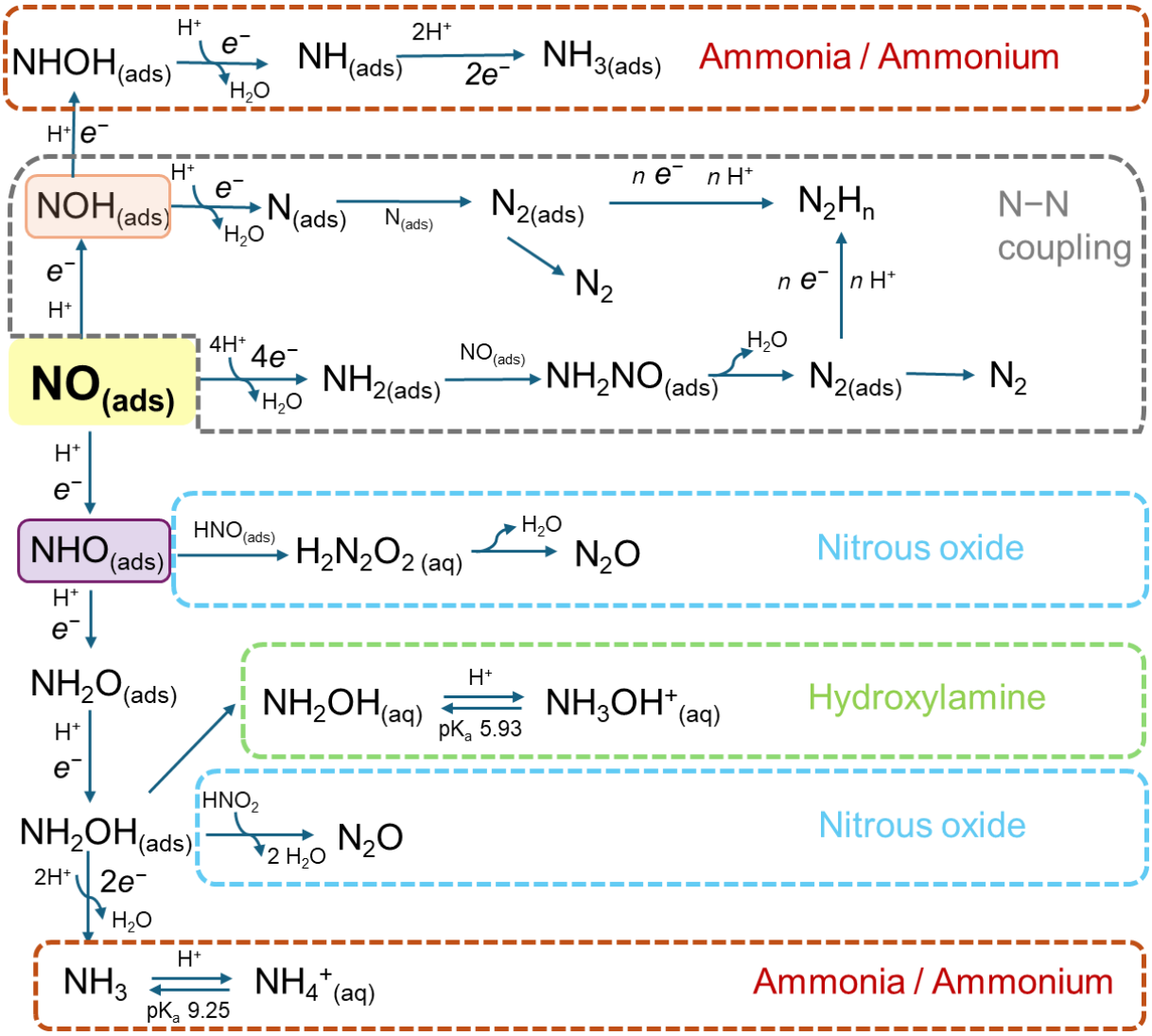

Figure 1.4. Scheme of the possible mechanisms of the reduction of $NO_{(ads)}$. The formation of ammonia/ammonium is highlighted in red, the N–N coupling in gray, the formation of nitrous oxide in light blue, and hydroxylamine in light green.

Figure 1.4 shows the different paths through which NO_3RR can undergo from the divergent central intermediate $NO_{(ads)}$. The two possible protonated species that are shown in Figure 1.3 are highlighted in orange and purple in Figure 1.4, $NOH_{(ads)}$ and $NHO_{(ads)}$ respectively. By favoring the formation of the intermediate $NOH_{(ads)}$, the N–N coupling mechanisms (in gray in Figure 1.4) are more likely to occur,[39,49,50] favoring the formation of N_2. We can also obtain NH_3 from $NOH_{(ads)}$ through its subsequent protonation in the N atom to form $HNOH_{(ads)}$ followed by the release of water to form $NH_{(ads)}$ species (in red on the top of Figure 1.4). This mechanism for

NH_3 is less likely to occur than N_2 formation since it demands 3 additional proton-electron transfer steps to obtain NH_3 compared to N_2.[28] From the formation of $NHO_{(ads)}$, especially for what is reported for Cu-based catalysts,[35,51,52] the production of hydroxylamine (NH_2OH) (in light green in Figure 1.4) and NH_3 (in red on the bottom of Figure 1.4) is more favorable. Katsounaros and Kyriacou[48] reported two possible mechanisms for the formation of nitrous oxide (N_2O) either through the coupling of two $HNO_{(ads)}$ species or from the reaction between $H_2NOH_{(ads)}$ with $HNO_{2(aq)}$ (light blue in Figure 1.4). Due to the high solubility of N_2O in water, it can be reduced after its re-adsorption.[14] In summary, the choice and design of the catalyst are crucial to tuning the selectivity toward the desirable product, in our case, NH_3.

In this regard, Cu-based electrodes are attracting increasing attention for designing electrocatalysts for NO_3RR,[53–59] considering Cu combines some key characteristics that make it a good choice for this purpose.[40] Cu is a cheap and abundant metal that has a favorable charge transfer between its *d*-band and NO_3^- LUMO π^* and promotes $NO_{(ads)}$ hydrogenation to $NHO_{(ads)}$ especially, when it is undercoordinated, which favors the formation of NH_3.[39,60,61] Among Cu-based catalysts, its oxides are especially studied due to their capability to enhance the selectivity toward NH_3 compared to unmodified copper.[32,54,55,58,62–69] Considering these oxides are unstable under cathodic reaction conditions,[70] the active site that indeed promotes the NO_3RR to NH_3 on copper oxide-based catalysts is still unclear, and Chapter 2 details how we addressed this ongoing debate in the literature.

1.3.2 Electrolyte pH Influence on Electrocatalytic Nitrate Reduction

The pH of the electrolyte is very important for electrochemical reactions and actively dictates the reaction mechanism of NO_3RR. Additionally, the NO_3RR to NH_3 can either consume 10 moles of protons (Eq. 1.1) or produce 9 moles of hydroxyls (Eq. 1.2) per mole of NH_3 produced depending on the electrolyte pH,[17] which can impact both local and bulk pH during the electrochemical reaction.[32]

Examining the steps required to produce NH_3 from NO_3RR, they consist of multiple proton/electron transfer steps, especially from $NO_{(ads)}$, as shown in Figure 1.4. In this regard, the concentration of protons can determine whether a hydroxonium cation (H_3O^+) a water molecule will be the proton source for the NO_3RR. Anionic species can also donate protons to the hydrogenation of the adsorbates, such as hydrogenophosphate, bicarbonate, etc. Depending on the

electrolyte pH, the reaction can follow different elementary steps and the solution pH determines the predominant species from an acid/base equilibrium, depending on its acid dissociation constant (pK_a). For instance, NH_2OH can be protonated to NH_3OH^+ at pHs lower than 5.93.

The pH influence on NO_3RR not only relies on $NO_{(ads)}$ subsequent protonation steps but also on the first steps of NO_3^- conversion to $NO_{(ads)}$. Figure 1.5 illustrates how the pH can determine the different paths that NO_3RR to $NO_{(ads)}$ undergoes.

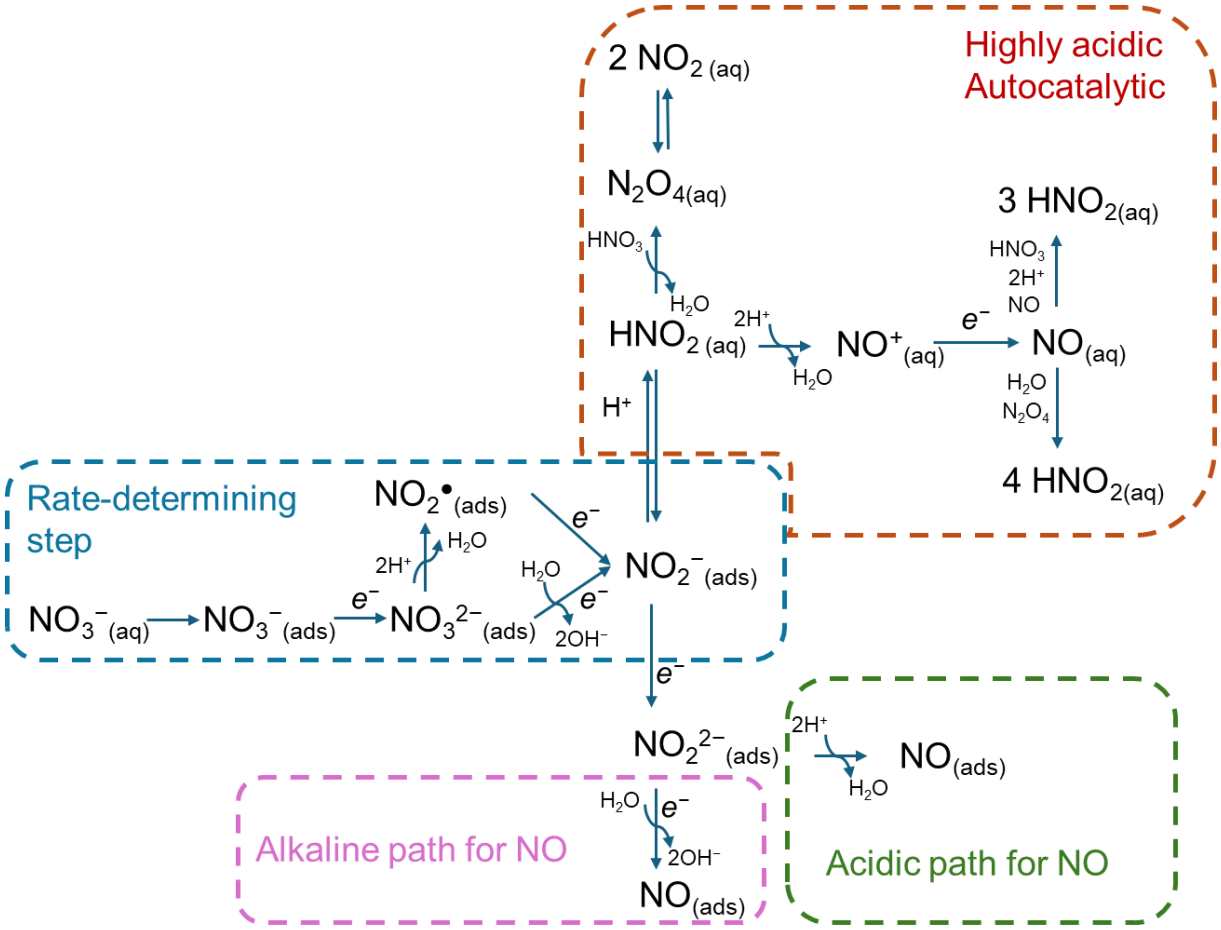

Figure 1.5. Scheme representing the nitrate electrochemical reduction to nitrite (dotted blue rectangle) and the following steps depending on the pH. Highly acidic mechanism in red, alkaline path in pink and mildly acidic one in green.

In Figure 1.5 we can identify that the rate-determining conversion of $NO_3^-{}_{(aq)}$ to $NO_2^-{}_{(ads)}$ depends on the pH (dark blue dotted rectangle). The formation of the radical $NO_2^{\bullet}{}_{(ads)}$ through two proton transfers to $NO_3^{2-}{}_{(ads)}$ occurs in acidic pH,[71] while in alkaline or neutral media,

the reduction of $NO_3^{2-}{}_{(ads)}$ to $NO_2^{-}{}_{(ads)}$ occurs directly through the consumption of a water molecule.[51] In highly acidic environments, the high concentration of protons can trigger an autocatalytic cycle (dark red rectangle in Figure 1.5), through which each molecule of $HNO_{2(aq)}$ ($pK_a = 3.4$) can electrochemically generate 3 or 4 molecules of HNO_2, following the Schmid[72] or Abel[73] mechanisms respectively, being the second one valid for concentrations of HNO_3 higher than 4 mol L^{-1}.[14]

For mildly acidic (pH > 3.4) electrolytes, $NO_{(ads)}$ can be formed through the transfer of two protons to $NO_2^{2-}{}_{(ads)}$ (green dotted rectangle in Figure 1.5).[28] At alkaline and neutral pHs, the conversion of $NO_2^{2-}{}_{(ads)}$ to $NO_{(ads)}$ is an electrochemical process by which a water molecule is consumed and two hydroxyls are released (pink dotted rectangle in Figure 1.5).[28,52]

As we discussed in the last subsection, metallic Cu catalyst has compelling attributes that make it a strong candidate to make the electrocatalytic NO_3RR to NH_3 viable.[40,74] The influence of the pH on single crystals Cu activities for NO_3RR was well studied by Pérez-Gallent *et al.*[35]. They found that at pH 1, HNO_2 is the first intermediate formed, from which NO is released in solution and then re-adsorbed ($NO_{(ads)}$) to be further reduced to NH_4^+ for both Cu(100) and Cu(111) surfaces. For pH 13, they detected the formation of $NO_2^{-}{}_{(aq)}$ and $NH_2OH_{(ads)}$ on both Cu surfaces, being faster on Cu (100).[35] Hu *et al*.[75] also explored both pH and Cu facet influences on NO_3RR to NH_3 with density functional theory (DFT) calculations and reported that the RDS and overpotentials are pH-dependent. Although these findings clarify the mechanism at those boundary pHs (1 and 13), the mechanisms underlying NO_3RR at mildly acid and alkaline electrolytes on Cu remain unclear. Understanding how pHs around 7 impact the NO_3RR is crucial to enable the wastewater treatment of nitrate-rich streams since most of them are neutral solutions. Chapter 3 of this thesis is dedicated to exploring the reaction mechanism of NO_3RR on Cu at pHs ranging from 4.4 to 9.3.

1.4 Scope of the Thesis

The main objective of this thesis is to investigate how both catalyst and electrolyte aspects impact the electrocatalytic nitrate reduction reaction on copper-based materials. The interest in elucidating these aspects of Cu activity for this reaction relies on its high activity for NO_3RR and low cost compared to other metals.[51] However, a good catalyst must also be highly selective toward a valuable product, and stable over catalytic cycles.

To enhance the NO_3RR selectivity of Cu-based catalysts for NH_3, there are several reports in the literature that explore the use of different morphologies and contents of mixed Cu and Cu oxides (CuO and/or Cu_2O) that indeed outperform pure Cu selectivity toward NH_3.[41,54,62,64,67,76,77] However, the active site of copper oxide-based catalysts for NO_3RR to NH_3 remains under debate in the literature. We hypothesize that there must be a correlation between the applied potential and the catalytic active site of Cu oxides for NO_3RR to NH_3, which is addressed by the work presented in Chapter 2 of this thesis. In this chapter, we aim to identify the active site of a composite containing Cu + Cu_2O for NO_3RR and how it correlates with the applied potential. To do so, we performed kinetic electrochemical experiments, *ex-situ* characterizations, and spectroscopic *in-situ* measurements. We also explored the effect of an alkaline shift on the catholyte pH promoted by the NO_3RR when employing a non-buffered electrolyte. In summary, we found that pure Cu is intrinsically active for NO_3RR to NH_3 at higher overpotentials and that the kinetics of the reaction changes with the pH. These findings led us to the second main objective of this thesis, which is to investigate the pH influence on metallic Cu activity to NO_3RR.

In Chapter 3 our objective is to identify the pH influence on the mechanisms through which NO_3RR undergoes at pHs ranging from 4.4 to 9.3. First, we evaluated how the different pHs impact the RDS conversion of NO_3^- to NO_2^-. Tracking the production of key volatile products with differential electrochemical mass spectrometry (DEMS), we correlate the pH with the rate of NO formation and detect the formation of some by-products that are also dictated by the electrolyte pH. This work provides elucidative mechanistic insights into the role of electrolyte pH at mildly acidic and basic conditions on NO_3RR on metallic Cu electrodes.

In summary, this thesis explores some key factors that must be properly understood for a better design of both catalyst and electrolyte conditions that can enable the NO_3RR to NH_3 as a viable alternative for electrochemical wastewater remediation.

Chapter 2. The Active Site of Cu/Cu_2O for Electrocatalytic Nitrate Reduction to Ammonia

This chapter presents our work conducted to identify the active site of a composite containing copper and copper oxide as an electrocatalyst for nitrate reduction to ammonia. Alongside electrochemical kinetic experiments, we explored how the catalyst containing both copper and its oxide modifies under electrochemical nitrate reduction with *in-situ* spectroscopic techniques. The results presented in this chapter are published in "**G. F. Costa**, M. Winkler, T. Mariano, M. R. Pinto, I. Messias, J. B. Souza, I. T. Neckel, M. F. C. Santos, C. F. Tormena, N. Singh, R. Nagao, *Chem Catalysis* **2024**, *4,* 100850."

2.1 Introduction

Copper-based catalysts for NO_3RR to NH_3 have attracted increasing attention in the last years due to their capability to promote the charge transfer to LUMO π^* of NO_3^- and stabilize some key intermediates to enhance the activity for NH_3 production, such as $NHO_{(ads)}$.[40,74,78,79] To improve the selectivity of Cu-based catalysts, there are some purposes in the literature that include alloying with other metals,[41,80–83] designing materials combining metallic and oxide phases,[45,67,76] using sulfides,[84] hydrides,[44] etc.

Among the Cu-based catalysts, composites containing Cu_2O with a metallic phase, especially Cu itself, are reported to boost the formation of NH_3 from NO_3RR,[59,68,85,86], being the interface between the metal and Cu_2O the active site for this reaction, as proposed in some reports in the literature.[54,62] The promotion of NH_3 formation on the metal-oxide interface is attributed to its capability to boost the hydrogenation of $NO_{(ads)}$ and suppress the competing hydrogen evolution reaction (HER). In the work presented in this chapter, we evaluate the catalytic activity of a composite containing Cu and Cu_2O electrochemically alternately deposited through a galvanostatic oscillatory potential regime, using a Cu(II)-lactate system.[87] We explored the possibility of using self-organization in electrochemical systems as a tool for designing new materials in our review article,[88] and the work presented here goes in this direction.

Although some reports using Cu oxide-based catalysts suggest the presence of the oxide phase actively promoting NO_3RR to NH_3,[54,62] we would expect the reduction of Cu_2O species at high overpotentials, under cathodic conditions, considering the Cu Pourbaix diagram.[70] Considering Cu oxides instabilities under operation conditions for NO_3RR, Daiyan *et al.*[64] and Yuan *et al.*[58] propose that oxygen vacancies formed in the catalyst lattice from Cu_2O reduction improve are the active site, by favoring the formation of $NHO_{(ads)}$ and its hydrogenation to $NH_2O_{(ads)}$. Contrary to the two previous hypotheses, Song *et al.*[66] and Li *et al.*[65] defend that reconstructed Cu^0 serves as active sites for NO_3RR to NH_3. In the same direction, Anastasiadou *et al.*[55] reported structural changes in Cu_2O nanocubes after the NO_3RR attributing to their catalytic activity to Cu^0 phases. Recently, Bai *et al.*[77] attributed the activity of NO_3RR to NO_2^- to Cu^+ species, while the following formation of NH_3 occurs on Cu^0 active sites. Indeed, there is no consensus on the active phase of Cu_2O-based materials for electrocatalytic NO_3RR to NH_3. To address this debate in the literature we elected three main candidates to explore: the interface

between Cu and Cu_2O, oxygen vacancies formed at higher cathodic potentials, and metallic Cu^0 phases.

In the work presented in this chapter,[32] our objective is to determine the active site of Cu_2O-based materials for the electrocatalytic NO_3RR to NH_3 across the potential range from −0.6 to −1.1 V *vs.* standard hydrogen electrode (SHE). Starting with a composite containing both Cu and Cu_2O, we kinetically evaluated their interface as the active site for NO_3RR to NH_3. By subjecting the composite to different durations of pre-reduction steps, we explored other two potential active sites: oxygen vacancies and metallic Cu^0. Employing a combination of *ex-situ* and *in-situ* spectroscopic and microscopic characterizations, we evaluate how operating conditions for NO_3RR change the composite structure and composition. Based on our kinetic analysis and characterizations, we propose that at low overpotentials (−0.6 to −0.77 V *vs.* SHE), oxygen vacancies serve as the active site for NO_3RR to NH_3, while at higher overpotentials (−1.1 V *vs.* SHE), Cu^0 is the main active phase. Additionally, we detected a significant alkaline shift of the non-buffered catholyte pH from 5.8 to approximately 12, and our findings suggest that this pH increase indeed boosts the formation of NH_3. Thus, we could provide a detailed evaluation of how NO_3RR to NH_3 operating conditions impact both catalyst and electrolyte.

2.2 Experimental Methods

2.2.1 Synthesis of the Catalyst

The deposition of the catalyst containing Cu and Cu_2O was conducted in a 1-compartment electrochemical cell setup. We used a plate with a 0.3848 cm^2 area of Au exposed surface (200 nm of thickness) on Ti (10 nm), both deposited by electron beam onto a silicon wafer as working electrode (WE) and substrate for Cu/Cu_2O. We used a graphite rod as a counter electrode (CE) and a single junction saturated silver chloride (Ag/AgCl) reference electrode (RE) from Pine research. The electrolyte for the deposition consists of 0.5 mol L^{-1} $CuSO_4.5H_2O$ (ACS reagent, >98.0%, Sigma-Aldrich) + 2.5 mol L^{-1} lactic acid (>85.0% Sigma-Aldrich) at pH at 9.0 adjusted with a 6.0 mol L^{-1} NaOH (ACS reagent, >97%, pellets, Sigma Aldrich) solution. The solution was kept under magnetic stirring (1200 rpm) for at least 4 days after its first preparation. The galvanostatic deposition was conducted at −0.75 mA cm^{-2}_{geo} for one hour.[87] We conducted 10 scans of cyclic voltammetry (CV) from 0.1 to 0.6 V *vs.* SHE at a scan rate of 50 mV s^{-1} before each deposition. We also evaluate the activity of the underlying Au layer for NO_3RR, which did

not present substantial electrocatalytic current density for the reaction (Figure A1) compared to the composite one.

2.2.2 Electrochemical Kinetic Measurements

We conducted electrolysis experiments using a two-compartment cell (Figure A2a) separated by a Nafion 117 membrane soaked overnight in ultrapure water (resistivity > 18.2 MΩ cm, Synergy UV). We used a graphite rod as CE in the anolyte compartment and a single junction Ag/AgCl as RE with the WE in the catholyte. The catalysts used as WE will be discussed later. Argon was purged before (at least for 15 minutes) and during the electrolysis. The catholyte was stirred at 700 rpm to minimize the current limited by mass transport. All electrolysis were potentiostatic and 85%-*iR*-compensated considering the impedance measured at 100 kHz at open circuit potential (OCP), with the remaining 15% *iR* being considered afterward, for data analysis.

The unbuffered electrolyte at pH 5.8 was prepared with 0.5 mol L^{-1} Na_2SO_4 (ACS reagent, >99% anhydrous granular, Sigma Aldrich). The phosphate buffer (PB) electrolyte at pH 5.8 was prepared as a solution containing 22.08 g L^{-1} KH_2PO_4 (certified ACS, FisherChemical) + 4.29 g L^{-1} Na_2HPO_4 (ACS reagent, >99.0%, Sigma Aldrich). For the alkalized 0.5 mol L^{-1} Na_2SO_4 electrolyte, we adjusted its pH to 12 with a 6 mol L^{-1} NaOH solution. The solutions' pHs were measured with the OrionStar A214 Thermo Scientific pHmeter. For NH_3 partial current densities (j_{NH3}) and Faradaic efficiencies (FEs) results, we used a concentration of 0.05 mol L^{-1} $NaNO_3$ at the catholyte.

To determine the NO_3^- rate orders to NH_3, we extracted them by obtaining j_{NH3} for different $NaNO_3$ concentrations, ranging from 0.005 to 0.05 mol L^{-1}. Being the current density a quantity that expresses the rate of electron-transfer reactions, we can assume a rate law for NO_3RR to NH_3 expressed as the following Eq. 2.1:

$$\text{rate} \propto \left|j_{NH_3}\right| = k\,[NO_3^-]^{\alpha} \ldots \qquad \text{(Eq. 2.1)}$$

Being 'k' the rate constant and 'α' the NO_3^- rate order to NH_3. Thus, we obtained α given by the slope of the relationship between *log* ($|j_{NH3}|$) *vs. log* ($[NO_3^-]$), as shown in Eq. 2.2.

$$\log(|j_{NH_3}|) = \alpha \log([NO_3^-]) + \log(k) + \cdots \qquad \text{(Eq. 2.2)}$$

We used four different catalysts as WE, for three of them by changing the duration of previous reduction steps on the Cu/Cu_2O composite (as-prepared, 10 minutes and 10 hours), and

we also evaluated the performance of a pure metallic Cu plate (200 nm deposited on Ti 10 nm at a silicon wafer). For each experiment of the catalysts derived from the Cu/Cu_2O composite, a new electrode was prepared as described in subsection 2.2.1. The previous reduction step consists of a potentiostatic application of – 1.0 V *vs.* SHE under the same conditions described for the electrolysis but in the absence of NO_3^-. Linear sweep voltammetries were conducted using the same setup for electrolysis from the open circuit potential (0.1 V *vs.* SHE) to −1.2 V *vs.* SHE at a scan rate of 20 mV s^{-1}.

The applied potentials were corrected against SHE (E_{SHE}) from the applied potential *vs.* Ag/AgCl ($E_{Ag/AgCl}$) through the Eq. 2.3:

$$E_{SHE} = E_{Ag/AgCl} + E^0_{Ag/AgCl} \quad \text{(Eq. 2.3)}$$

In Eq. 2.3, $E^0_{Ag/AgCl}$ is the standard potential for the Ag/AgCl RE against SHE at 25°C, which was previously calibrated to 0.218 V *vs.* SHE. The potentials reported against reversible hydrogen electrode (RHE), E_{RHE}, were corrected through the Eq. 2.4:

$$E_{RHE} = E_{Ag/AgCl} + E^0_{Ag/AgCl} + 0.059\ V\ pH \quad \text{(Eq. 2.4)}$$

All electrochemical kinetic and deposition measurements were conducted using a Biologic SP-150 potentiostat.

2.2.3 Protocols for Quantification and Detection of NH_3 and NO_2^-

We used the indophenol blue method to quantify NH_3. Our protocol consisted of diluting 500 µL of the sample with 2.5 mL of H_2O, in which we added 500 µL of 0.4 mol L^{-1} sodium salicylate (ACS reagent, >99%, Sigma Aldrich) + 0.32 mol L^{-1} NaOH, 50 µL of a 1% (w/w) sodium nitroprusside dihydrate solution and 50 µL of a sodium hypochlorite solution (reagent grade 4.00-4.99 % available chlorine). The final solution must rest for 1 hour before the measurement. The UV-Vis spectra were recorded from 500 to 800 nm (Figure A3a) with the Evolution 350 UV-Vis (ThermoScientific), and we used absorbance used to build the calibration curve was 657 nm (Figure A3b).

The colorimetric methods for NH_3 quantification are questioned in the literature due to the impact of some interferents in the measured absorbance that leads to false positives, especially for nitrogen reduction experiments.[89–91] In our quantification protocol, we used a blank similar to the fresh electrolyte to avoid those influences and to not misinterpret the results. Additionally, we

performed ^{1}H nuclear magnetic resonance (NMR) analysis of NH_4^+ species formed from electrolysis using both $Na^{14}NO_3$ and $Na^{15}NO_3$ (98 atom% ^{15}N) to verify whether the produced NH_3 was indeed formed from NO_3^- species. To do so, the produced NH_3 from 1 hour-electrolysis at −0.8 V *vs.* SHE for both electrolytes (^{14}N and ^{15}N) was protonated at pH 3 to NH_4^+. Then, we transferred 550 µL of the acidified sample to a 5-mm NMR tube adding 100 µL of D_2O to adjust the locker of the spectrometer. We performed the ^{1}H at room temperature on a Bruker AVANCE III NMR spectrometer, at 11.7 Tesla, in which we observed the ^{1}H nuclei at 500.13 MHz. We acquired the spectra using a pulse sequence *zgesgp* (Bruker library). Figure A4 shows two different types of spectra, obtained with 2.4 mmol L^{-1} of $NaNO_3$ (a) and 24 mmol L^{-1} of $NaNO_3$ (b): the black lines are ascribed to $^{15}NH_4^+$ species and red lines to $^{14}NH_4^+$, which shows a typical triplet.[92,93] The difference between the isotopes is due to the different values of the spin for each nucleus of ^{14}N and ^{15}N, being 1 and ½ respectively.[94] Then we were able to determine that the produced NH_3 came from NO_3^- species. The NMR experiments were conducted in collaboration with Dr. Maria F. C. Santos and Prof. Dr. Cláudio Tormena from the Institute of Chemistry of the University of Campinas.

We used the Griess method to quantify NO_2^- from NO_3RR of the catholyte after electrolysis experiments.[44] We diluted 500 µL of the sample in 2.5 mL of H_2O, mixing with 500 µL of the Griess reagent. This reagent consists of a solution containing 0.1 g of *N*-(1-naphthyl)ethylenediamine hydrochloride (ACS reagent, >98%, Sigma Aldrich) + 1.0 g of sulfanilamide (Fisher Chemical) + 2.94 mL of phosphoric acid (ACS reagent, >85%, Sigma Aldrich) in 50 mL of ultrapure water. We measured UV-Vis spectra from 400 to 800 nm (Figure A3c) with the Evolution 350 UV-Vis (ThermoScientific), using the absorbance at 540 nm build the calibration curve for NO_2^- quantification employing the same solution electrolytes used for the samples (Figure A3d).

2.2.4 Faradaic Efficiencies and Partial Current Densities

Knowing the concentrations of NO_2^- and NH_3, we can determine their Faradaic efficiencies (FEs) from NO_3RR, i.e., the ratio of the total charge transferred that was used to produce them. The Eq. 2.5 shows how we can calculate this parameter:

$$FE = \frac{n \cdot F \cdot [P] \cdot V_{cat}}{Q_{total}} \cdot 100\% \qquad \text{(Eq. 2.5)}$$

In Eq. 2.5, the numerator denotes the charge used to electrochemically form such product 'P', and 'Q_{total}' indicates the total charge that was transferred during the electrolysis, which is calculated by the integration of the current *vs.* time chronoamperometric experiments. In Eq. 2.5, 'n' is the number of electrons transferred (2 for NO_2^- and 8 for NH_3), 'F' is the Faraday constant (total charge of 1 mol of electrons, 96485 C mol^{-1}), '[P]' the concentration of either NO_2^- or NH_3 in the catholyte and 'V_{cat}' the catholyte's volume (0.04 L).

The partial current density is obtained by multiplying the FE with the total steady-state current density (*j*). The total current was normalized by the electrochemically active surface area (ECSA) to obtain *j*, which was determined as described in the next subsection.

2.2.5 Electrochemically Active Surface Area Determination

We calculated the electrochemically active surface area (ECSA) by obtaining the double-layer capacitance (C_{dl}) from the slope of the capacitive current recorded from CVs around the OCP (± 50 mV) (red line in Figure A5b) *vs.* the scan rate of the CV (Figure A5c). Knowing the C_{dl}, we can calculate the ECSA with Eq. 2.6.

$$\mathrm{ECSA} = \frac{\mathrm{C_{dl}}}{\mathrm{C_{specific}}} \qquad \text{(Eq. 2.6)}$$

In Eq. 2.6, '$C_{specific}$' is the specific capacitance, which is an intrinsic property of materials related to their electric properties. We measured the $C_{specific}$ of a flat copper plate under the same conditions to consider this value to measure the ECSA of the catalysts (Figure A5a). We start with a mixture of Cu and Cu_2O, and the presence of an interface between them generates a pseudo-capacitance that overestimates the C_{dl}. We measured how the ECSA changes over time for the tested conditions, as shown in Figure 2.1.

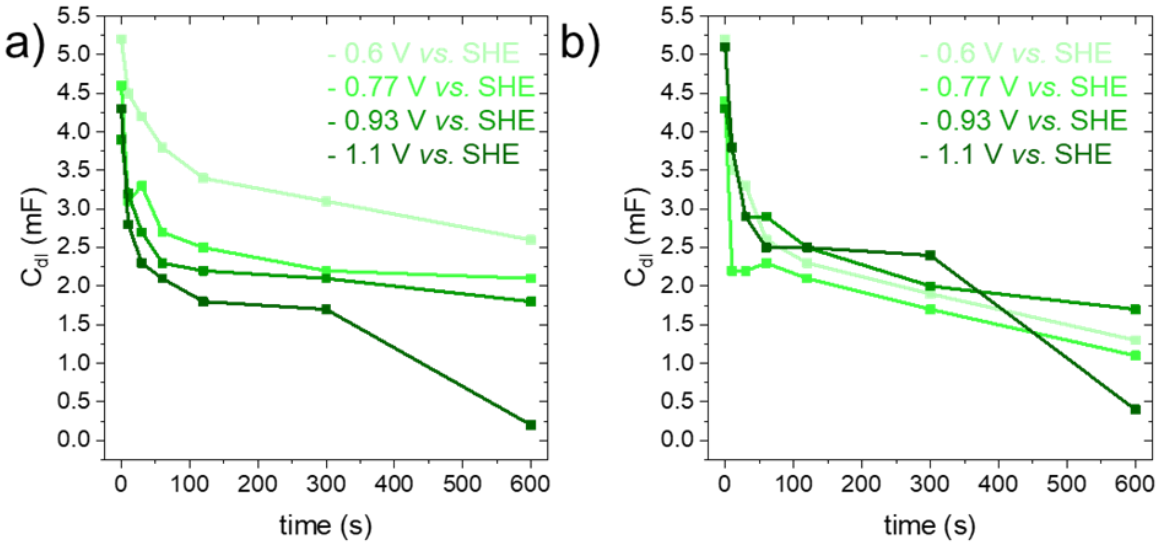

Figure 2.1. Double layer capacitance measurements over time for electrolysis at different applied potentials of Cu/Cu_2O composite. Electrolyte consists of 0.5 mol L^{-1} Na_2SO_4 in the absence (a) and presence (b) of 0.05 mol L^{-1} $NaNO_3$.

Examining the profile of C_{dl} over time, we detected a significant decrease under tested conditions both in the absence (Figure 2.1a) and presence (Figure 2.1b) of NO_3^-. Considering this variation, we calculated the ECSA with the C_{dl} measured after the electrolysis.

2.2.6 *Ex-situ* Characterizations

We performed some microscopic and spectroscopic characterizations of the as-prepared Cu/Cu_2O catalyst deposited as described in subsection 2.2.1 as well as a sample of the material after 1h-electrolysis at −0.77 V *vs.* SHE in non-buffered electrolyte under the conditions described in subsection 2.2.2. These characterizations were conducted in conjunction with Dr. João Batista Souza Junior from the Brazilian Nanotechnology National Laboratory (LNNano), part of the Brazilian Center for Research in Energy Materials (CNPEM).

We acquired scanning electron microscopy (SEM) images with Quanta 650 FEG microscope by the detection of secondary electrons by Everhart-Thornley detector, applying 20 kV with a working distance of 6.0 mm and horizontal field of 2.98 µm.

Transmission electron microscopy (TEM) images were acquired with a JEOL JEM-2100 microscope equipped with a LaB_6 electron gun, 200 kV as accelerating voltage for TEM and scanning TEM (STEM) modes, spatial resolutions equal to 0.25 and 1 nm respectively.

Atomic force microscopy (AFM) and Kelvin probe force microscopy (KPFM) maps were obtained with the NX10-ParkSystems equipment. We used an AFM tip recovered with Pt/Ir from NanoSensors, with a spring constant equal to 2.8 N m^{-2} and resonance frequency of 75 kHz. We scanned an area of 25 μm^2.

The X-ray photoelectron spectroscopy (XPS) experiments were conducted in a Thermo Scientific Al K-α X-ray excited photoelectron spectrometer. The spectra were obtained with 10 scans for a time of 3 minutes and 20.5 seconds. The spot size was 300 μm, the pass energy was 50.0 eV, and energy step size of 0.100 eV.

2.2.7 *In-situ* Raman Spectroscopy

The experiments of *in-situ* Raman spectroscopy were performed using a Renishaw InVia microscope spectrometer with a 633 laser. We used a homemade spectro-electrochemical cell (SEC) as shown in Figure A2c, assembled with a quartz window and in a 3-electrode configuration, in which the Cu/Cu_2O on Au was the WE, a leakless Ag/AgCl was the RE and a Pt wire was the CE.

The Raman spectra were acquired by the accumulation of 16 scans, with 100% laser power, and 1 second of exposure time at selected potentials. We recorded the spectra during chronoamperometric measurements with an electrolyte containing 0.5 mol L^{-1} Na_2SO_4 + 0.1 mol L^{-1} $NaNO_3$ from 0.0 to −1.0 V *vs.* SHE with a step 100 mV. The potentiostat used for these experiments was WaveNow from Pine Research performed at the Department of Chemistry of the University of Michigan.

2.2.8 *In-situ* X-ray Fluorescence, Absorption and Spectromicroscopy

We conducted *in-situ* X-ray absorption near edge spectroscopy (XANES) and spectromicroscopy experiments in the Carnaúba beamline (Tarumã station) at Sirius synchrotron light source of the Brazilian laboratory of synchrotron light (LNLS). We used a nanoprobe with a beam size of 200 x 500 nm^2 with an estimated flux of 10^9 photons/second on the sample. We carried out X-ray fluorescence mapping (nano-XRF) in continuous scan mode (flyscan) over an area of 50 x 50 μm with a step size of 500 nm^2 (pixel size) by scanning the sample.[95] Punctual XANES measurements were performed with a four-bounce Si (111) monochromator with an energy resolution of 10^{-4} keV at a step of 0.5 eV.

With XRF and energy scan, XANES maps were obtained by acquiring XRF images from 8974 eV to 9000 eV in the step of 0.5 eV, in which by stacking all XRF maps we can obtain the XANES map, where each pixel corresponds to a XANES spectrum. The concentration maps were obtained with an in-house development CORAL (Curve ResOlution foR dAta anaLysis), based on principal component analysis (PCA).[96] Both punctual spectra and XANES maps were collected during chronoamperometric experiments at selected potentials, using the as-prepared Cu/Cu_2O as WE, Pt wire as CE, and a leakless Ag/AgCl as RE, electrolyte containing 0.5 mol L^{-1} Na_2SO_4 + 0.1 mol L^{-1} $NaNO_3$. We used the potentiostat EC301 from Stanford Research Systems. The experiments in the Carnaúba beamline as well as the construction of the XANES maps were done in collaboration with Dr. Itamar Neckel from LNLS/CNPEM.

2.2.9 *In-situ* Fourier Transform Infrared Spectroscopy

We performed *in-situ* Fourier transform infrared spectroscopy (FTIR) using a Shimadzu IR prestige-21 spectrometer with a mercury-cadmium-telluride (MCT) detector refrigerated with liquid N_2. The SEC used for FTIR experiments (Figure A2b) consists of a 3 electrode cell (WE = Cu/Cu_2O on Au / Cu rod; CE = Pt wire; RE = RHE; electrolyte: 0.5 mol L^{-1} Na_2SO_4 + 0.024 mol L^{-1} $NaNO_3$) was assembled on top of a CaF_2 window and positioned on the upper part of a specular reflection accessory (Pike Technologies model VeeMax II). The FTIR spectra were acquired in external reflection mode from a thin layer formed by the careful pressure of the WE against the CaF_2 window. We used a PGSTAT 204 potentiostat (Autolab) to conduct chronoamperometric experiments from −0.3 to −1.2 V *vs.* SHE (at every 100 mV) and compared to the reference potential (−0.35 V *vs*. SHE). We acquired the spectra from an average of 128 scans with a resolution of 8 cm^{-1}.

2.3 Results and Discussion

2.3.1 Synthesis Characterization of Cu/Cu_2O Catalyst

We electrochemically synthesized a nanostructured composite containing Cu and Cu_2O phases through a galvanostatic regime with alkaline (pH 9) Cu(II)-lactate electrolyte aiming to study the interface of Cu^0 and Cu_2O as a potential active site for NO_3RR.[87,97] Under specific pH conditions (8.0 – 10.5) of a Cu(II)-lactate electrolyte and applied current density (0.025 – 8.0 mA cm^{-2}),[87] spontaneous potential oscillations occur that lead to the alternated deposition of metallic

Cu and Cu_2O.[98] In Figure 2.2a we show the voltammetric profile of a gold electrode in the Cu(II)-lactate system, in which the peaks related to the reduction of Cu^{2+} to Cu^{+} and the oxidation of Cu^{+} to Cu^{2+} are at 0.33 and 0.02 V *vs.* SHE respectively.[87] We established a reproducible electrodeposition protocol in which we applied −0.75 mA cm^{-2} for one hour, as shown in the time series that presents the potential oscillations between −0.35 and −0.17 V *vs.* SHE over time in Figure 2.2b. This galvanostatic regime leads to the alternated deposition of Cu and Cu_2O on Au as the zoomed section from the red rectangle of Figure 2.2b schematizes in Figure 2.2c, which shows that we deposit mainly Cu_2O at less negative potentials and Cu + Cu_2O at more negative ones. The period of each oscillation is 24 seconds.

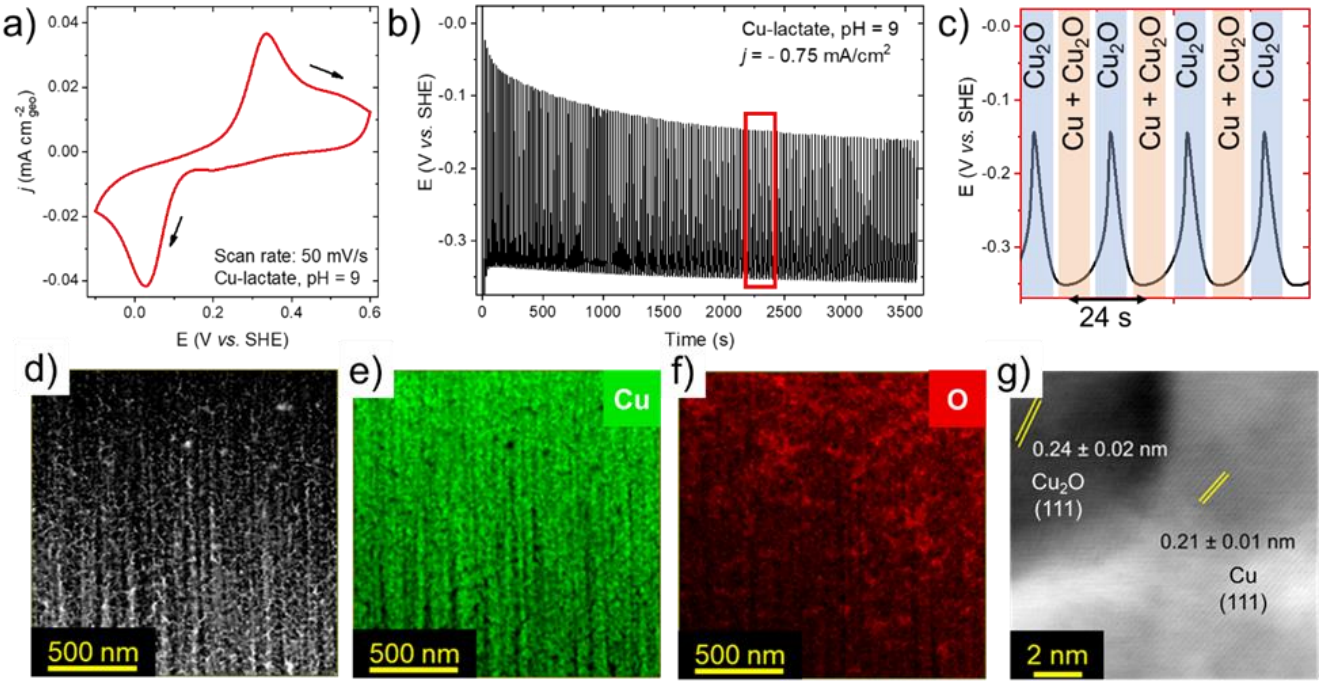

Figure 2.2. Electrochemical synthesis of Cu/Cu_2O and its characterization. (a) CVs from −0.1 to 0.6 V *vs.* SHE and following 1h galvanostatic deposition (time series shown in b) at −0.75 mA cm^{-2} of Cu/Cu_2O onto a gold plate as WE, graphite rod as CE and Ag/AgCl as RE. Electrolyte consists of 0.5 mol L^{-1} $CuSO_4$ + 2.5 mol L^{-1} lactate at pH 9.0. The red rectangle in (b) indicates the region of the time series shown in (c), which sketches the alternated deposition of Cu_2O and Cu + Cu_2O. (d) TEM image obtained from a FIB sampled lamella of Cu/Cu_2O. (e) EDS map for Cu and (f) O of the

region shown in (d). (g) High-resolution TEM image showing the lattice distance of Cu_2O and Cu phases.

We sampled a lamella from the Cu/Cu_2O composite using a focused ion beam (FIB) to characterize a cross-section of the deposited film with TEM and map the elementary distribution with energy dispersive X-ray spectroscopy (EDS). In Figure 2.2d we show the bright field TEM image of the cross-section of the Cu/Cu_2O, in which we could identify a porous structure along the deposit. We show in Figure 2.2e and Figure 2.2f the distribution of Cu and O, respectively, obtained by EDS from the same region imaged in Figure 2.2d. The distribution of Cu (Figure 2.2e) is homogeneous as expected considering both Cu and Cu_2O phases present Cu in their composition. The oxygen distribution along the deposit (Figure 2.2f) demonstrates that we have the formation of some domains with higher and lower amounts of O, ascribed to Cu_2O and Cu phases respectively. We used high-resolution TEM (Figure 2.2g) to confirm the formation of both phases by measuring the lattice distances of two different regions, the brighter one is ascribed to Cu (111) and the darker one to Cu_2O (111), whose lattice parameters are 0.21 and 0.24 nm respectively.[99] We also performed other characterizations of the as-prepared catalyst that will be presented in comparison with the Cu/Cu_2O after being submitted to NO_3RR in subsection 2.3.3.

2.3.2 Kinetic Evaluation of Pre-reduction Steps on Cu/Cu_2O for NO_3RR

We compared the kinetic performance of the three proposed active sites for NO_3RR to NH_3: the interface Cu/Cu_2O, oxygen vacancies on Cu_2O lattice, and pure Cu^0. To obtain a material that would contain these active sites, we employed different durations of a pre-reduction step before 10 minutes of electrolysis. We started with the as-prepared Cu/Cu_2O composite to test the interface metal-oxide as the potential active site. We previously reduced electrochemically the composite for 10 minutes and 10 hours from which we suggest that we would form oxygen vacancies and oxide-derived Cu respectively. The previous reduction consists of applying −1.0 V *vs.* SHE under the same electrolysis conditions, but in the absence of NO_3^-. Figure 2.3a displays the comparison of the NH_3 partial current densities from NO_3RR of the as-prepared Cu/Cu_2O with 10 minutes, 10 hours reduced Cu/Cu_2O, and a pure Cu^0 polycrystalline plate. The as-prepared and 10 min-reduced catalysts presented similar activity over the potential range tested (from −0.59 to −1.1 V *vs.* SHE). We attribute this similarity to the rapid reduction of Cu_2O which forms oxygen vacancies sufficiently quickly under these conditions so that we would not see differences between the as-

prepared and 10 min-reduced Cu/Cu_2O. Thus, the previous reduction of 10 minutes did not significantly change the activity of the Cu/Cu_2O composite. This finding suggests that the interface between Cu and Cu_2O is not the active site for NO_3RR to NH_3 at this potential range.

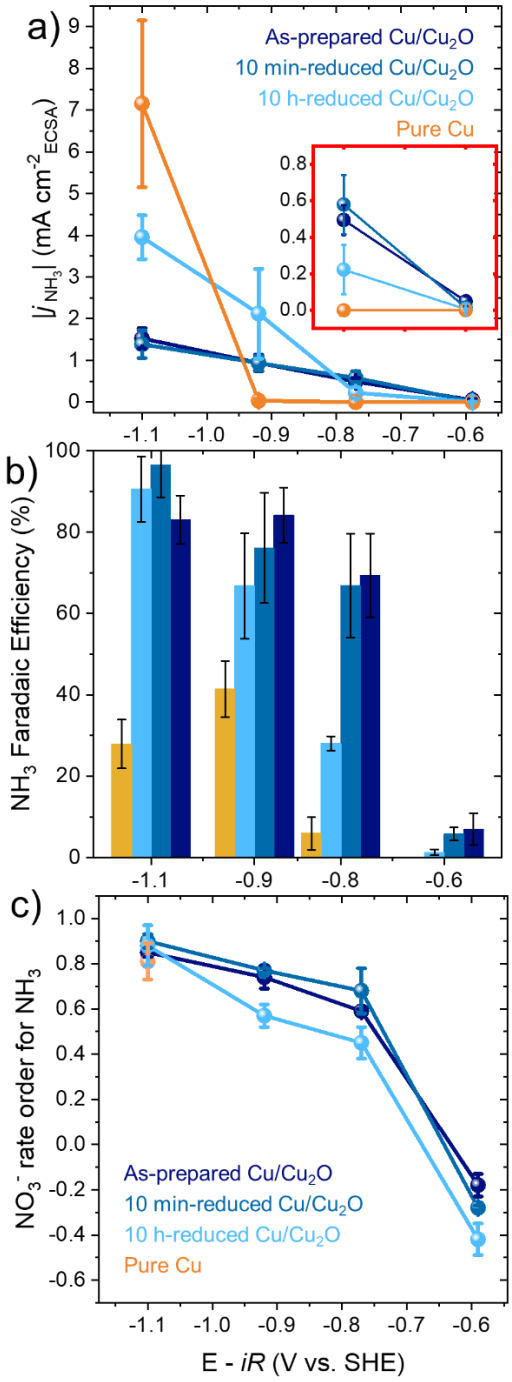

Figure 2.3. (a) NH_3 partial current densities, (b) Faradaic efficiencies toward NH_3 and (c) NO_3^- rate orders for NH_3 for as-prepared, 10 min-reduced and 10 h-reduced

Cu/Cu_2O (shades of blue) and pure Cu (orange). The results for (a) and (b) were obtained from 10 minutes of potentiostatic electrolysis with the catalyst as WE, graphite rod as CE and Ag/AgCl as RE, electrolyte containing 0.5 mol L^{-1} Na_2SO_4 adding 0.05 mol L^{-1} $NaNO_3$ in the catholyte. Rate orders shown in (c) were extracted from electrolysis under the same conditions as in (a) but with varying $NaNO_3$ concentrations from 0.005 to 0.05 mol L^{-1}. The error bars denote the standard deviation of at least three separate experiments.

The 10 h-reduced Cu/Cu_2O and pure Cu present lower activity for NH_3 at −0.59 and −0.77 V *vs.* SHE compared to as-prepared and 10 min-reduced Cu/Cu_2O (red square inset in Figure 2.3a). As we go to higher overpotentials, 10 h-reduced Cu/Cu_2O (oxide-derived Cu) is more active for NH_3 production than the others from −0.93 V *vs.* SHE and pure metallic Cu is the most active at −1.1 V *vs.* SHE. The higher activity of 10 h-reduced and pure Cu at larger overpotentials suggests that under high cathodic conditions, Cu^0 species are the active site for NO_3RR to NH_3. Considering that the 10 h-reduced Cu/Cu_2O has a rougher area compared to the flat Cu^0 electrode, the fact that the second one is more active than the oxide-derived Cu is attributed to the hampered mass transport of NO_3^- species toward the electrode in a rougher surface.[100] Thus, based on our activity results (Figure 2.3a), we suggest that at −1.1 V *vs*. SHE, Cu^0 is the active site for NO_3RR to NH_3.

When we compare the activities for NH_3 from NO_3RR normalized by ECSA (Figure 2.3a) with the ones normalized by geometric area (A_{geo}) (Figure A6), we see a major difference between the materials obtained from the Cu/Cu_2O and the metallic Cu due to the nanostructured composite surface. We will discuss morphology aspects of Cu/Cu_2O in subsection 2.3.3. We demonstrate that the materials derived from Cu/Cu_2O present a high roughness that would lead to misinterpretation if we had considered merely A_{geo} to compare their activities. We have shown in Figure 2.1 that the C_{dl} of Cu/Cu_2O decreases when applying negative potentials. We attribute this decrease to two phenomena. The first one is that the surface indeed changes its structure, which is reflected in the ECSA. The second one is the fact that since Cu_2O is quickly reduced, the pseudo-capacitance from the metal-oxide interface that overestimates the C_{dl} is suppressed.[101] We also measured the C_{dl} from metallic Cu before and after the electrolysis (Figure A7) and they did not change significantly, which indicates that Cu ECSA remains the same after electrolysis.

By examining the NH_3 FE (Figure 2.3b), which reflects the selectivity of an electrochemical reaction, the as-prepared and 10 min-reduced Cu/Cu_2O are more selective toward NH_3 at low overpotentials (−0.59 to −0.77 V vs. SHE) and all Cu_2O-derived catalysts are equally selective at higher ones (shades of blue in Figure 2.3b at −0.93 to −1.1 V vs. SHE). For those materials, we attribute the remaining FE to the production of NO_2^-, as we show in Figure A8. This trend for Cu_2O-containing materials follows the potential dependence seen in Figure 2.3a, in which the as-prepared and 10 min-reduced Cu/Cu_2O are more active to NH_3 than 10 h-reduced Cu/Cu_2O from −0.59 to −0.77 V vs. SHE and less active from −0.93 to −1.1 V vs. SHE.

Metallic Cu^0 is less selective to NH_3 than all the Cu_2O-derived catalysts over the entire potential range (orange bars in Figure 2.3b). We attribute the lower NH_3 FE of Cu^0 at −1.1 V vs. SHE, despite its highest activity toward NH_3 at this potential, (Figure 2.3a) to the competing HER, since we did not detect considerable amounts of NO_2^- under this condition (Figure A9). We explain this lower selectivity of the metallic Cu catalyst with different hypotheses. The first one is that we must have different facet distributions for oxide-derived and pristine Cu. Since the Cu produced from Cu_2O can present different proportions of crystalline orientations than metallic Cu, promoted by the previous reduction that can lead to a preferential and more active orientation.[35] Besides that, it has been studied that less coordinated Cu atoms can serve as more selective active sites for NH_3 than higher coordinated ones,[39,60] which can be the case for Cu_2O-derived catalysts.[67] Additionally, grain boundaries in the catalyst lattice can also be a potential active site for NO_3RR to NH_3,[102] which can be formed by the previous reduction of Cu_2O. Also, Anastasiadou *et al.*[55] demonstrated that starting from different Cu_2O-oriented nanocubes leads to differently active surfaces, where the Cu derived from Cu_2O (111) is more active than the one derived from Cu_2O (100).

We calculated the NO_3^- rate orders to NH_3 (Figure 2.3c) for the tested catalysts over the studied potentials, which shows us how increasing the concentration of NO_3^- impacts the NH_3 partial current density. Comparing the NO_3^- rate orders to NH_3 of the catalysts (Figure 2.3c), we found a similar trend for as-prepared and 10 min-reduced Cu/Cu_2O, which corroborates with what was previously obtained from both NH_3 activity (Figure 2.3a) and FE (Figure 2.3b) results. The 10 h-reduced Cu/Cu_2O exhibits slightly lower rate orders from −0.59 to −0.93 V vs. SHE, which means that for this potential range, the NH_3 activities of as-prepared and 10 min-reduced Cu/Cu_2O

are more sensitive to increasing NO_3^- concentration. At the most negative potential (−1.1 V vs. SHE) the NH_3 activities of all the catalysts, including metallic Cu, are equally sensitive to increasing NO_3^- concentration. We calculated the rate order for Cu only at −1.1 V vs. SHE due to the below quantifiable amounts of NH_3 produced with lower NO_3^- concentrations.

Interestingly, the NO_3^- rate orders to NH_3 for all catalysts were negative at −0.59 V vs. SHE (Figure 2.3c), which reflects the fact that at this potential, increasing the NO_3^- concentration indeed decreases NH_3 activity. At −0.59 V vs. SHE, we have the highest NO_2^- FE (Figure A8). We attribute the negative NO_3^- rate orders to NH_3 to the fact that by increasing NO_3^- concentrations we would be favoring the formation of NO_2^- first instead of the following production of NH_3. Thus, when we increase the NO_3^- concentration, more NO_3^- species would be available to be reduced to NO_2^- that would not be subsequently converted to NH_3.

As the concentration of NO_3^- increases, more NO_3^- species can interact with the active sites. However, if the active sites become saturated with increasing [NO_3^-], it would inhibit the reduction of NO_2^- to NH_3. If the inhibitory effect becomes significant, increasing [NO_3^-] would decrease the formation rate of NH_3, reflected by lower j_{NH3} at higher initial [NO_3^-]. Thus, the rate of the overall reaction, and consequently the rate order to NH_3 with respect to NO_3^- (α in Eq. 2.1) may decrease, leading to a negative rate order for NO_3^- in the production of NH_3.

Bai *et al*.[77] demonstrated that the Cu^+ sites are responsible for the conversion of NO_3^- to NO_2^- on Cu_2O nanocubes, while the Cu^0 atoms would be the active sites for the further conversion to NH_3, which can explain our highest NO_2^- FE at the lowest overpotential, the one that we would expect the higher presence of Cu^+.

2.3.3 Compositional and Structural Changes in the Catalyst after NO_3RR

We characterized the catalyst before and after NO_3RR with different microscopic and spectroscopic techniques to assess how the reaction conditions modify both catalyst structure and composition. We found with XPS and EDS (from SEM images) that Cu_2O from as-prepared Cu/Cu_2O was heavily reduced after 1 hour of electrolysis at −0.77 V *vs.* SHE (Figure 2.4a-d). Cu XPS spectrum of Cu_2O typically presents a satellite peak at 948 eV[53] related to Cu^+ species, as shown in the spectrum in Figure 2.4a for the as-prepared Cu/Cu_2O before the electrolysis. After the NO_3RR, we couldn't detect the presence of this satellite peak in the Cu XPS spectrum (Figure

2.4b). We also compared the 1s core level oxygen XPS spectra before (blue line) and after (orange line) the NO_3RR (Figure 2.4c). For these spectra, we attribute 3 peaks to 3 different origins of oxygen species: 530.4 eV attributed to Cu_2O lattice oxygen, 531.9 eV to O atoms from chemisorbed water molecules, and 533.9 eV to adsorbed O atoms.[103,104] We highlight that the peak centered in 530.4 eV is not present in the O XPS spectrum after the NO_3RR, demonstrating that the O atoms in the catalyst lattice were electrochemically removed, by the reduction of Cu_2O species. Additionally, the average EDS spectra (Figure 2.4d) obtained from same-sized areas of the Cu/Cu_2O before (blue line) and after (orange line) the NO_3RR also confirms the Cu_2O reduction. The peak centered in 0.52 keV relative to O species (inset in Figure 2.4d) significantly diminishes after the NO_3RR, indicating the removal of those atoms from the catalyst lattice.

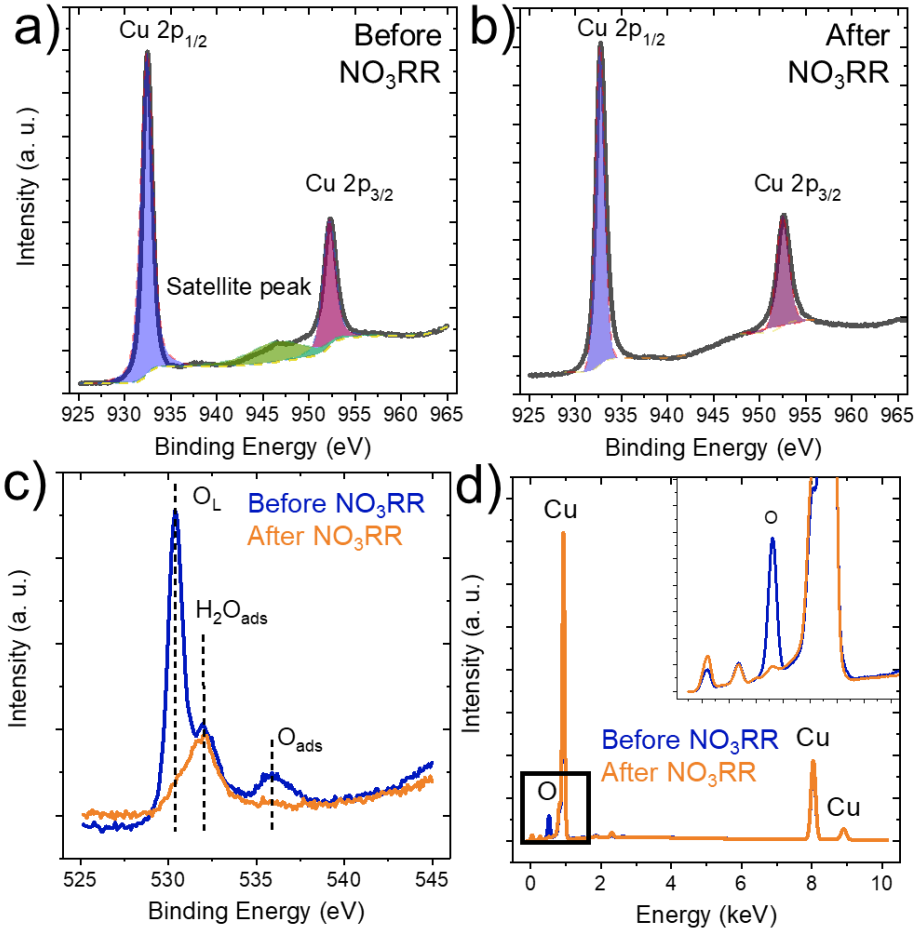

Figure 2.4. Cu/Cu_2O *ex-situ* spectroscopic characterizations. (a,b) Cu and (c) O XPS spectra and (d) EDS spectra for as-prepared Cu/Cu_2O (a, blue line in c, d) and after NO_3RR (b, orange line in c, d). Inset in (d) zoom in the O peak of EDS spectra. The

electrolysis was conducted for 1 hour at −0.77 V *vs.* SHE, electrolyte consisting of 0.5 mol L^{-1} Na_2SO_4 and catholyte with addition of 2.35 mmol L^{-1} $NaNO_3$.

Since oxygen is being removed from the catalyst lattice, due to the electrochemical reduction of Cu_2O under reaction conditions, we would expect structural changes in the Cu/Cu_2O after NO_3RR as well. In Figure 2.5a, we present a SEM image of the as-prepared Cu/Cu_2O catalyst, a porous nanometric surface with rounded structures with some cavities between them. After NO_3RR (Figure 2.5b), the corners of these well-defined structures are smoothed, leading to a less rough surface.

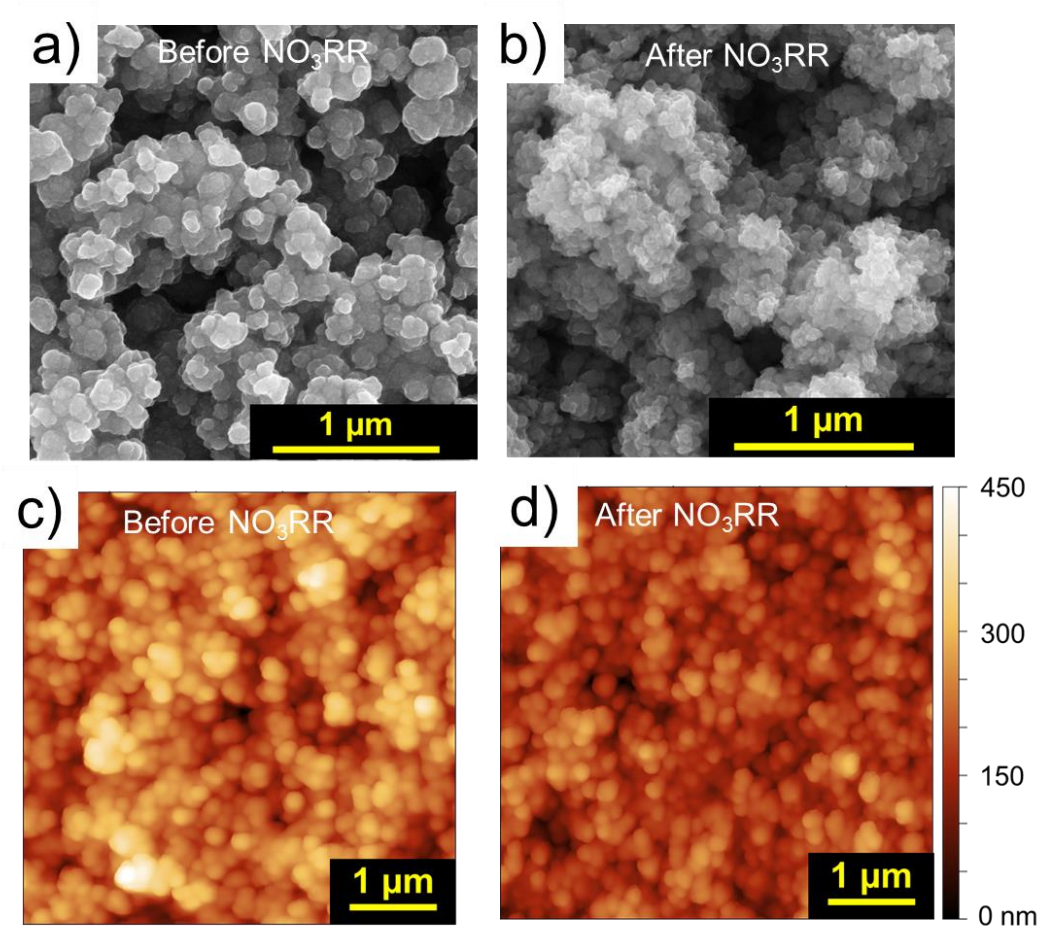

Figure 2.5. Cu/Cu_2O *ex-situ* characterizations. (a-b) SEM images and (c-d) AFM topology maps of the Cu/Cu_2O catalyst before (a,c) and after (b,d) NO_3RR. The electrolysis was conducted for 1 hour at −0.77 V *vs.* SHE, electrolyte consisting of 0.5 mol L^{-1} Na_2SO_4 and catholyte with addition of 2.35 mmol L^{-1} $NaNO_3$.

The smoothening of the Cu/Cu_2O surface is corroborated with the AFM topography maps obtained before (Figure 2.5c) and after (Figure 2.5d) the NO_3RR, from which the calculated average roughness decreased from 222.5 nm to 173.1 nm. We also extracted the surface contact potential with KPFM of the same area probed by AFM in Figure 2.4g-h (Figure A10) which confirms that the identity of the material changes after NO_3RR. The average contact potential shifted from 0.1957 to 0.038 V after the electrolysis. Under cathodic conditions, Cu_2O-based materials can change their structure through a dissolution-redeposition mechanism.[105] As such, Anastasiadou *et al.*[55] also reported structural changes in Cu_2O films after NO_3RR.

2.3.4 The Role of Cu_2O Reduction in NO_3RR to NH_3

We employed *in-situ* spectroscopies to track the presence of Cu_2O under operating NO_3RR conditions. The Raman spectra of Cu_2O typically present 4 major peaks: two centered at 145 and 630 cm^{-1} related to infrared active mode F_{1u} (T_{15}), one weak peak at 415 cm^{-1} attributed to multiphoton process, and one at 520 cm^{-1} ascribed to Raman allowed mode $^3T`_{25}$ (F_{2g}).[106] We probed the presence of Cu_2O by evaluating the evolution of these peaks from 0.0 to −1.0 V *vs.* SHE (Figure 2.6a). We observed that the peaks related to Cu_2O gradually diminish from −0.6 to −1.0 V *vs.* SHE. The cathodic voltammetric profile of Cu/Cu_2O conducted in the absence of NO_3^- (blue dotted line in Figure A1) presents a peak centered in −0.6 V *vs.* SHE, which we attribute to the electrochemical reduction of Cu_2O. Thus, we found that from −0.6 V *vs.* SHE onwards, Cu_2O electrochemically reduces.

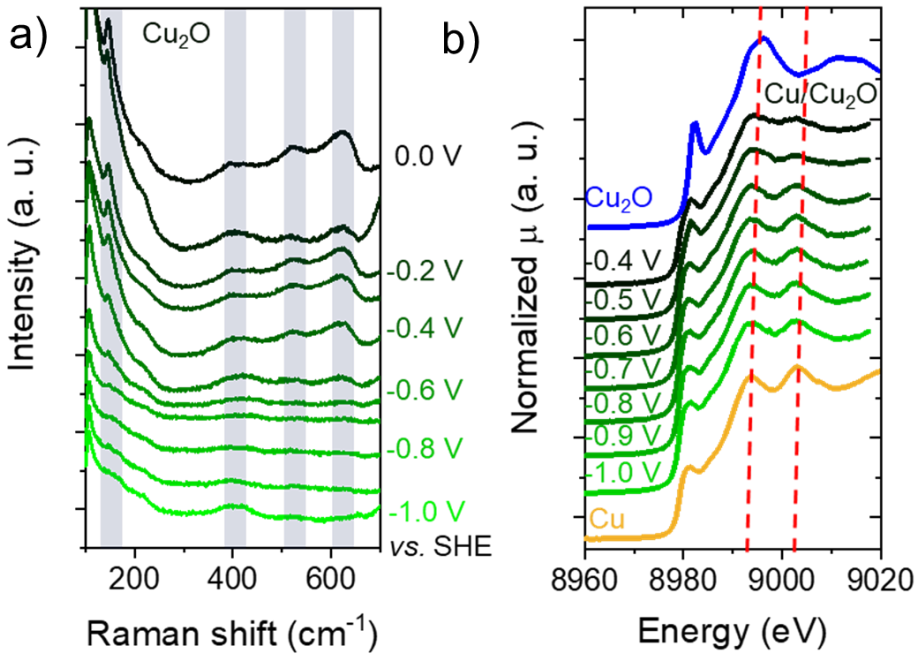

Figure 2.6. *In-situ* spectroscopies for Cu/Cu_2O characterizations. (a) Raman spectroscopy of Cu/Cu_2O under NO_3RR conditions from 0.0 to −1.0 V *vs.* SHE (shades of green), with the peaks related to Cu_2O highlighted in blue. (b) Punctual Cu *K*-edge XANES spectra for Cu foil (orange line), Cu_2O (blue line), and Cu/Cu_2O (shades of green) under different applied potentials. All measurements were conducted using Cu/Cu_2O on Au as WE with an electrolyte containing 0.1 mol L^{-1} $NaNO_3$ and 0.5 mol L^{-1} Na_2SO_4.

We performed punctual *in-situ* Cu *K*-edge XANES measurements (Figure 2.6b) to also track the potential-dependent transition of a catalyst that first consists of a composite containing Cu/Cu_2O to a material containing mainly metallic Cu^0. We compared the XANES spectra of Cu/Cu_2O under reaction conditions from −0.4 to −1.0 V *vs.* SHE (shades of green in Figure 2.6b) with the pure spectra of Cu and Cu_2O (orange and blue lines in Figure 2.6b). The position of the absorption edge, i.e., the energy from which the probed atom starts absorbing X-rays is usually the main descriptor used to determine the oxidation state of metals.[107] In our case, it is hard to use this parameter considering we cannot ensure whether we are probing a Cu or Cu_2O phase. We attribute the white line peak to the *1s* → *4p* transition of Cu *K*-edge XANES spectrum centered around 8980.5 eV.[108] Additionally, there are two peaks centered in 8993.5 and 9003 eV identified for the

pure Cu spectrum (red dotted lines in Figure 2.6b) that are related to X-ray scattering on the first and second coordination shells of Cu *fcc* metal lattice.[109] These post-edge peaks ascribed to Cu *fcc* become better defined from −0.6 to −1.0 V *vs.* SHE, indicating that the catalyst lattice is transitioning from a mixture of Cu/Cu_2O to metallic Cu within this potential range. These results agree with the Cu Pourbaix diagram,[70] from which we expect to get this transition in the potential range of 0.2 to −0.5 V vs. SHE, depending on the electrolyte pH.

We mapped the distribution of Cu oxidation state using XANES spectroscopy over an area of 2500 μm^2 of the Cu/Cu_2O catalyst at −0.8 (Figure 2.7a,b) and −1.0 V vs. SHE (Figure 2.7c,d). By using PCA through a stack of XRF images acquired over Cu *K*-edge XANES spectra, we extracted the maps *in situ* of Cu^+ (Figure 2.7a,c) and Cu^0 (Figure 2.7b,d) species.

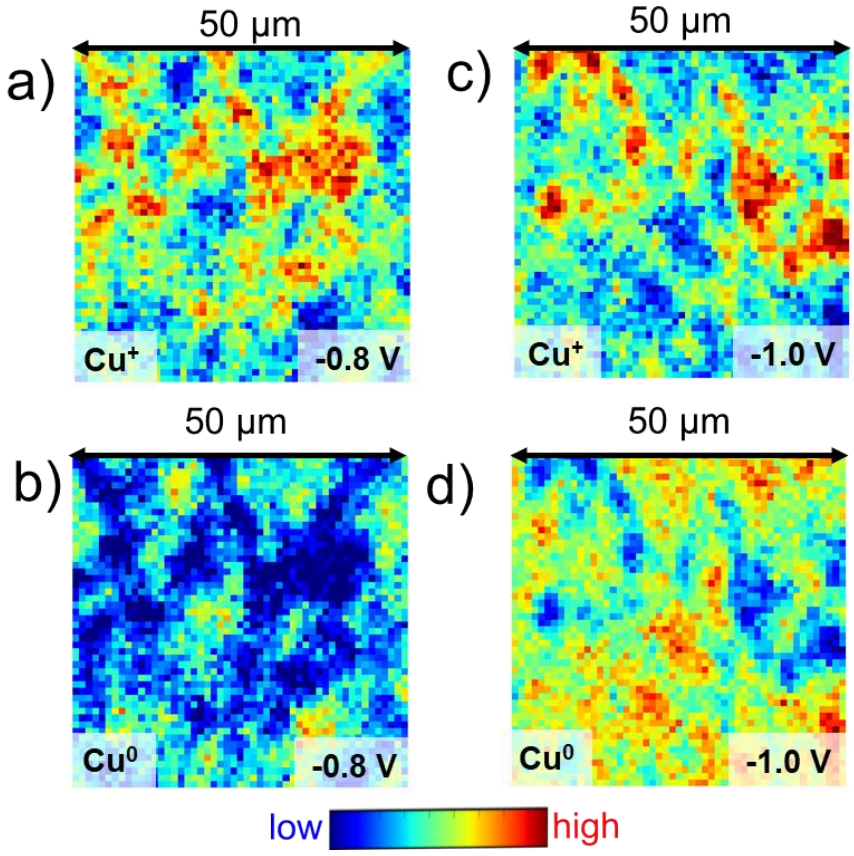

Figure 2.7. XANES maps for the distribution of oxidation states of Cu^+ (a,c) and Cu^0 (b-d) of 50 x 50 µm area of the catalyst obtained at (a,b) −0.8 and (c,d) −1.0 V vs. SHE. The measurements were conducted using Cu/Cu_2O on Au as WE with electrolyte containing 0.1 mol L^{-1} $NaNO_3$ and 0.5 mol L^{-1} Na_2SO_4.

Comparing the maps obtained at −0.8 and −1.0 V vs. SHE, we see that the quantity of Cu^+ species decreases, evidenced by the transition of the color of some pixels from orange in Figure 2.7a to blue/green in Figure 2.7c. When we examine the distribution of Cu^0 species, the transition is more evident, since a considerable region of the map shifts its colors from a predominantly blue distribution at −0.8 V vs. SHE (Figure 2.7b) to a more orange/yellow map −1.0 V vs. SHE (Figure 2.7d). These results corroborate with our kinetic results shown in subsection 2.3.2, where we attribute to Cu^0 the activity of Cu_2O-based catalysts for NO_3RR to NH_3 at higher overpotentials (−1.1 V vs. SHE). Although we have detected remaining Cu^+ species in the Cu/Cu_2O maps, we demonstrated that there is clear evidence that Cu oxidation states are shifting from +1 to 0 with the application of negative potentials during NO_3RR, which is also corroborated with *in-situ* Raman and XANES spectra (Figure 2.6).

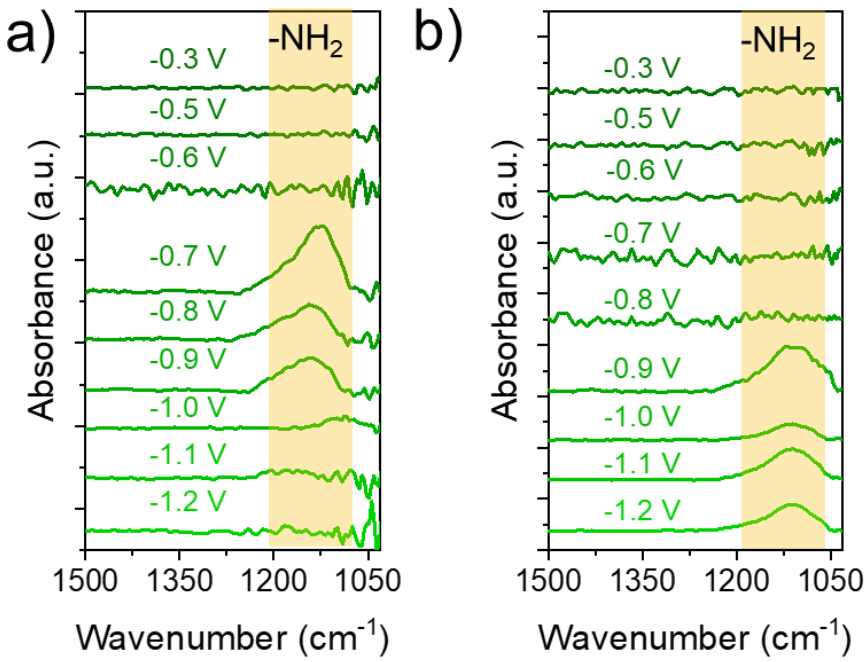

Figure 2.8. *In-situ* FTIR spectra for (a) Cu/Cu_2O and (b) a Cu rod as WE. Electrolyte consists of 0.1 mol L^{-1} $NaNO_3$ and 0.5 mol L^{-1} Na_2SO_4. The peak centered at 1111 cm^{-1} (yellow) related to $-NH_2$ from NH_2OH is highlighted in yellow.

We used *in-situ* FTIR to track the formation of NH_2OH (Figure 2.8), which is a key intermediate of NO_3RR to ammonia (Figure 1.4). We ascribe the peak centered in 1111 cm^{-1} to the $-NH_2$ stretch of NH_2OH.[110] We show that NH_2OH is formed at −0.7 V vs. SHE and consumed at

−1.0 V vs. SHE on Cu/Cu_2O (Figure 2.8a), while on metallic Cu it is only formed at −0.9 V vs. SHE (Figure 2.8b). Previously, we demonstrated with Raman and XANES spectroscopies (Figure 2.6) that Cu_2O reduces at −0.6 V *vs.* SHE, which is a lower overpotential than those with higher FEs for NH_3 production (−0.77 to −1.1 V vs. SHE, Figure 2.3b). Then, the formation of NH_2OH from −0.7 to −0.9 V vs. SHE on the Cu/Cu_2O electrode suggests that NH_3 is formed from this species, which follows the expected mechanism for Cu-based catalysts.[35,51,111] As we see in Figure 2.8b, the formation of NH_2OH at metallic Cu requires a higher overpotential than on Cu/Cu_2O to occur. Since we have suggested based on our kinetic results (Figure 2.3) that oxygen vacancies are the active site for NO_3RR to NH_3 from −0.59 to −0.77 V *vs.* SHE, we attribute this lower overpotential to the presence of these oxygen vacancies in the catalyst lattice. We discuss in subsection 2.3.5 how the attribution that we gave to the potential dependence on the active site of Cu/Cu_2O is in context with the current literature.

2.3.5 The Active Site of Cu_2O-based Materials for NO_3RR

While previous studies have suggested that the interface between Cu and Cu_2O plays a pivotal role in NO_3RR to NH_3, our research indicates that in the conditions under which we have a favorable conversion of NO_3^- to NH_3, Cu_2O reduces. Wang *et al.*[62] linked the NO_3RR activity of CuO nanowires to the "*in-situ*" formation of the interface of Cu/Cu_2O at higher overpotentials. This work also utilized 0.5 mol L^{-1} Na_2SO_4 electrolyte and assessed the catalyst performance across a similar potential range as our study (−0.55 to −0.95 V *vs.* RHE, equivalent to −0.9 to −1.3 V *vs.* SHE, at the reported initial pH). They used DFT analysis to propose that the Cu/Cu_2O interface promotes the formation of $NOH_{(ads)}$ which is subsequently hydrogenated to NH_2OH. We demonstrated that NH_2OH indeed forms at −0.7 V *vs.* SHE, but in our case, we attribute this facilitated formation on Cu/Cu_2O to the presence of oxygen vacancies in the catalyst lattice.

Shen *et al.*[59] suggested that the Cu^0–Cu^+ interfaces facilitate NO_3RR to NH_3 by initially converting NO_3^- to NO_2^- on Cu^0 sites and reducing NO_2^- to NH_3 on Cu^+ ones. This proposal contradicts our results that show higher FEs for NO_2^- at lower overpotentials (Figure A8), where we expect to have more Cu^+ sites. Our results follow what was proposed by Bai *et al.*[77] that suggests that the formation of NO_2^- occurs in Cu^+ sites while the Cu^0 promotes the further conversion to NH_3. Other several proposals suggest the presence of Cu_2O species at the cathodic conditions under which we would expect their reduction.[58,63,68,112,113] Since our kinetic results for

the 10 min-reduced Cu/Cu_2O are similar to the as-prepared catalyst (Figure 2.3), we do not attribute NH_3 formation from NO_3RR to any presence of Cu^+ species under reaction conditions.

Daiyan *et al.*[64] ascribe the improved efficacy of Cu_2O-based catalysts for NO_3RR to NH_3 to the presence of oxygen vacancies in the catalyst lattice, which is supported by our findings for potentials from −0.59 to −0.77 V *vs.* SHE. Employing DFT, they found that oxygen vacancies promote the formation of the intermediate $NHO_{2(ads)}$, which is subsequently reduced to $NO_{(ads)}$, $NHO_{(ads)}$, and $NH_2O_{(ads)}$ intermediates. Then, the conversion to NH_3 follows the reduction of $NH_2O_{(ads)}$ through a proton-electron transfer, concurrently forming $O_{(ads)}$. Our kinetic results (Figure 2.3) corroborates with this hypothesis within the −0.59 to −0.77 V *vs.* SHE potential range, where oxygen vacancies serve a pivotal role in stabilizing intermediates and also favor the formation of NH_2HO, as we demonstrate with *in-situ* FTIR (Figure 2.8). Although we have detected improved NH_3 activities and FE on the catalyst containing oxygen vacancies from −0.59 to −0.77 V *vs.* SHE, we found that at higher overpotentials (−1.1 V *vs.* SHE) Cu^0 overperformed the vacancy-rich Cu/Cu_2O.

Between −0.93 to −1.1 V *vs.* SHE, oxygen vacancies do not exert a beneficial impact on the formation NH_3 (Figure 2.3), which aligns with Li *et al.*[65] that attribute the enhanced activity and selectivity of CuO-derived Cu nanotubes to their distinctive architecture and structure. This study reported an optimal selectivity toward NH_3 at −1.3 V *vs.* saturated calomel electrode (SCE) (approximately −1.0 V *vs.* SHE). This potential is within the range that our work found higher activity of NO_3RR to NH_3 from 10-hour-reduced Cu/Cu_2O (Figure 2.3a), which is attributed to the complete reduction of Cu_2O. Moreover, when we examine the NH_3 activities derived from the geometric area (Figure A6), the lower activity of pure Cu compared to Cu_2O-based catalysts is attributed to the highly roughened surface obtained from Cu/Cu_2O reduction, which agrees with what was reported by Li *et al.*[65] Additionally, it is important to consider that Cu_2O reduction can trigger a dissolution-redeposition mechanism that can form more active phases under a cathodic regime.[55,105]

Agreeing with our results, Zhou *et al.*[67] also noted a potential-dependent behavior of the active sites of Cu_2O-based catalysts for NO_3RR. They observed that at potentials more negative than −0.6 V *vs.* RHE (equivalent to −1.0 V *vs.* SHE, at pH 7), oxide-derived Cu serves as the active phase for NO_3RR to NH_3. At lower overpotentials, they attribute the Cu/Cu_2O interface as the

preferred site for NO_3RR to NO_2^-. We found the highest activity for NH_3 at −1.1 V *vs.* SHE and for NO_2^-, Cu/Cu_2O presented its highest FE at −0.6 V *vs.* SHE (Figure A8), both agreeing with what was reported by Zhou *et al.*[67] However, we associate the enhanced NH_3 production at −0.77 V *vs.* SHE of Cu/Cu_2O with oxygen vacancy, a hypothesis that was not explored by Zhou and co-workers.[67] Then, our approach presents a novel proposal of potential-dependent active sites of Cu/Cu_2O for NO_3RR to NH_3, as Table 2.1 demonstrates.

Table 2.1. Proposed active sites of Cu_2O-based catalysts for NO_3RR to NH_3 by the literature. Bolded is what was suggested by our work.[32]

Catalyst	Electrolyte	Proposed active site	Ref.
CuO nanowires converted into Cu/Cu_2O	0.5 mol L^{-1} Na_2SO_4 14.3 mmol L^{-1} $NaNO_3$	Cu/Cu_2O interface	[62]
Cu_2O/Cu foam	0.1 mol L^{-1} Na_2SO_4 12.87 mmol L^{-1} $NaNO_3$	Cu^0 for NO_3RR to NO_2^- and Cu^+ for NH_3 formation	[59]
Cu_2O nanocubes	0.1 mol L^{-1} Na_2SO_4 (pH 12) 21.4 mmol L^{-1} $NaNO_3$	Cu^+ for NO_3RR to NO_2^- and Cu^0 for NH_3 formation	[77]
"Island-like" Cu electrodeposited at Ni	0.5 mol L^{-1} Na_2SO_4 0.05 mol L^{-1} KNO_3	Stable Cu(I) species	[68]
Cu_2O converted into Cu/Cu_2O nanorods	0.1 mol L^{-1} Na_2SO_4 2.14 mmol L^{-1} $NaNO_3$	Interface of metal/oxide	[113]
Oxide-derived Cu foam	1 mol L^{-1} KOH 1 - 100 mmol L^{-1} KNO_3	Cu^+ sites inhibit the competing HER	[58]
Ag/Cu_xO nanoparticles	0.5 mol L^{-1} Na_2SO_4 7.15 mmol L^{-1} $NaNO_3$	Interface between Ag and Cu_2O	[63]
Cu/Cu_2O microspheres	0.1 mol L^{-1} Na_2SO_4 21.4 mmol L^{-1} $NaNO_3$	Cu_2O (111) facets	[112]
Plasma treated CuO	0.1 mol L^{-1} H_2SO_4 0.05 mol L^{-1} KNO_3	Oxygen vacancies improve intermediates' adsorption	[64]
CuO nanotube *in-situ* reduced to Cu	0.5 mol L^{-1} K_2SO_4 3.6 mmol L^{-1} KNO_3	Cu^0 is intrinsically active	[65]
Electrochemically reconstituted Cu/Cu_2O	0.1 mol L^{-1} PB 0.1 mol L^{-1} KNO_3	Interface Cu/Cu_2O or Cu^0 (potential-dependent)	[67]
Electrodeposited Cu/Cu_2O	**0.5 mol L^{-1} Na_2SO_4 50 mmol L^{-1} $NaNO_3$**	**Oxygen vacancies or Cu^0 (potential-dependent)**	[32]

In Table 2.1, we also introduce another variable that needs to be addressed to better evaluate the activity of Cu_2O-based catalysts for NO_3RR: the electrolyte. For the results reported so far, we have employed a non-buffered mildly acidic electrolyte containing Na_2SO_4, considering most of the water streams that can serve as a feedstock for NO_3RR are unbuffered solutions.[14,20] Additionally, as we see in Table 2.1, sulfate-based electrolytes are the most used ones for this reaction, due to the less favorable adsorption of sulfates onto the catalyst. However, by utilizing non-buffered electrolytes for a highly proton-consuming reaction, we can change its pH over time.[32] In the next subsection 2.3.6, we discuss the effect of pH changes of Na_2SO_4 electrolyte on NO_3RR to NH_3.

2.3.6 Effect of pH Changes of Non-buffered Electrolyte on NO_3RR to NH_3

Employing a non-buffered Na_2SO_4 electrolyte, we detected an alkaline shift in the catholyte pH from 5.8 to up to 12 within 10 minutes of electrolysis. We show in Figure A11 how both catholyte and anolyte pHs change over time during the NO_3RR at −0.93 V *vs.* SHE. This alkaline shift in the catholyte pH was detected at all tested potentials, as the black arrow in Figure 2.9a illustrates. Since we have seen that the non-buffered electrolyte pH is dynamic, we report our results on the SHE scale, which is not pH-dependent. We attribute the pH increase of the catholyte containing Na_2SO_4 to the fact that the electrochemical conversion of NO_3^- to NH_3 can either consume 10 moles of $H_3O^+_{(aq)}$ (Eq. 1.1) or release 9 moles of $OH^-_{(aq)}$ (Eq. 1.2) depending on the solution pH.[17] This pH shift can impact both the NO_3RR mechanisms and the catalyst performance, as we have discussed in section 1.3. To explore how this alkalinization is impacting the NO_3RR kinetics, we compared in Figure 2.9 the Cu/Cu_2O electrocatalytic performance on the unbuffered Na_2SO_4 (light red bars and line) solution with PB at fixed pH 5.8 (golden bars and line) along with alkalized Na_2SO_4 (dark red bars and line). We did not detect any significant pH change after NO_3RR employing both PB and alkalized Na_2SO_4 electrolyte (dark red and golden bars in Figure 2.9a, respectively). This pH shift cannot only be attributed to the weak capacity of the Nafion membrane to exchange protons since we detected a quick pH shift (from 5.8 to 10 within 1-min electrolysis) when using a 1-compartment electrochemical cell. For this reason, we consider that this alkalinization also occurs during the *in-situ* measurements presented in subsection 2.3.4.

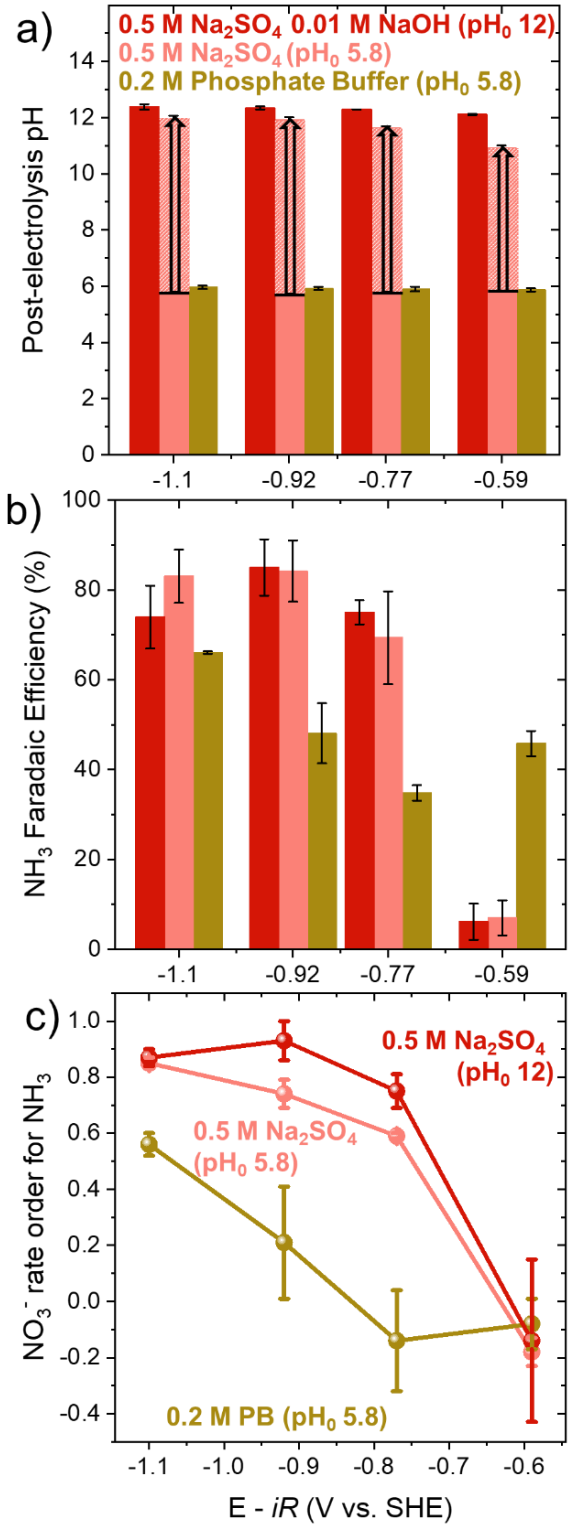

Figure 2.9. pH of the catholyte measured after the NO_3RR (a), NH_3 FEs (b) and NO_3^- rate orders to NH_3 for alkalized (dark red), non-buffered (light red) 0.5 mol L^{-1} Na_2SO_4

and 0.2 mol L^{-1} PB (golden) electrolytes in terms of applied potential. Electrolysis conditions: 10 min, with the addition of 5 to 50 mmol L^{-1} $NaNO_3$ in the catholyte stirring rate at 700 rpm. The black arrow and shaded area in (a) indicate the alkaline pH shift in the non-buffered Na_2SO_4 electrolyte.

We demonstrate that the kinetic behavior of the Cu/Cu_2O catalyst in the unbuffered Na_2SO_4 electrolyte presents more similarity to the alkalized one than to the PB at a set pH of 5.8. We reported that the NH_3 FEs from NO_3RR on the as-prepared Cu/Cu_2O are notably higher when employing non-buffered or alkalized Na_2SO_4 than for PB from −0.77 to −0.92 V *vs.* SHE (Figure 2.9b). This finding suggests that the rapid alkalinization of Na_2SO_4 non-buffered electrolyte (Figure A11) contributes to enhancing the catalyst performance for NO_3RR to NH_3. This facilitated alkalinization is associated with the different buffering capacity of both electrolytes at the electrode-electrolyte interface. This observation is corroborated by our detection of NH_2OH using *in-situ* FTIR (Figure 2.8), considering that its formation prior to NH_3 release is attributed to occur at alkaline pH.[35] By favoring the formation of NH_2OH, we can enhance the rates to produce NH_3, which is reflected by the FEs presented in Figure 2.9b.

The tendency of NO_3^- rate orders to produce NH_3 obtained for the Cu/Cu_2O catalyst in the unbuffered 0.5 mol L^{-1} Na_2SO_4 electrolyte mirrors the alkalized one, as shown in Figure 2.9c by the light and dark red lines respectively. Comparing the catalyst performance using PB (golden line) at pH 5.8 with sulfate-based electrolytes (red lines), we found significantly lower NO_3^- rate orders to NH_3 from −0.77 to −1.1 V *vs.* SHE. This finding means that the catalyst activity to NH_3 employing PB is less sensitive to increasing NO_3^- concentration. This trend can be attributed to both the pH effect and different anions' adsorption strength,[114] which is also pH-dependent.[115] Even when we plot those rate orders employing the RHE scale, as shown in Figure A12, the trends become even more different between them. We also detected a peak shift of the Cu_2O reduction in the absence of NO_3^- in the voltammetric profile of Cu/Cu_2O (dotted lines) from −0.6 to −0.9 V *vs.* SHE (Figure A13b) from Na_2SO_4 to PB electrolytes, red and yellow lines respectively.

2.4 Conclusions

Using a composite of Cu/Cu_2O as an electrocatalyst for NO_3RR to NH_3, our results unveil a novel potential dependence of different previously proposed active sites in the literature: oxygen vacancies and Cu^0 sites. Our kinetic analysis of differently reduced Cu/Cu_2O

suggested that within the range of −0.6 to −0.77 V *vs.* SHE, oxygen vacancies are the active sites for NO_3RR to NH_3. As we go to higher overpotentials (−1.1 V *vs.* SHE), pure metallic copper emerges as the active site for NO_3RR.

By employing *in-situ* spectroscopic characterizations, we found that Cu_2O reduces at −0.6 V *vs.* SHE and this reduction leaves oxygen vacancies in the catalyst lattice that promotes the formation of NH_2OH, an important precursor to NH_3. This intermediate is preferably formed in alkaline pHs, which is the case of our non-buffered electrolyte of 0.5 mol L^{-1} Na_2SO_4 since it is alkalized during NO_3RR. We found that this alkalinization led to an increased catalyst performance to produce NH_3, evidenced by higher FEs and NO_3^- rate orders compared to PB at fixed pH 5.8.

Our results also underscore the importance of coupling catalyst characterization, ideally *in-situ* or *operando*, with kinetic analysis to comprehend active sites for electrocatalytic reactions. Additionally, it is essential to employ meticulous control of the electrolyte's bulk pH, ideally measuring the local pH of the electrochemical interface to understand environmental conditions during electrochemical reactions.

Chapter 3. pH Influence on Cu Activity for Electrocatalytic Nitrate Reduction

This chapter is dedicated to presenting our studies on mechanistic insights into the pH-dependent copper intrinsic activity for nitrate electrochemical reduction. We conducted kinetic electrochemical and differential electrochemical mass spectrometry experiments to get some elucidative information about the pH influence on nitrate electrochemical reduction on copper.

3.1 Introduction

The electrolyte pH usually plays a crucial role in several electrochemical systems, especially in proton-consuming reactions. Considering that NO_3RR to NH_3 consumes 8 moles of H^+ per mole of NH_3, understanding the role of the electrolyte pH and identifying the proton source for this reaction is crucial to determine the best electrolyte conditions. Pérez-Gallent *et al*.[35] reported that there are different NO_3RR mechanisms on single crystalline Cu (100 and 111) for pHs 1 and 13. They found that in acidic media, HNO_2 is the first intermediate formed, followed by NO formation in solution, which absorbs on both Cu (100) and Cu (111) surfaces. NO_{ads} are then reduced to ammonium at the same potential for both single crystals. In alkaline media, they detected the formation of nitrite on both surfaces, being more favorable to occur at Cu (111). They also detected NH_2OH on both surfaces, being faster on Cu (100).[35]

In our work presented in Chapter 2, NO_3RR was performed initially in a slightly initially acidic sodium sulfate electrolyte,[32] and we detected the formation of NH_2OH and an alkaline shift on the initial pH on Cu/Cu_2O, related to the alkaline mechanism. Additionally, we found that Cu^0 is intrinsically active at higher overpotentials, overcoming the activity of Cu_2O-based catalysts (Figure 2.3a). Although the pH-dependent NO_3RR mechanisms on Cu were already studied at pHs 1 and 13, it is still poorly understood how mildly acid or basic pHs impact this reaction on such an important catalyst. In the work presented in this Chapter, we aim to evaluate from electrochemical experiments how the solution pH from 4.4 to 9.3 impacts the NO_3RR to NO_2^-. Using DEMS, we also established a pH influence on the product's distribution and how it dictates the mechanisms that NO_3RR can undergo. Thus, we could provide a picture of how this pH range from 4.4 to 9.3 can govern the NO_3RR mechanisms to NH_3 to elucidate crucial aspects of electrolyte engineering for this reaction.

3.2 Experimental Methods

3.2.1 Electrochemical Measurements

We performed CVs of NO_3RR on a Cu rod (0.196 cm^2) as a rotating disk electrode (RDE) from Pine Research (1600 rpm) varying the electrolyte pH using 0.2 mol L^{-1} $Na_xH_{3-x}PO_4$ mixing the salts NaH_2PO_4 (sodium phosphate monobasic dihydrate >98%, Sigma Aldrich) or Na_2HPO_4 (sodium phosphate dibasic heptahydrate >98%, Sigma Aldrich) to obtain solution pHs

of 4.4, 5.8, 7.1, 8.3 and 9.3, as shown in Figure 3.1. We conducted CVs from −0.2 to −1.2 V *vs.* SHE in the absence and presence of 0.05 mol L^{-1} $NaNO_3$.

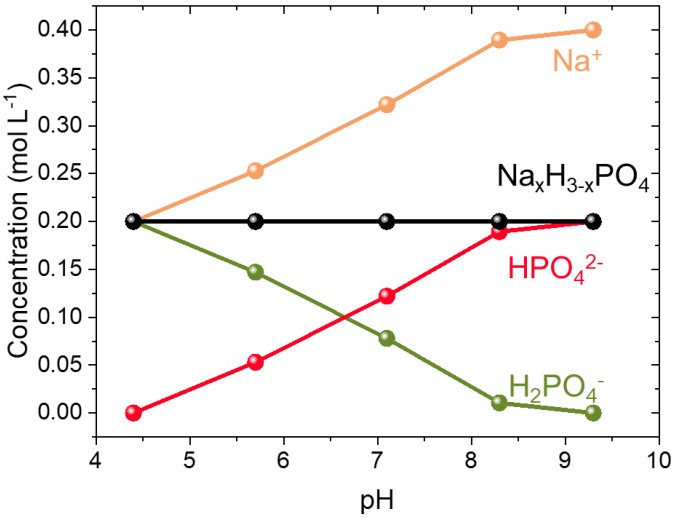

Figure 3.1. Ions' concentration and the solution pH of 0.2 mol L^{-1} $Na_xH_{3-x}PO_4$ (black line) electrolytes from pH 4.4 to 9.3.

We conducted potentiostatic chronoamperometric experiments in a two-compartment electrochemical cell separated by a Nafion 424 membrane. We used Ag/AgCl RE, a Pt plate as CE, and a previously electropolished Cu mesh (Alfa Aesar, copper gauze, 50 mesh woven from 0.23 mm diameter wire) as WE. The electropolishing protocol consisted of applying +3.0 V *vs.* another Cu mesh at the Cu mesh for 30 s using a 50% H_3PO_4 solution. We applied potentials from −0.1 to −0.8 V *vs.* SHE for 60 seconds for each measurement to obtain the steady-state current at each condition. The applied potentials were corrected *versus* SHE and RHE according to Eqs. 2.3 and 2.4.

The electrolyte consisted of 0.2 mol L^{-1} $Na_xH_{3-x}PO_4$ varying the quantities of NaH_2PO_4 or Na_2HPO_4 to obtain solution pHs of 4.4, 7.1, and 9.3, with and without the addition of 0.05 mol L^{-1} $NaNO_2$ or $NaNO_3$ in the catholyte, which was under magnetic stirring of 700 rpm. The pHs were measured after the experiments and did not change significantly.

3.2.2 Differential Electrochemical Mass Spectrometry Measurements

We performed *online* DEMS experiments to track the variation of the ionic current (I_{ionic}) of key mass/charge ratios (m/z) during potentiostatic chronoamperometric steps of 120 s each

from −1.4 to −1.7 V *vs.* SHE in duplicates. Between each step (120 s) and during the whole DEMS session, a potential of −0.6 V *vs.* SHE was kept in an electrochemical cell to maintain Cu in its metallic state, considering Cu can be oxidized in OCP. We monitored the I_{ionic} of m/z 2, 5, 17, 18, 28, 29, 30, 32, 33 and 44. The m/z 5 is monitored to verify if the baseline of all m/z is not being affected by differences in the pressure of the chamber, which was not the case. The I_{ionic} were normalized by the initial base line of each series of chronoamperometric experiments. The WE consisted of a Cu mesh (Alfa Aesar, copper gauze, 50 mesh woven from 0.23 mm diameter wire) positioned in a Teflon support underneath 4 poly(tetrafluoroethylene) (PTFE) membranes (Gore-Tex, 0.02 μm pore size, thickness of 50 μm), in which a stainless-steel flange (with a frit of 40 μm pore size) is screwed upon the PTFE membranes, that is connected to the DEMS chambers. The exposed geometric area was 0.38 cm^2. We used a custom-made electrochemical cell (Figure A14) with a Pt plate as CE and a leak-less Ag/AgCl as RE, under magnetic stirring at 700 rpm and Ar atmosphere. The electrolyte consisted of 0.2 mol L^{-1} NaH_2PO_4 or Na_2HPO_4 for pHs 4.4 or 9.3 respectively with the addition of 0.1 mol L^{-1} $NaNO_3$. The pHs were measured after the experiments and did not change significantly.

The DEMS equipment consists of a mass spectrometer with a vacuum system, powered by two turbomolecular pumps operating at 60,000 rpm (HIPACE 300 Turbopump DN 100 CF-F) and a mechanical pre-vacuum pump, two chambers, and valves.[116] We used a DEMS with two chambers that under operating conditions present a difference of pressure of up to 4 orders of magnitude (each one with a pressure in the order of 10^{-3} and 10^{-7} hPa). This pressure difference enables the differential detection of the gaseous and volatile species.[116] The mass spectrometer (PrismaPlus QMG 220 M1) is located in the second chamber and consists of a tungsten filament that ionizes the gaseous collected species that are detected by a secondary electron multiplier detector.

3.3 Results and Discussion

3.3.1 The Influence of pH in the Voltammetric Profile of NO_3RR on Cu

We compared the cathodic voltammetric profile of Cu RDE in the absence (Figure 3.2a) and the presence of 0.05 mol L^{-1} $NaNO_3$ (Figure 3.2b) for pHs from 4.4 to 9.3. Evaluating the cathodic voltammetric profile of NO_3RR at Cu RDE from pHs from 4.4 to 9.3 (Figure 3.2b), we can see a peak that is not detected in the absence of $NaNO_3$, which we attribute to NO_3RR.

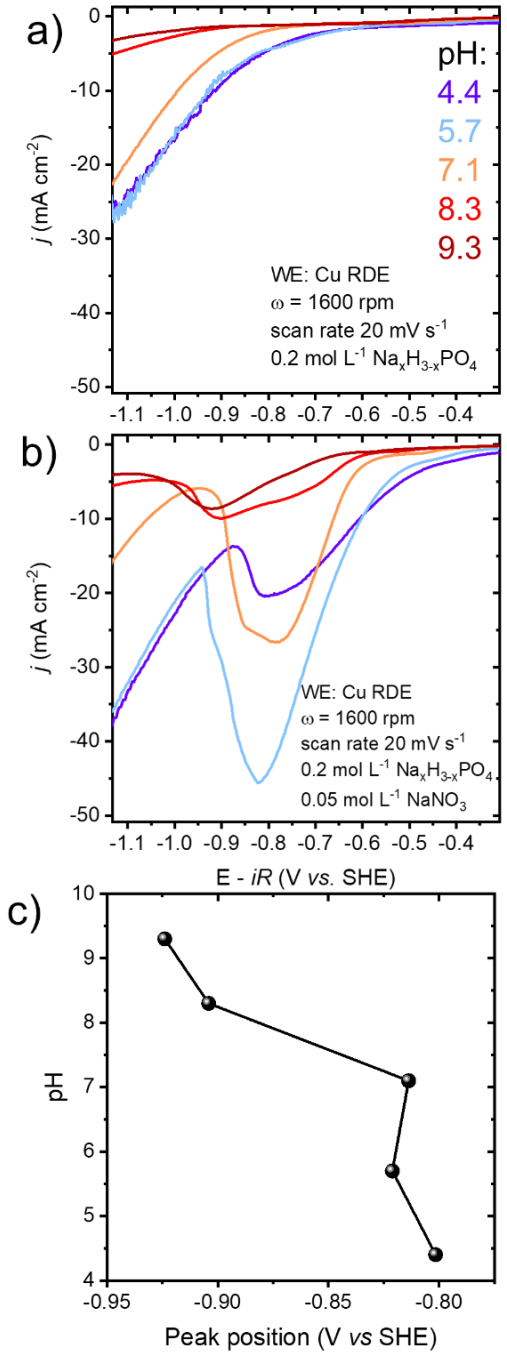

Figure 3.2. The fifth cathodic scans of CVs for Cu RDE recorded at different pHs in the absence (a) and presence (b) of 0.05 mol L^{-1} $NaNO_3$. Electrolyte containing 0.2 mol L^{-1} $Na_xH_{3-x}PO_4$ at pHs 4.4, 5.7, 7.1, 8.3 and 9.3, the scan rate of 20 mV s^{-1}, the rotation

rate of 1600 rpm, potential range between -0.2 and -0.8 V vs. RHE. (c) Evolution of the NO_3RR peak position in function of electrolyte pH.

We found that there is a peak shift to higher overpotentials with increasing electrolyte's pH (Figure 3.2c). At pH 4.4, there is a peak related to NO_3RR centered around −0.8 V *vs.* SHE, which shifts to a potential around −0.93 V *vs.* SHE for pH 9.3. At pHs 7.1 and 8.3, the peak attributed to NO_3RR presents two convoluted peaks in it. This profile suggests that increasing the electrolyte's pH shifts the reaction mechanism for NO_3RR for pHs lower to higher than 7.1. This increase in the overpotential for NO_3RR for pH also reflects the fact that this reaction depends on the concentration of protons since we are evaluating the CVs in the SHE scale. In the next subsection 3.3.2, we will explore how changing the pH impacts the NO_3RR in both SHE and RHE scales.

3.3.2 pH Influence on the NO_3RR to NO_2^-

We evaluated the pH influence on Cu intrinsic activity for NO_3RR and NO_2^- electrochemical reduction reaction (NO_2RR) by employing chronoamperometric experiments. In Figure 3.3, we show the comparison of the steady-state cathodic current of a Cu mesh from −0.1 to −0.8 V *vs.* SHE for HER with the electrolyte containing only $Na_xH_{3-x}PO_4$, NO_3RR and NO_2RR at different pHs (4.4, 7.1 and 9.3). For NO_3RR and NO_2RR, we present the steady-state overall current in the presence of 0.05 mol L^{-1} $NaNO_x$, which means that some activity is still related to the competing HER. Considering we cannot assume that HER will take place at the same rates in the presence and absence of NO_3^- or NO_2^-, we did not merely subtract the HER current in the absence of these anions from the overall current obtained in their presence. However, we could extract some elucidative trends that will be explored as follows. Additionally, the currents are expressed in their absolute values, and they are comparable considering we used the same size Cu mesh to do all the experiments.

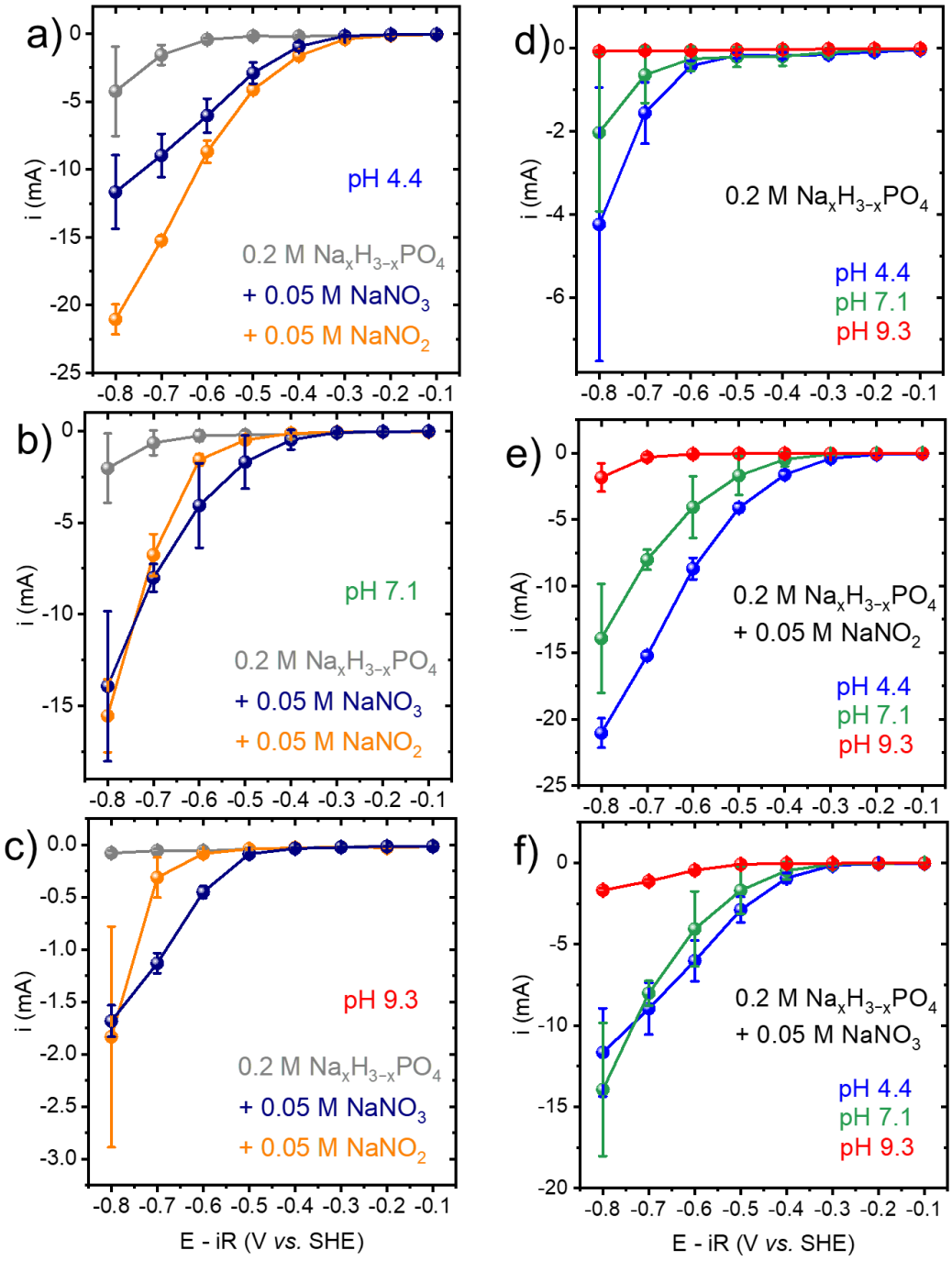

Figure 3.3. Potential dependence of the steady-state current of 1-minute chronoamperometric experiments conducted in different electrolytes using a copper mesh as WE. The electrolyte consists of 0.2 mol L^{-1} $Na_xH_{3-x}PO_4$ at pHs 4.4 (a), 7.1 (b) and 9.3 (c) with the absence (gray lines) and the presence of 0.05 mol L^{-1} $NaNO_3$ (navy

lines) or 0.05 mol L^{-1} $NaNO_2$ (orange lines). Figures d-f show the pH influence on the activity of Cu for the electrolyte containing 0.2 mol L^{-1} $Na_xH_{3-x}PO_4$ with the absence (d) and presence of 0.05 mol L^{-1} $NaNO_3$ (e) or 0.05 mol L^{-1} $NaNO_2$ (f). The experiments were conducted in a 2-compartment H-cell separated by a Nafion 424 membrane, saturated Ag/AgCl RE, and a Pt plate as CE under argon atmosphere. The catholyte was stirred at 700 rpm to minimize the mass transport limitation of the recorded currents. The error bars denote the standard deviation of at least two separate experiments.

We compare the cathodic currents of Cu at pHs 4.4 (Figure 3.3a), 7.1 (Figure 3.3b) and 9.3 (Figure 3.3c). in the absence (gray lines) and presence of NO_2^- (orange lines) and NO_3^- (navy lines). At pH 4.4 (Figure 3.3a), we see that the overall activity of Cu in the presence of NO_2^- is higher than in the presence of NO_3^- from −0.4 V *vs.* SHE to –0.8 V *vs.* SHE. This trend indicates that for these conditions of pH and potentials, NO_2RR is more kinetically favorable than NO_3RR. As we go to higher pHs, Cu activity for NO_3RR overcomes its activity for NO_2RR at lower overpotential (for pH 9.3, at –0.6 V and –0.7 V) indicating that NO_3RR becomes more kinetically favorable than the NO_2RR. At a higher overpotential (–0.8 V *vs.* SHE), the current in the presence of NO_2^- is similar to the one in the presence of NO_3^-, indicating that from this potential the NO_2RR starts to be more kinetically favored.

Considering all the reactions are proton-consuming, all of them should reflect a decreasing activity with increasing pH. This trend is valid for both HER (Figure 3.3d) and NO_2RR (Figure 3.3e), where we see that by increasing the pH, we lower their associated currents. When we exclude the influence of the concentration of protons by comparing their activity on the RHE scale (Figure 3.4), the activities of HER Figure 3.4a), NO_2RR (Figure 3.4a) are similar for all pHs, which means that the kinetics of these reactions are dictated by a proton/electron transfer process.[117]

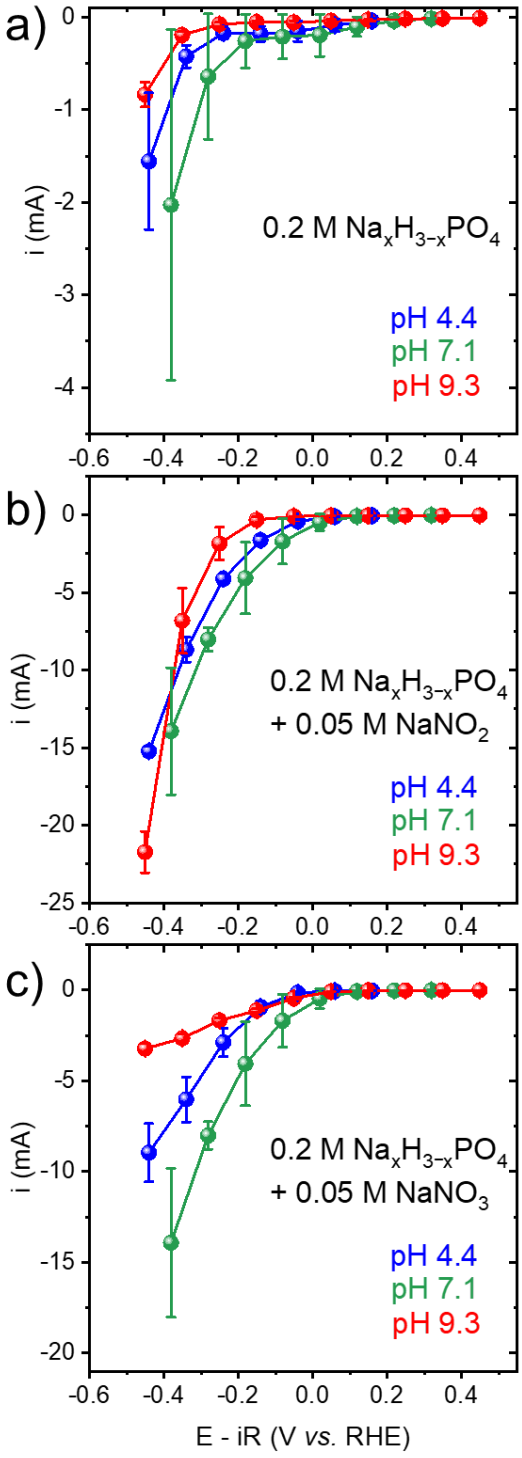

Figure 3.4. Potential dependence on RHE scale of the steady-state current of 1-minute chronoamperometric experiments conducted in different electrolytes using a copper

mesh as WE. pH influence on the activity of Cu for the electrolyte containing 0.2 mol L^{-1} $Na_xH_{3-x}PO_4$ with the absence (a) and presence of 0.05 mol L^{-1} $NaNO_3$ (b) or 0.05 mol L^{-1} $NaNO_2$ (c). The experiments were conducted under the same conditions as in Figure 3.3. The error bars denote the standard deviation of at least two separate experiments.

We do not see a clear pH dependence of Cu activities for NO_3RR on the SHE scale (Figure 3.3f), since they present similar profiles for pHs 4.4 and 7.1. It means that the reaction rate is not governed by a proton-electron transfer step, since it is not pH-sensitive. By excluding the influence of the protons' concentration (RHE scale), the NO_3RR (Figure 3.4c) is more favorable at pH 7.1. This can be explained by the fact that the mechanism path of the RDS for NO_3RR (NO_3^- adsorption and its reduction to NO_2^-) depends on the pH, which involves two proton transfers only when we employ an acidic electrolyte. Figure 3.5 shows different paths through which NO_3RR to $NO_2^-{}_{(ads)}$ can undergo depending on the pH.

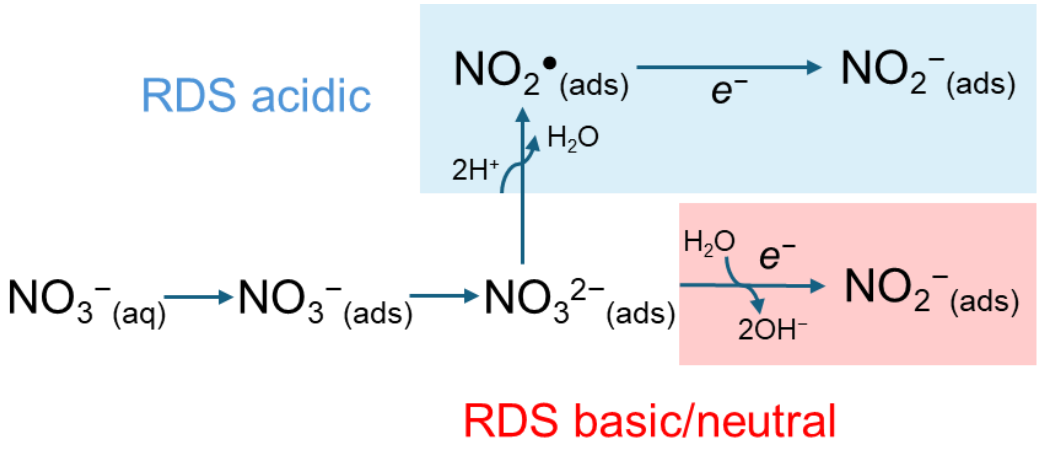

Figure 3.5. Scheme of the reaction mechanisms through which the nitrate reduction to nitrite can occur depending on the pH: acidic one highlighted in blue and neutral/alkaline one highlighted in red.

Considering the proposed mechanisms in Figure 3.5,[28] we suggest that the acidic RDS (highlighted in blue in Figure 3.5) is the main route for pH 4.4 and the basic/neutral RDS (highlighted in red in Figure 3.5) is the main one for pHs 7.1 and 9.3. By shifting the reaction mechanism from one that consumes protons (acidic path) to another one that consumes H_2O molecules (neutral/alkaline) producing OH^-, comparing only the pHs 7.1 and 9.3, the reaction is

more favorable at the lower one. We suggest that for pH 7.1 the lower concentration of OH^- species in solution favors their production, and the higher concentration of hydrogenophosphate (HPO_4^{2-}) at pH 9.3 (Figure 3.1) can hinder the adsorption of NO_3^-, which inhibits the NO_3RR activity of Cu at this pH.

3.3.3 Mechanistic Insights for the pH Influence on NO_3RR on Cu from DEMS

We employed DEMS (Figure 3.6) to track the formation of key gaseous products from NO_3RR on Cu electrode at pHs 4.4 (blue line) and pH 9.3 (red line) by evaluating the variation of the I_{ionic} related to the mass charge ratio (m/z) of those products or their fragments. We present in Figure 3.6a the steps of potential (120 seconds each) employed to qualitatively detect the potential-dependent production of N_2H_x (m/z = 29, Figure 3.6b), NO (m/z = 30, Figure 3.6c), N_2H_4 (m/z = 32, Figure 3.6d), NH_2OH (m/z = 32 and 33, Figure 3.6d-e), N_2O (m/z = 44, Figure 3.6f). We applied sufficiently negative potential to produce a detectable quantity of the volatile species, but it may not reflect the actual potential from which we started producing them. Our goal is to show the potential dependence of the production of each species from NO_3RR on Cu at different pHs (4.4 and 9.3).

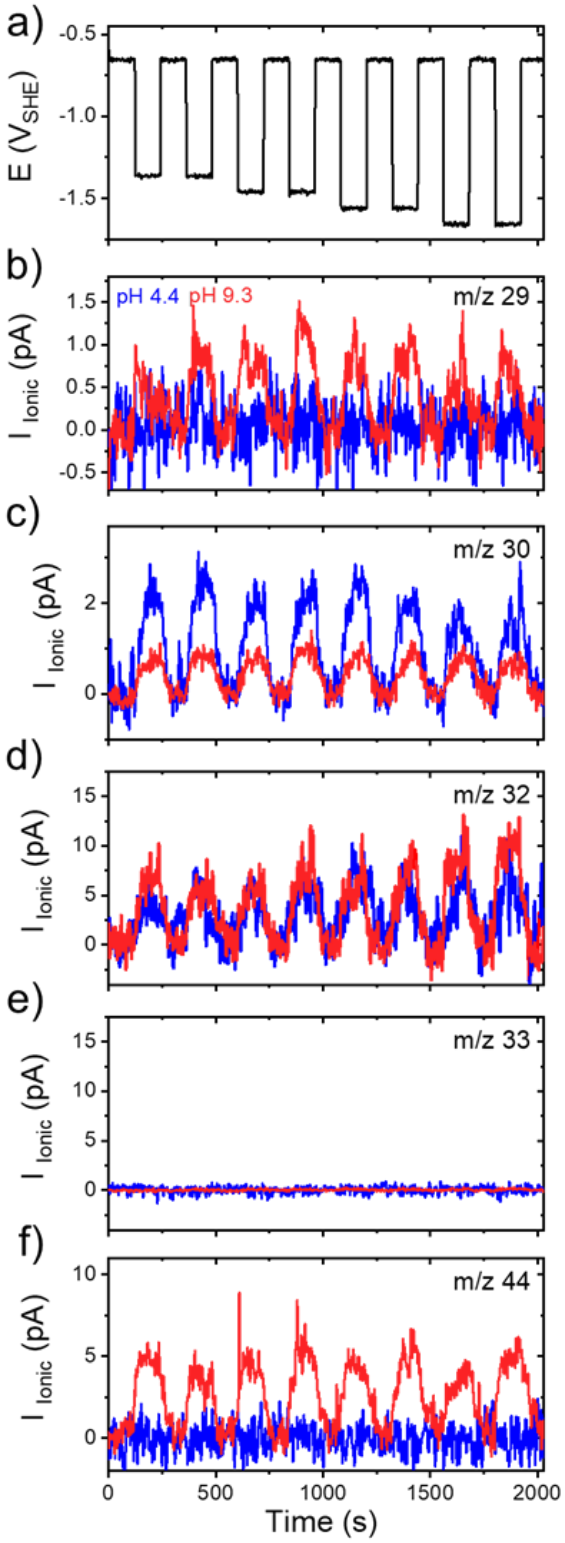

Figure 3.6. Differential Electrochemical Mass Spectrometry results. (a) Potential steps applied over time. Variation of ionic current related to m/z = 29 (b), 30 (c), 32 (d), 33

(e), 44 (f) for nitrate electrochemical reduction on Cu at pHs 4.4 (blue line) and 9.3 (red line). Experiments were conducted in a 1-compartment electrochemical cell containing 0.2 mol L^{-1} NaH_2PO_4 (pH 4.4) or Na_2HPO_4 (pH 9.3) + 0.1 mol L^{-1} $NaNO_3$, a Cu mesh as working electrode, Pt as counter electrode and a leak-less Ag/AgCl as reference electrode.

We tracked the formation of $NO_{(g)}$ by examining the variation of I_{ionic} of m/z = 30 (Figure 3.6c), which is a central intermediate of NO_3RR after the reduction of $NO_2^-{}_{(ads)}$. We observe that the potential-dependent increase of the I_{ionic} of m/z = 30 is higher at pH 4.4 than at pH 9.3. This finding suggests that the reduction of NO_2^- to $NO_{(ads)}$ (which can be desorbed and detected by DEMS) is more favorable at acidic pH, which corroborates our previous result (Figure 3.3a) and with what was found by Perez-Gallent *et al.*[35] at single crystal Cu at pH 1 compared to pH 13. The $NO_2^-{}_{(ads)}$ reduction to NO can undergo through different pathways, depending on the electrolyte pH, as Figure 3.7 schematizes.[14,28]

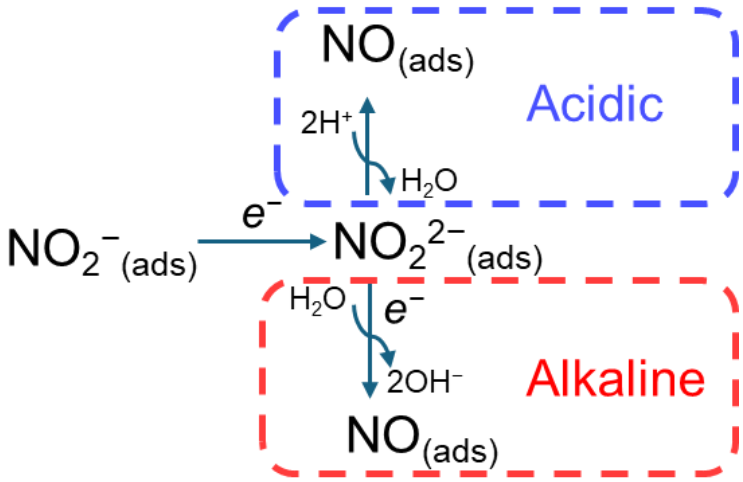

Figure 3.7. Scheme of the reaction mechanisms for nitrite conversion to NO at acidic (blue) and alkaline (red) pHs.

The $NO_2^-{}_{(ads)}$ species can be reduced to $NO_2^{2-}{}_{(ads)}$, consuming one electron.[14] Then, we can form NO through 2 protons-mediated reduction (acidic mechanism, in blue) or through the consumption of one H_2O molecule and one electron transfer (alkaline mechanism, in red).[14,35] Considering that the acidic path requires 1 electron while the alkaline one requires 2, the last one produces less NO per electron transferred. It is corroborated by the difference in the production of

NO at both pHs, which is more prominent at the acidic one. After the formation of $NO_{(ads)}$, a myriad of other products can be produced, as shown in Figure 1.4, and we also tracked the formation of the gaseous and volatile ones.

The m/z = 32 can be attributed to hydrazine (N_2H_4) and to a fragment of hydroxylamine (NH_2OH), whose main molecular fragment has a m/z equal to 33.[37] NH_2OH can be protonated to NH_3OH^+ at acidic pH with a pK_a equal to 5.93 (highlighted in green in Figure 1.4), which means that for pH = 4.4, we would not expect considerable amounts of NH_2OH in solution. We found a potential-dependent variation of I_{ionic} of m/z = 32 (Figure 3.6d) for both pHs, which can be attributed to both N_2H_4 and NH_2OH. However, considering that m/z = 33 (Figure 3.6e) does not vary at the same scale, and NH_2OH is not expected to be present in solution at pH 4.4 (pK_a = 5.93),[28] we attribute this variation to the formation of N_2H_4 through the protonation of $N_{2(ads)}$ species, as shown in the N-N coupling mechanisms in gray in Figure 1.4.[50] Although we do not attribute the variation of m/z = 32 to NH_2OH, we cannot state that it is not being formed during NO_3RR, considering that it is a soluble species that can be desorbed and/or quickly electrochemically converted into NH_3.[35] Besides that, our previous work detected the formation of hydroxylamine on Cu with *in-situ* Fourier transform infrared spectroscopy.[32] The formation of N_2H_x species is further confirmed by the potential-dependent variation of the I_{ionic} of m/z = 29, related to the fragment N_2H^+ (Figure 3.6b).

The N_2O can be formed through two different pathways (highlighted in light blue in Figure 1.4): by the coupling of two species $HNO_{(ads)}$ during NO_3RR leading to the formation of $H_2N_2O_2$ which dissociates releasing N_2O and H_2O and through the reaction of $H_2NOH_{(ads)}$ with $HNO_{2(aq)}$, as reported by Katsounaros and Kyriacou.[48] We tracked the formation of N_2O by probing the I_{ionic} related to m/z = 44 (Figure 3.6f). We found a potential-dependent formation of N_2O only for pH 9.3, which was not observed for pH 4.4. We attribute this side mechanism occurring at a more alkaline pH to the fact that $NHO_{(ads)}$ can be more rapidly protonated to form $NH_2O_{(ads)}$ at pH 4.4, inhibiting the formation of N_2O under this condition. We do not expect the formation of N_2O through the second mechanism (HNO_2-mediated one), considering that the pK_a of HNO_2 is equal to 3.4,[14] and it wouldn't be present in solution at both studied pHs.

We also probed the variation of I_{ionic} of m/z = 17 (Figure 3.8b), which can be attributed to both NH_3 and a fragment of H_2O, and m/z = 18 (Figure 3.8c) attributed to H_2O. Tracking I_{ionic}

of m/z = 18 (Figure 3.8b), we see that it varies more significantly with the applied potential only at pH 9.3. This difference can be attributed to the fact that the main source of protons for NO_3RR at pH 9.3 is water, unlike pH 4.4, in which case the m/z = 18 does not vary significantly with applying negative potential. We used for pH 4.4 a solution containing 0.2 mol L^{-1} NaH_2PO_4, while at pH 9.3 we used 0.2 mol L^{-1} Na_2HPO_4, which means that the cations' concentration is twice as high in pH 9.3 as in pH 4.4 (Figure 3.1). Thus, we can assume that $Na^+_{(aq)}$ species that move toward the electrode to stabilize the electrical field carry more H_2O molecules toward the Cu surface at pH 9.3 than at pH 4.4.[118] This finding suggests that H_2O is the main proton source for NO_3RR at pH 9.3. At more acidic pH, the proton transfer can be promoted either by $H^+_{(aq)}$ and $H_2PO_4^-{}_{(aq)}$ anions, which cannot be probed by DEMS, considering that these ions are not volatile species.

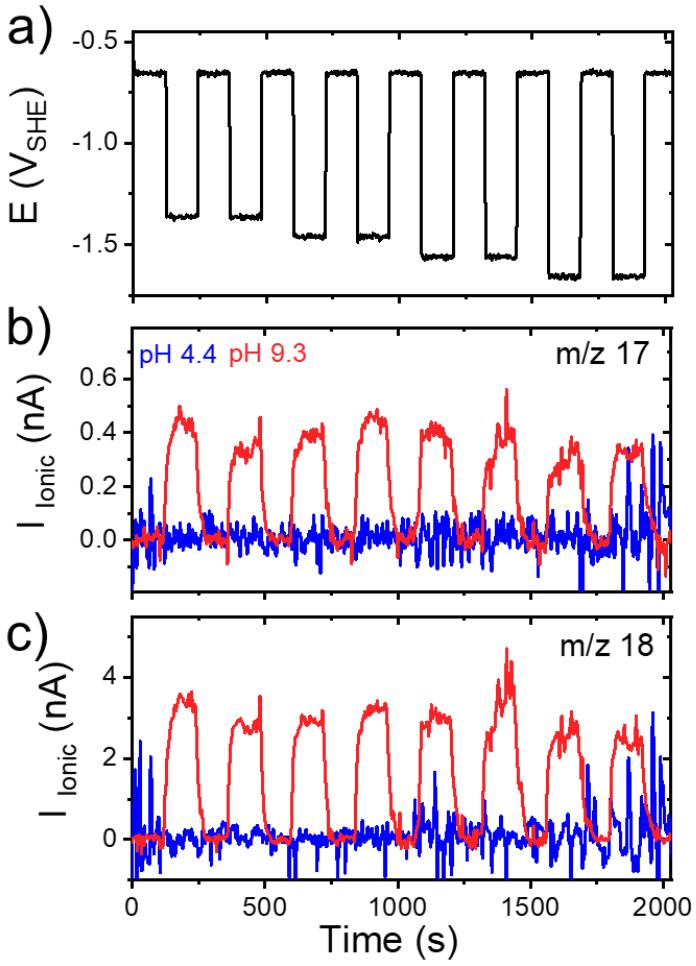

Figure 3.8. Differential Electrochemical Mass Spectrometry results. (a) Potential steps applied over time. Variation of ionic current related to m/z = 17 (b) and 18 (c) for nitrate

electrochemical reduction on Cu at pHs 4.4 (blue line) and 9.3 (red line). Experiments were conducted in a 1-compartment electrochemical cell containing 0.2 mol L^{-1} NaH_2PO_4 (pH 4.4) or Na_2HPO_4 (pH 9.3) + 0.1 mol L^{-1} $NaNO_3$, a Cu mesh as working electrode, Pt as counter electrode and a leak-less Ag/AgCl as reference electrode.

The I_{ionic} for m/z = 17 (Figure 3.8b) varies similarly as m/z = 18 (Figure 3.8c), signifying that the main source of fragments that impact the potential-dependent variation of m/z = 17 is H_2O. The pK_a of NH_3 to NH_4^+ is equal to 9.25,[28] which means that we would not expect to have considerable amounts of NH_3 in solution at pH 4.4, which corroborates the steadiness of this I_{ionic} at acid pH. Thus, we found that even though the m/z = 17 can also be attributed to the formation of NH_3,[62] it still confirms the expected for the studied pHs.

3.4 Conclusions

In the work presented in Chapter 3, we presented an experimental approach to explore the reaction mechanisms through which NO_3RR can undergo on metallic Cu depending on the electrolyte pH from 4.4 to 9.3. Comparing the electrochemical results obtained from HER, NO_2RR, and NO_3RR, we could establish the pH influence on the first steps of the NO_3RR to NO_2^-. We suggest that there are two different preferable mechanisms through which NO_3^- can be electrochemically converted into NO_2^-.

We also employed DEMS to unveil how the electrolyte pH can modulate the product distribution from NO_3RR on Cu, by tracking some key gaseous and volatile species. We found that $NO_{(ads)}$ is preferably formed at pH 4.4. At pH 9.3 more side products such as N_2O and N_2H_x can be formed, due to the lower concentration of protons that promotes the hydrogenation of oxygenated intermediates.

The results presented in Chapter 3 can stimulate the use of coupled techniques to explore electrolyte conditions for electrochemical reactions by shedding light on the role of mild pH conditions on NO_3RR on Cu electrodes. We highlight that electrolyte engineering is crucial to enable the use of electrochemical alternatives to both wastewater treatment and NH_3 synthesis.

Chapter 4. Summary and Outlook

This chapter is dedicated to summarizing the main conclusions of this thesis presenting the unanswered questions that it evokes. Some alternatives are proposed for addressing these questions through future research efforts.

4.1 Main Conclusions and Open Questions

In summary, in this thesis, we evaluate how different aspects of catalysts and electrolytes impact the NO_3RR. The work presented in Chapter 2 could successfully attribute the dependence on the applied potential of the active site for NO_3RR on Cu_2O-based catalysts, also shedding light on the dynamic nature of the catholyte pH under reaction conditions. We also could explore the pH-dependent NO_3RR paths by evaluating the kinetics of NO_3^- conversion into NO_2^- and probing the formation of gaseous products.

Our work suggested a meticulous and creative approach to evaluate different proposed active sites of Cu_2O-based catalysts for NO_3RR. We suggested the premise that different durations of an electrochemical pre-reduction step on a Cu/Cu_2O composite would lead to either a surface rich in oxygen vacancies (10 minutes of pre-reduction) or an oxide-derived Cu (10 hours of pre-reduction). Thus, we could evaluate how these pre-reduction steps led to different kinetic behaviors, i.e., different degrees of a previous reduction can modulate the activity of oxide-based catalysts for NO_3RR to NH_3. We hope that this type of approach can inspire future research on the activity of unstable oxides for electrochemical reduction reactions.

Although we have attributed the increased activity of Cu_2O-based catalysts at lower overpotentials to oxygen vacancies, we could not prove their existence in the catalyst lattice. Some proposals in the literature suggest the use of electron paramagnetic resonance (EPR) spectroscopy to assess oxygen vacancies in oxide materials.[119] However, EPR is not sufficient to distinguish different types of defects (cationic or anionic vacancies) and pits.[120] Thus, although we could not prove the presence of oxygen vacancies for 10 min-reduced Cu/Cu_2O, our results could explore the influence of the pre-reduction on the catalyst activity and hopefully will instigate future research to better address this question.

Our results presented in subsection 2.3.3 reveal that the structure of the Cu/Cu_2O composite changes with NO_3RR, by the reduction of Cu_2O during the electrolysis. Thus, the catalyst indeed modifies which possibly leads to oxygen vacancies on its lattice. However, it remains an open question of how we can properly probe these oxygen vacancies and their life during electrochemical reactions. Section 4.2 discusses some possible alternatives to better comprehend how the local environment of active Cu sites changes over electrochemical reactions.

For the results evaluating the pH dependence of NO_3RR mechanisms on Cu, we could confirm some hypothetical and/or experimentally proved mechanisms proposed in the literature,[35,51] as well as unveil some alternative routes that are first reported for Cu, such as the production of N_2O and N_2H_x. As previously mentioned, there is an intrinsic issue in employing phosphate buffers for electrochemical reactions: the fact that we end up varying the concentration of cations and different anions. Considering that both cations and anions can play an important role in electrocatalytic reactions,[33,121,122] it is hard to determine whether the differences that we report are due to the differences in the pH or to the different concentrations of Na^+, $H_2PO_4^-$ and/or HPO_4^{2-}. For this reason, we tried to carefully evaluate how the observed trends could be linked to different concentrations of protons and/or be influenced by the other ions present in the electrolyte solution.

Although the bulk pH can be kept constant by using buffered solutions, the interfacial pH can vary under reduction reaction conditions by the local consumption of protons.[34] It can lead to a pH gradient between the WE and the bulk of the electrolyte,[123] which is the critical region where the electrochemical reaction occurs. Section 4.2 will explore different alternatives that can be used to measure the local pH of an electrochemical interface.

4.2 Outlook for Future Research

Probing the presence and/or the formation of oxygen vacancies on oxide lattice is still a challenge for the field of catalysis.[120] EPR spectroscopy is a technique that probes paramagnetic samples, i.e., with an unpaired electron, which can adsorb the electromagnetic radiation under a certain magnetic field, following Eq. 4.1.[124]

$$h\nu = g\beta B \qquad \text{(Eq. 4.1)}$$

In Eq. 4.1 ‘h’ is the Planck constant, ‘ν’ is the frequency, ‘g’ is a constant that depends on the nature of the radical, ‘β’ is the Bohr magneton, and ‘B’ is the applied magnetic field. By evaluating the value of ‘g’, we would be able to probe oxygen vacancies, which is about 2.00, which is the information of unpaired electrons, for this type of radicals.[120] This type of conclusion still lacks evidence to properly attribute this measured quantity to oxygen vacancies. EPR indeed is sensitive to defects on an oxide lattice but cannot distinguish their type, whether such bond length increased or decreased, etc. Additionally, it is hard to determine whether the recorded signal comes from the surface of the catalyst or its bulk.[120]

To better address this challenge, the use of extended X-ray adsorption fine structure (EXAFS) spectroscopy can be an alternative to probe important information from the local coordination environment of a Cu atom from oxide catalysts.[125,126] EXAFS spectra of a material present oscillations that are related to constructive and destructive interferences between the scattered X-rays and their profile reflects information from the local coordination of the absorbing atom.[126,127] Thus, EXAFS is a powerful technique to investigate defects and extract the coordination number as well as the bond length of the probed atom. As we improve the technologies used by synchrotron facilities to acquire more EXAFS spectra per time, we can be able to extract real-time information on the existence and stability of oxygen vacancies in oxide catalysts.[128]

To probe the local pH during an electrochemical reaction, there are some alternatives that can be classified as direct (actual measurement of proton concentration) or indirect (probing species whose signal reflects the proton concentration).[34] The direct probing of local pH involves the electrochemical measurement of a potential that is attributable to the concentration of H^+. Among the techniques used to do so, we highlight the scanning probe microscopies, such as scanning electrochemical microscopy (SECM) and rotating ring-disk electrodes (RRDE). Among the indirect techniques, we highlight the use of infrared spectroscopy to probe the local pH.

Tefashe *et al.*[129] reported the use of a probe of Pt/IrO_2 to measure the local pH with SECM during the corrosion of magnesium. They obtained a spatial distribution of the local pH after 30 minutes of immersion in 0.01 mol L^{-1} NaCl. Using RRDE, Zimer *et al.*[130] measured the influence of the rotation rate on steady-state H_2O reduction current on Cu by probing the local pH with the ring coated with IrO_2. Recently, Corson *et al.*[131] reported the use of attenuated total reflectance-surface-enhanced infrared spectroscopy (ATR-SEIRAS) to probe the local pH of the interface between Cu and the electrolyte, which consists of a phosphate buffer system, for NO_3RR. They used the intensities of the peaks from the ATR-SEIRAS spectra attributed to H_3PO_4, $H_2PO_4^-$ and HPO_4^{2-} to determine the local pH during NO_3RR. Employing time-resolved ATR-SEIRAS, they found that the interfacial pH shifted from 2 to 7 in the first minute of operation. It suggests that this phenomenon can occur in our work presented in Chapter 3, which can be addressed by future works.

In summary, for future researchers who will rely on the investigation of the active catalytic sites and electrolyte pH conditions for NO_3RR, we strongly recommend considering the

use of coupled techniques such as the ones that were briefly introduced in this section. By employing them, we believe that the findings reported in this thesis could be either strengthened and/or improved. As the techniques are improved to get spatial and/or temporal resolved information from a catalytic reaction, electrochemists must be focused on expanding our knowledge about how electrochemical reactions occur, using those increasingly powerful tools to probe the electrode/electrolyte interface.

References

[1] J. W. Erisman, M. A. Sutton, J. Galloway, Z. Klimont, W. Winiwarter, *Nat Geosci* **2008**, *1*, 636–639.

[2] V. Smil, *Enriching the Earth: Fritz Haber, Carl Bosch, and the Transformation of World Food Production*, The MIT Press, **2000**.

[3] C. Smith, A. K. Hill, L. Torrente-Murciano, *Energy Environ Sci* **2020**, *13*, 331–344.

[4] F. Haber, "The Synthesis of Ammonia from Its Elements," **1920**.

[5] Carl Bosch, "The Development of the Chemical High Pressure Method During the Establishment of the New Ammonia Industry," **1932**.

[6] A. Mittasch, W. Frankenburg, **1950**, pp. 81–104.

[7] G. B. Taylor, T. H. Chilton, S. L. Handforth, *Ind Eng Chem* **1931**, *23*, 860–865.

[8] A. Nielsen, *Ammonia: Catalysis and Manufacture*, Springer, **1995**.

[9] "World population with and without synthetic nitrogen fertilizers," **n.d.**

[10] M. A. Sutton, D. Simpson, P. E. Levy, R. I. Smith, S. Reis, M. van Oijen, W. de Vries, *Glob Chang Biol* **2008**, *14*, 2057–2063.

[11] J. M. Melillo, *Ambio* **2021**, *50*, 759–763.

[12] S. Fields, *Environ Health Perspect* **2004**, *112*, DOI 10.1289/ehp.112-a556.

[13] National Academy of Engineering, *National Academy of Engineering Grand Challenges For Engineers*, **2017**.

[14] S. Garcia-Segura, M. Lanzarini-Lopes, K. Hristovski, P. Westerhoff, *Appl Catal B* **2018**, *236*, 546–568.

[15] I. Bogárdi, R. D. Kuzelka, W. G. Ennenga, Eds. , *Nitrate Contamination*, Springer Berlin Heidelberg, Berlin, Heidelberg, **1991**.

[16] W. L. Zhang, Z. X. Tian, N. Zhang, X. Q. Li, *Agric Ecosyst Environ* **1996**, *59*, 223–231.

[17] Z. Wang, D. Richards, N. Singh, *Catal Sci Technol* **2021**, *11*, 705–725.

[18] A. H. Mahvi, J. Nouri, A. A. Babaei, R. Nabizadeh, *International Journal of Environmental Science & Technology* **2005**, *2*, 41–47.

[19] J. F. Power, J. S. Schepers, *Agric Ecosyst Environ* **1989**, *26*, 165–187.

[20] P. H. van Langevelde, I. Katsounaros, M. T. M. Koper, *Joule* **2021**, *5*, 290–294.

[21] I. Katsounaros, *Curr Opin Electrochem* **2021**, *28*, DOI 10.1016/j.coelec.2021.100721.

[22] Y. Zeng, C. Priest, G. Wang, G. Wu, *Small Methods* **2020**, *4*, DOI 10.1002/smtd.202000672.

[23] N. Gruber, J. N. Galloway, *Nature* **2008**, *451*, 293–296.

[24] J. N. Galloway, J. D. Aber, J. W. Erisman, S. P. Seitzinger, R. W. Howarth, E. B. Cowling, B. J. Cosby, *Bioscience* **2003**, *53*, 341–356.

[25] Z. J. Schiffer, K. Manthiram, *Joule* **2017**, *1*, 10–14.

[26] N. Singh, B. R. Goldsmith, *ACS Catal* **2020**, *10*, 3365–3371.

[27] D. R. MacFarlane, P. V. Cherepanov, J. Choi, B. H. R. Suryanto, R. Y. Hodgetts, J. M. Bakker, F. M. Ferrero Vallana, A. N. Simonov, *Joule* **2020**, *4*, 1186–1205.

[28] D. Anastasiadou, Y. van Beek, E. J. M. Hensen, M. Costa Figueiredo, *Electrochemical Science Advances* **2022**, DOI 10.1002/elsa.202100220.

[29] A. J. Bard, L. R. Faulkner, H. S. White, *Electrochemical Methods Fundamentals and Applications*, John Wiley & Sons Ltd., **2022**.

[30] P. V. Kamat, *ACS Energy Lett* **2024**, *9*, 1053–1055.

[31] E. Roduner, *Catal Today* **2018**, *309*, 263–268.

[32] G. F. Costa, M. Winkler, T. Mariano, M. R. Pinto, I. Messias, J. B. Souza, I. T. Neckel, M. F. C. Santos, C. F. Tormena, N. Singh, R. Nagao, *Chem Catalysis* **2024**, 100850.

[33] M. C. O. Monteiro, F. Dattila, N. López, M. T. M. Koper, *J Am Chem Soc* **2022**, *144*, 1589–1602.

[34] M. C. O. Monteiro, M. T. M. Koper, *Curr Opin Electrochem* **2021**, *25*, 100649.

[35] E. Pérez-Gallent, M. C. Figueiredo, I. Katsounaros, M. T. M. Koper, *Electrochim Acta* **2017**, *227*, 77–84.

[36] G. Marcandalli, A. Goyal, M. T. M. Koper, *ACS Catal* **2021**, *11*, 4936–4945.

[37] M. T. De Groot, M. T. M. Koper, *Journal of Electroanalytical Chemistry* **2004**, *562*, 81–94.

[38] Y. Wang, C. Wang, M. Li, Y. Yu, B. Zhang, *Chem Soc Rev* **2021**, *50*, 6720–6733.

[39] E. Romeo, M. F. Lezana-Muralles, F. Illas, F. Calle-Vallejo, *ACS Appl Mater Interfaces* **2023**, *15*, 22176–22183.

[40] M. Teng, J. Ye, C. Wan, G. He, H. Chen, *Ind Eng Chem Res* **2022**, *61*, 14731–14746.

[41] Y. Wang, A. Xu, Z. Wang, L. Huang, J. Li, F. Li, J. Wicks, M. Luo, D. H. Nam, C. S. Tan, Y. Ding, J. Wu, Y. Lum, C. T. Dinh, D. Sinton, G. Zheng, E. H. Sargent, *J Am Chem Soc* **2020**, *142*, 5702–5708.

[42] D. Richards, S. D. Young, B. R. Goldsmith, N. Singh, *Catal Sci Technol* **2021**, *11*, 7331–7346.

[43] J. M. McEnaney, S. J. Blair, A. C. Nielander, J. A. Schwalbe, D. M. Koshy, M. Cargnello, T. F. Jaramillo, *ACS Sustain Chem Eng* **2020**, *8*, 2672–2681.

[44] G. F. Chen, Y. Yuan, H. Jiang, S. Y. Ren, L. X. Ding, L. Ma, T. Wu, J. Lu, H. Wang, *Nat Energy* **2020**, *5*, 605–613.

[45] K. Nakata, Y. Kayama, K. Shimazu, A. Yamakata, S. Ye, M. Osawa, *Langmuir* **2008**, *24*, 4358–4363.

[46] J. Li, G. Zhan, J. Yang, F. Quan, C. Mao, Y. Liu, B. Wang, F. Lei, L. Li, A. W. M. Chan, L. Xu, Y. Shi, Y. Du, W. Hao, P. K. Wong, J. Wang, S. X. Dou, L. Zhang, J. C. Yu, *J Am Chem Soc* **2020**, *142*, 7036–7046.

[47] A. C. A. de Vooys, G. L. Beltramo, B. van Riet, J. A. R. van Veen, M. T. M. Koper, *Electrochim Acta* **2004**, *49*, 1307–1314.

[48] I. Katsounaros, G. Kyriacou, *Electrochim Acta* **2008**, *53*, 5477–5484.

[49] H. Muhammad Adeel Sharif, H. Muhammad Farooq Khan, S. Ullah, Y. Wang, M. Ahmad, B. Yang, C. Li, M. Bilal Asif, *Journal of Energy Chemistry* **2024**, DOI 10.1016/j.jechem.2024.03.043.

[50] Y. Yao, S. Zhu, H. Wang, H. Li, M. Shao, *Angewandte Chemie International Edition* **2020**, *59*, 10479–10483.

[51] G. E. Dima, A. C. A. de Vooys, M. T. M. Koper, *Journal of Electroanalytical Chemistry* **2003**, *554–555*, 15–23.

[52] M. Duca, M. C. Figueiredo, V. Climent, P. Rodriguez, J. M. Feliu, M. T. M. Koper, *J Am Chem Soc* **2011**, *133*, 10928–10939.

[53] C. Roy, J. Deschamps, M. H. Martin, E. Bertin, D. Reyter, S. Garbarino, L. Roué, D. Guay, *Appl Catal B* **2016**, *187*, 399–407.

[54] J. Zhao, Z. Shen, J. Yu, Y. Guo, M. A. Mushtaq, Y. Ding, Z. Song, W. Zhang, X. Huang, Y. Li, D. Liu, X. Cai, *J Hazard Mater* **2022**, *439*, DOI 10.1016/j.jhazmat.2022.129653.

[55] D. Anastasiadou, Y. van Beek, W. Chen, T. Wissink, A. Parastaev, E. J. M. Hensen, M. Costa Figueiredo, *ChemCatChem* **2023**, *15*, DOI 10.1002/cctc.202201503.

[56] D. Reyter, D. Bélanger, L. Roué, *Journal of Physical Chemistry C* **2009**, *113*, 290–297.

[57] D. P. Butcher, A. A. Gewirth, *Nano Energy* **2016**, *29*, 457–465.

[58] J. Yuan, Z. Xing, Y. Tang, C. Liu, *ACS Appl Mater Interfaces* **2021**, *13*, 52469–52478.

[59] Z. Shen, J. Yan, M. Wang, L. Xing, B. Huang, H. Zhou, W. Li, L. Chen, J. Shi, *ACS Sustain Chem Eng* **2023**, DOI 10.1021/acssuschemeng.3c01514.

[60] T. Hu, M. Wang, L. Ren, C. M. Li, C. Guo, *J Phys Chem Lett* **2024**, *15*, 3258–3266.

[61] A. S. Fajardo, P. Westerhoff, C. M. Sanchez-Sanchez, S. Garcia-Segura, *Appl Catal B* **2021**, *281*, 119465.

[62] Y. Wang, W. Zhou, R. Jia, Y. Yu, B. Zhang, *Angewandte Chemie* **2020**, *132*, 5388–5392.

[63] H. Yin, X. Zhao, S. Xiong, Y. Peng, Z. Chen, R. Wang, M. Wen, J. Luo, H. Yamashita, J. Li, *J Catal* **2022**, *406*, 39–47.

[64] R. Daiyan, T. Tran-Phu, P. Kumar, K. Iputera, Z. Tong, J. Leverett, M. H. A. Khan, A. Asghar Esmailpour, A. Jalili, M. Lim, A. Tricoli, R. S. Liu, X. Lu, E. Lovell, R. Amal, *Energy Environ Sci* **2021**, *14*, 3588–3598.

[65] C. Li, S. Liu, Y. Xu, T. Ren, Y. Guo, Z. Wang, X. Li, L. Wang, H. Wang, *Nanoscale* **2022**, *14*, 12332–12338.

[66] Z. Song, Y. Liu, Y. Zhong, Q. Guo, J. Zeng, Z. Geng, *Advanced Materials* **2022**, *34*, DOI 10.1002/adma.202204306.

[67] N. Zhou, Z. Wang, N. Zhang, D. Bao, H. Zhong, X. Zhang, *ACS Catal* **2023**, 7529–7537.

[68] C. Wang, F. Ye, J. Shen, K. H. Xue, Y. Zhu, C. Li, *ACS Appl Mater Interfaces* **2022**, *14*, 6680–6688.

[69] T. Ren, Z. Yu, H. Yu, K. Deng, Z. Wang, X. Li, H. Wang, L. Wang, Y. Xu, *Appl Catal B* **2022**, *318*, 121805.

[70] J. Wang, H.-C. Chen, H.-Y. Tan, C. M. Tan, Y. Zhu, H. M. Chen, *ACS Appl Mater Interfaces* **2022**, *14*, 22681–22696.

[71] K. J. Vetter, *Zeitschrift für Elektrochemie, Berichte der Bunsengesellschaft für physikalische Chemie* **1959**, *63*, 1189–1191.

[72] G. Schmid, O. Delfs, *Die Autokatalytische Natur Der Kathodischen Reduktion von Salpetersaure Zu Salpetriger Siiure II. Der Galvanostatische Einschaltvorgang*, **1959**.

[73] E. Abel, H. Schmid, *Zeitschrift für Physikalische Chemie* **1928**, *136U*, 430–436.

[74] J. Wei, Y. Li, H. Lin, X. Lu, C. Zhou, Y. Li, *Environmental Science and Ecotechnology* **2024**, *20*, 100383.

[75] T. Hu, C. Wang, M. Wang, C. M. Li, C. Guo, *ACS Catal* **2021**, *11*, 14417–14427.

[76] T. Ren, K. Ren, M. Wang, M. Liu, Z. Wang, H. Wang, X. Li, L. Wang, Y. Xu, *Chemical Engineering Journal* **2021**, *426*, DOI 10.1016/j.cej.2021.130759.

[77] L. Bai, F. Franco, J. Timoshenko, C. Rettenmaier, F. Scholten, H. S. Jeon, A. Yoon, M. Rüscher, A. Herzog, F. T. Haase, S. Kühl, S. W. Chee, A. Bergmann, R. C. Beatriz, *J Am Chem Soc* **2024**, *146*, 9665–9678.

[78] M. Karamad, T. J. Goncalves, S. Jimenez-Villegas, I. D. Gates, S. Siahrostami, *Faraday Discuss* **2023**, *243*, 502–519.

[79] X. Zhang, Y. Wang, C. Liu, Y. Yu, S. Lu, B. Zhang, *Chemical Engineering Journal* **2021**, *403*, 126269.

[80] J. Zhao, L. Liu, Y. Yang, D. Liu, X. Peng, S. Liang, L. Jiang, *ACS Sustain Chem Eng* **2023**, *11*, 2468–2475.

[81] X. Fang, L. Tan, H. Luo, F. Jiang, H. Chen, *Colloids Surf A Physicochem Eng Asp* **2023**, *658*, 130678.

[82] Y. Chen, Y. Zhao, Z. Zhao, Y. Liu, *Mater Today Energy* **2022**, *29*, 101112.

[83] X. Wang, S. Qiu, J. Feng, Y. Tong, F. Zhou, Q. Li, L. Song, S. Chen, K. Wu, P. Su, S. Ye, F. Hou, S. X. Dou, H. K. Liu, G. Q. (Max) Lu, C. Sun, J. Liu, J. Liang, *Advanced Materials* **2020**, *32*, DOI 10.1002/adma.202004382.

[84] W. He, J. Zhang, S. Dieckhöfer, S. Varhade, A. C. Brix, A. Lielpetere, S. Seisel, J. R. C. Junqueira, W. Schuhmann, *Nat Commun* **2022**, *13*, 1129.

[85] Y. Xu, K. Ren, T. Ren, M. Wang, Z. Wang, X. Li, L. Wang, H. Wang, *Appl Catal B* **2022**, *306*, DOI 10.1016/j.apcatb.2022.121094.

[86] G. A. Cerrón-Calle, A. Wines, S. Garcia-Segura, *Appl Catal B* **2023**, *328*, 122540.

[87] M. R. Pinto, G. B. Pereira, A. C. Queiroz, R. Nagao, *Journal of Physical Chemistry C* **2020**, *124*, 12559–12568.

[88] M. R. Pinto, G. F. Costa, E. G. Machado, R. Nagao, *ChemElectroChem* **2020**, *7*, 2979–3005.

[89] J. Choi, B. H. R. Suryanto, D. Wang, H.-L. Du, R. Y. Hodgetts, F. M. Ferrero Vallana, D. R. MacFarlane, A. N. Simonov, *Nat Commun* **2020**, *11*, 5546.

[90] R. Y. Hodgetts, A. S. Kiryutin, P. Nichols, H.-L. Du, J. M. Bakker, D. R. Macfarlane, A. N. Simonov, *ACS Energy Lett* **2020**, *5*, 736–741.

[91] S. S. Biswas, A. Saha, M. Eswaramoorthy, *ACS Omega* **2022**, *7*, 1874–1882.

[92] A. C. Nielander, J. M. McEnaney, J. A. Schwalbe, J. G. Baker, S. J. Blair, L. Wang, J. G. Pelton, S. Z. Andersen, K. Enemark-Rasmussen, V. Čolić, S. Yang, S. F. Bent, M. Cargnello, J. Kibsgaard, P. C. K. Vesborg, I. Chorkendorff, T. F. Jaramillo, *ACS Catal* **2019**, *9*, 5797–5802.

[93] M. Kolen, W. A. Smith, F. M. Mulder, *ACS Omega* **2021**, *6*, 5698–5704.

[94] W. Zheng, L. Zhu, Z. Yan, Z. Lin, Z. Lei, Y. Zhang, H. Xu, Z. Dang, C. Wei, C. Feng, *Environ Sci Technol* **2021**, acs.est.1c02278.

[95] R. A. Vicente, S. P. Raju, H. V. N. Gomes, I. T. Neckel, H. C. N. Tolentino, P. S. Fernández, *Anal Chem* **2023**, DOI 10.1021/acs.analchem.3c02695.

[96] S. J. A. Figueroa, A. Rochet, I. Ferreira Torquato, A. M. Espíndola, H. Rigamonti, B. C. Meyer, G. de M. Azevedo, *Radiation Physics and Chemistry* **2023**, *212*, 111198.

[97] B. T. Kitagaki, M. R. Pinto, A. C. Queiroz, M. C. Breitkreitz, F. Rossi, R. Nagao, *Physical Chemistry Chemical Physics* **2019**, *21*, 16423–16434.

[98] J. A. Switzer, G. Hodes, *MRS Bull* **2010**, *35*, 743–750.

[99] S. J. Kim, S. Kim, J. Lee, Y. Jo, Y. S. Seo, M. Lee, Y. Lee, C. R. Cho, J. pil Kim, M. Cheon, J. Hwang, Y. I. Kim, Y. H. Kim, Y. M. Kim, A. Soon, M. Choi, W. S. Choi, S. Y. Jeong, Y. H. Lee, *Advanced Materials* **2021**, *33*, DOI 10.1002/adma.202007345.

[100] R. Kas, K. Yang, D. Bohra, R. Kortlever, T. Burdyny, W. A. Smith, *Chem Sci* **2020**, *11*, 1738–1749.

[101] S. Jung, C. C. L. McCrory, I. M. Ferrer, J. C. Peters, T. F. Jaramillo, *J Mater Chem A Mater* **2016**, *4*, 3068–3076.

[102] Q. Hu, Y. Qin, X. Wang, H. Zheng, K. Gao, H. Yang, P. Zhang, M. Shao, C. He, *CCS Chemistry* **2022**, *4*, 2053–2064.

[103] T. J. Frankcombe, Y. Liu, *Chemistry of Materials* **2023**, *35*, 5468–5474.

[104] S. Gao, Z. Sun, W. Liu, X. Jiao, X. Zu, Q. Hu, Y. Sun, T. Yao, W. Zhang, S. Wei, Y. Xie, *Nat Commun* **2017**, *8*, DOI 10.1038/ncomms14503.

[105] J. Vavra, G. P. L. Ramona, F. Dattila, A. Kormányos, T. Priamushko, P. P. Albertini, A. Loiudice, S. Cherevko, N. Lopéz, R. Buonsanti, *Nat Catal* **2024**, *7*, 89–97.

[106] Y. Deng, A. D. Handoko, Y. Du, S. Xi, B. S. Yeo, *ACS Catal* **2016**, *6*, 2473–2481.

[107] J. A. van Bokhoven, C. Lamberti, *X-Ray Absorption and X-Ray Emission Spectroscopy: Theory and Applications*, **2015**.

[108] A. Gaur, D. Shrivastava, K. Joshi, in *J Phys Conf Ser*, Institute Of Physics Publishing, **2009**.

[109] A. A. Guda, S. A. Guda, A. Martini, A. N. Kravtsova, A. Algasov, A. Bugaev, S. P. Kubrin, L. V. Guda, P. Šot, J. A. van Bokhoven, C. Copéret, A. V. Soldatov, *NPJ Comput Mater* **2021**, *7*, 203.

[110] H. Liu, X. Lang, C. Zhu, J. Timoshenko, M. Rüscher, L. Bai, N. Guijarro, H. Yin, Y. Peng, J. Li, Z. Liu, W. Wang, B. R. Cuenya, J. Luo, *Angewandte Chemie - International Edition* **2022**, *61*, DOI 10.1002/anie.202202556.

[111] D. Reyter, D. Bélanger, L. Roué, *Electrochim Acta* **2008**, *53*, 5977–5984.

[112] M. Jiang, Q. Zhu, X. Song, Y. Gu, P. Zhang, C. Li, J. Cui, J. Ma, Z. Tie, Z. Jin, *Environ Sci Technol* **2022**, *56*, 10299–10307.

[113] J. Zhou, F. Pan, Q. Yao, Y. Zhu, H. Ma, J. Niu, J. Xie, *Appl Catal B* **2022**, *317*, DOI 10.1016/j.apcatb.2022.121811.

[114] M. C. Santos, D. W. Miwa, S. A. S. Machado, *Electrochem commun* **2000**, *2*, 692–696.

[115] M. H. Hasan, I. T. McCrum, *Angewandte Chemie International Edition* **2024**, *63*, DOI 10.1002/anie.202313580.

[116] S. J. Ashton, *Design, Construction and Research Application of a Differential Electrochemical Mass Spectrometer (DEMS)*, Springer Berlin Heidelberg, Berlin, Heidelberg, **2012**.

[117] J. Resasco, Y. Lum, E. Clark, J. Z. Zeledon, A. T. Bell, *ChemElectroChem* **2018**, *5*, 1064–1072.

[118] L. D. Chen, M. Urushihara, K. Chan, J. K. Nørskov, *ACS Catal* **2016**, *6*, 7133–7139.

[119] C. Drouilly, J.-M. Krafft, F. Averseng, S. Casale, D. Bazer-Bachi, C. Chizallet, V. Lecocq, H. Vezin, H. Lauron-Pernot, G. Costentin, *The Journal of Physical Chemistry C* **2012**, *116*, 21297–21307.

[120] K. Ye, K. Li, Y. Lu, Z. Guo, N. Ni, H. Liu, Y. Huang, H. Ji, P. Wang, *TrAC Trends in Analytical Chemistry* **2019**, *116*, 102–108.

[121] M. C. O. Monteiro, M. F. Philips, K. J. P. Schouten, M. T. M. Koper, *Nat Commun* **2021**, *12*, 4943.

[122] M. C. O. Monteiro, F. Dattila, B. Hagedoorn, R. García-Muelas, N. López, M. T. M. Koper, *Nat Catal* **2021**, *4*, 654–662.

[123] H. Ooka, M. C. Figueiredo, M. T. M. Koper, *Langmuir* **2017**, *33*, 9307–9313.

[124] M. J. Davies, *Methods* **2016**, *109*, 21–30.

[125] S. Peng, X. Han, L. Li, S. Chou, D. Ji, H. Huang, Y. Du, J. Liu, S. Ramakrishna, *Adv Energy Mater* **2018**, *8*, DOI 10.1002/aenm.201800612.

[126] I. Rossetti, L. Sordelli, P. Ghigna, S. Pin, M. Scavini, L. Forni, *Inorg Chem* **2011**, *50*, 3757–3765.

[127] A. J. Dent, *Top Catal* **2002**, *18*, 27–35.

[128] L. Liu, N. Milas, A. H. C. Mukai, X. R. Resende, F. H. De Sá, *J Synchrotron Radiat* **2014**, *21*, 904–911.

[129] U. M. Tefashe, P. Dauphin-Ducharme, M. Danaie, Z. P. Cano, J. R. Kish, G. A. Botton, J. Mauzeroll, *J Electrochem Soc* **2015**, *162*, C536–C544.

[130] A. M. Zimer, M. Medina da Silva, E. G. Machado, H. Varela, L. H. Mascaro, E. C. Pereira, *Anal Chim Acta* **2015**, *897*, 17–23.

[131] E. R. Corson, J. Guo, W. A. Tarpeh, *J Electrochem Soc* **2024**, *171*, 046503.

Appendix

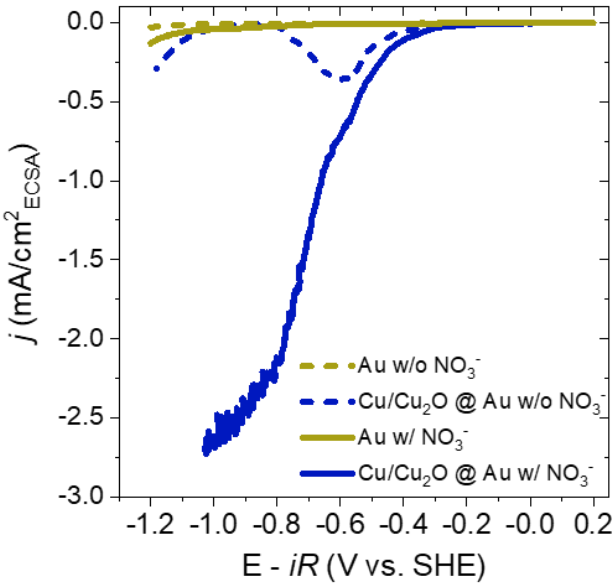

Figure A1. Linear sweep voltammetries conducted from 0.2 to −1.2 V vs. SHE, scan rates of 20 mV s^{-1} for Au substrate (golden lines) and Cu/Cu_2O catalyst (blue lines). Electrolyte containing 0.5 mol L^{-1} Na_2SO_4 in the presence (solid lines) and absence (dotted lines) of 0.05 mol L^{-1} $NaNO_3$.

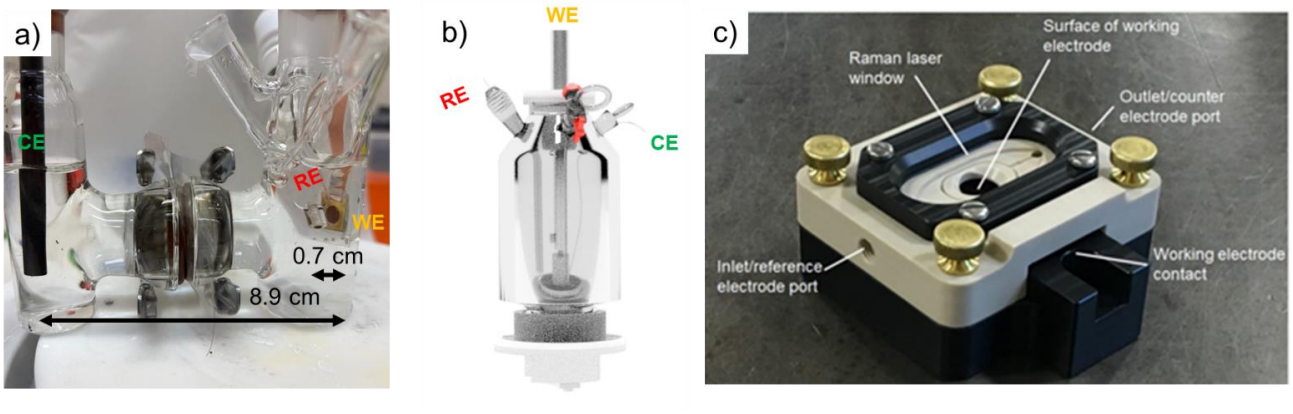

Figure A2. Photos of the electrochemical cells, including labels for their elements: WE for working electrode, RE for reference electrode, and CE for counter electrode. (a) 2-compartment electrochemical cell employed for kinetic experiments. (b) Spectro-electrochemical cell for *in-situ* FTIR. (c) Spectro-electrochemical cell for *in-situ* Raman spectroscopy measurements.

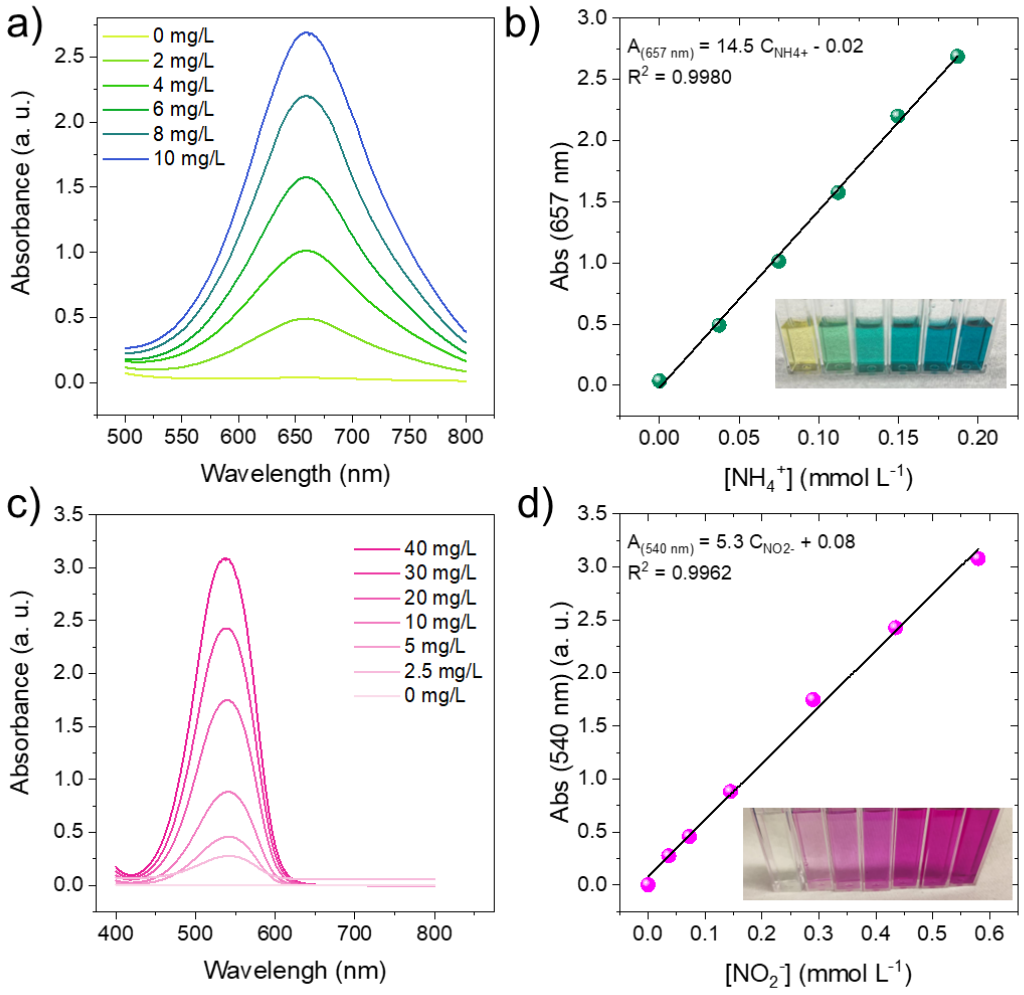

Figure A3. UV-Vis spectra of (a) NH_3 and (c) NO_2^- quantifications. Linear regression for (b) NH_3 and (d) NO_2^- with the relationship between maximum absorbance and product concentration.

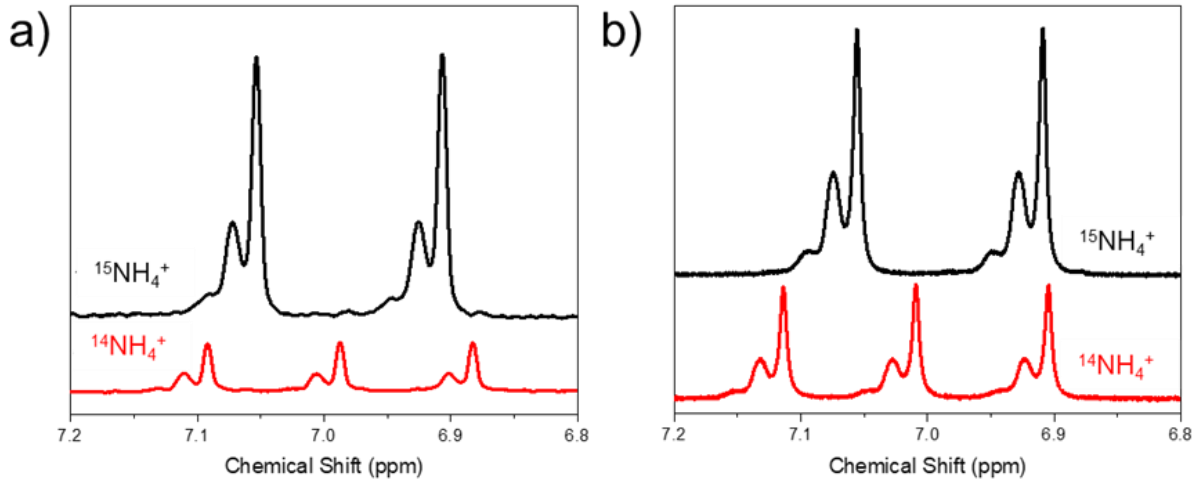

Figure A4. ^{1}H NMR spectra for $^{15}NH_4^+$ at δH 6.98 (d, 73.2 Hz) (black curve) and $^{14}NH_4^+$ at δH 6.97 (t, 52.3 Hz) (red curve) obtained after 1 h electrolysis in 0.5 mol L^{-1} Na_2SO_4 and (a) 2.4 mmol L^{-1} and (b) 24 mmol L^{-1} of $^{15}NaNO_3$ and $^{14}NaNO_3$, respectively, at −0.8 V vs. SHE.

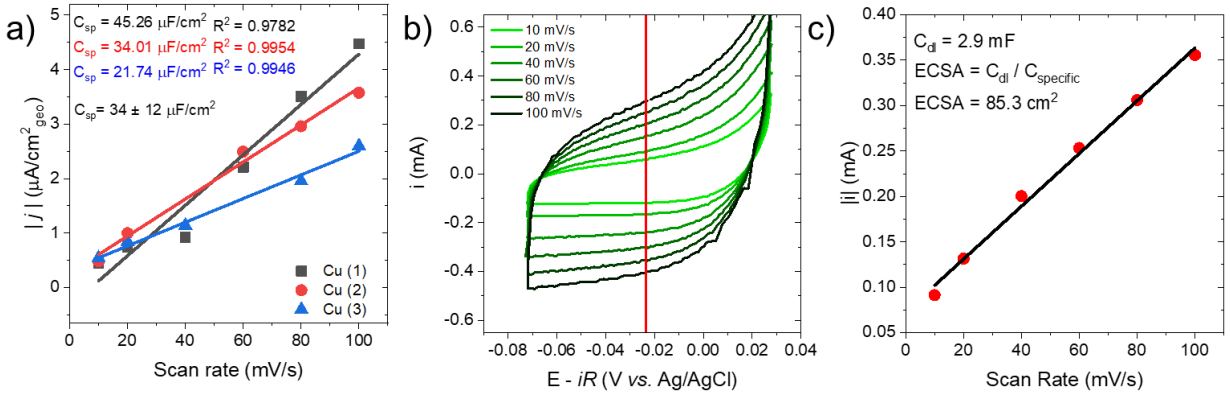

Figure A5. Electrochemically active surface area (ECSA) measurements. (a) Metallic flat Cu specific capacitance measurements. (b) Cyclic voltammetries of Cu/Cu_2O catalyst at different scan rates (10 to 100 mV s^{-1}). Electrolyte containing 0.5 mol L^{-1} Na_2SO_4. Red line indicates the capacitive double-layer current that was used for the (c) linear relationship (black line) for the modulus of the average of double-layer current and the scan rate.

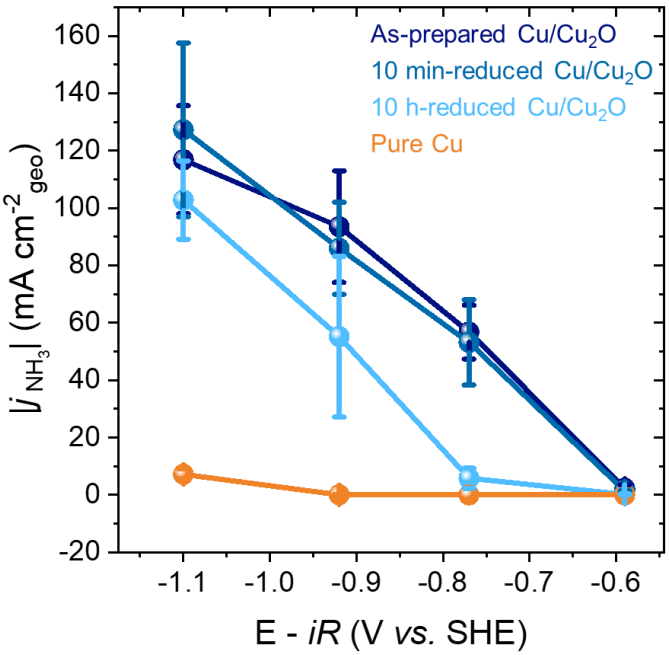

Figure A6. NH_3 partial current densities normalized by geometric areas for as-prepared, 10 min-reduced and 10 h-reduced Cu/Cu_2O (shades of blue) and pure Cu (orange). The results were obtained from 10 minutes of potentiostatic electrolysis with the catalyst as WE, graphite rod as CE and Ag/AgCl as RE, electrolyte containing 0.5 mol L^{-1} Na_2SO_4 adding 0.05 mol L^{-1} $NaNO_3$ in the catholyte.

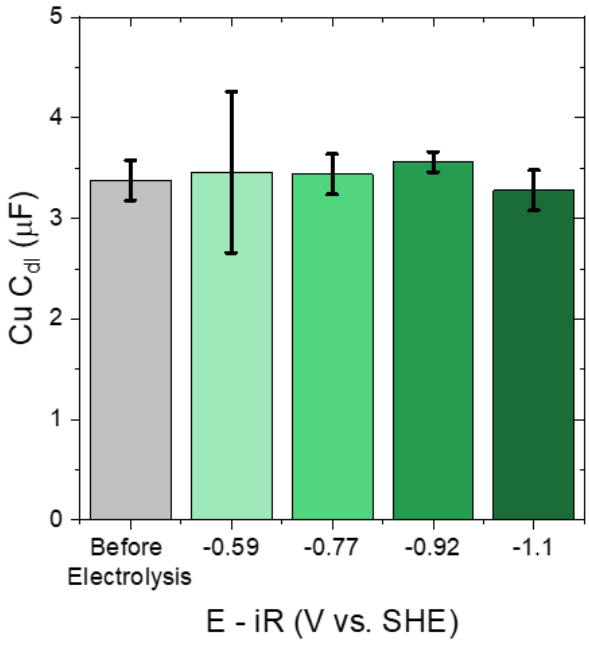

Figure A7. Cu double-layer capacitance (C_{dl}) before (gray bar) after electrolysis at different applied potentials. Electrolyte containing 0.5 mol L^{-1} Na_2SO_4 and 0.05 mol L^{-1} $NaNO_3$.

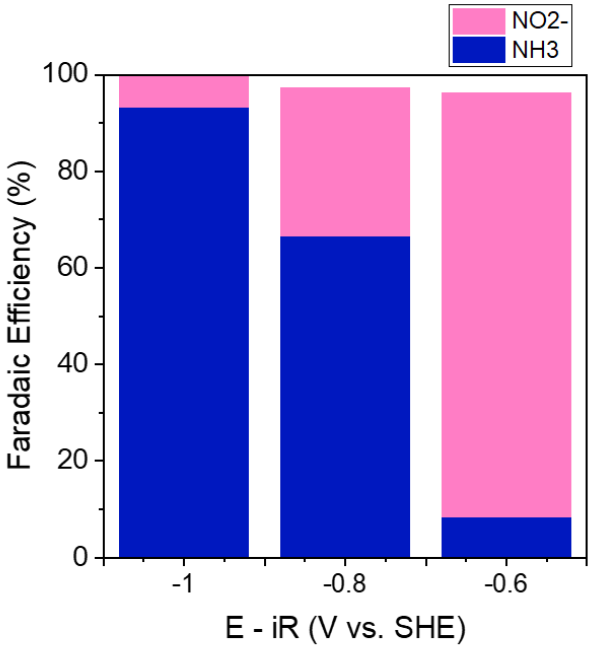

Figure A8. Faradaic efficiencies towards nitrite (pink) and ammonia (blue) obtained from 10 min-electrolysis with [$NaNO_3$] = 50 mmol L^{-1} for as-prepared Cu/Cu_2O composite. Data extracted from chronoamperometric electrolysis for 10 minutes with electrolyte containing 0.5 mol L^{-1} Na_2SO_4 (pH_0 = 5.8) and stirred at 700 rpm.

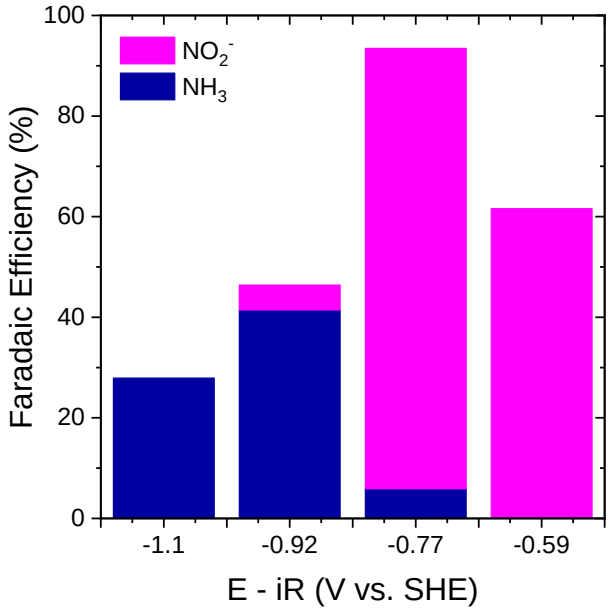

Figure A9. Faradaic efficiencies toward nitrite (pink) and ammonia (blue) obtained from 10 min-electrolysis with [$NaNO_3$] = 50 mmol L^{-1} for pure metallic copper. Data extracted from chronoamperometric electrolysis for 10 minutes with electrolyte containing 0.5 mol L^{-1} Na_2SO_4 (pH_0 = 5.8) and stirred at 700 rpm.

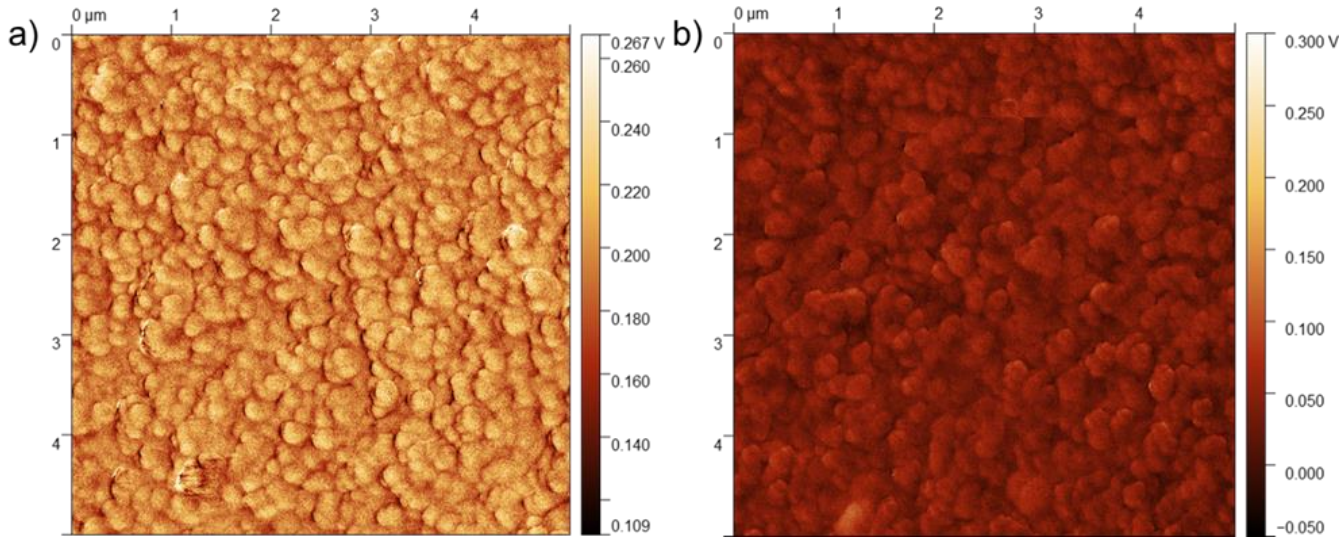

Figure A10. Surface contact potential maps recorded with Kelvin Probe AFM for the Cu/Cu_2O before (a) and after (b) NO_3RR. Electrolysis conditions: 1h-electrolysis at −0.77 V vs. SHE; electrolyte containing 0.5 mol L^{-1} Na_2SO_4 and catholyte with addition of 2.35 mmol L^{-1} $NaNO_3$.

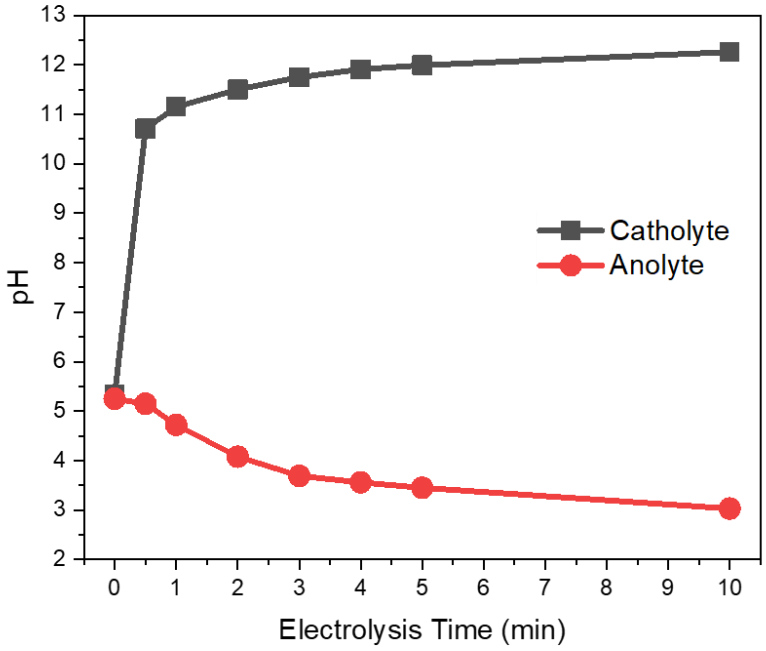

Figure A11. Evolution of electrolyte (catholyte and anolyte) pHs over the time for an electrolysis at −0.93 V vs. SHE. Electrolyte containing 0.5 mol L^{-1} Na_2SO_4 and catholyte with 0.05 mol L^{-1} $NaNO_3$.

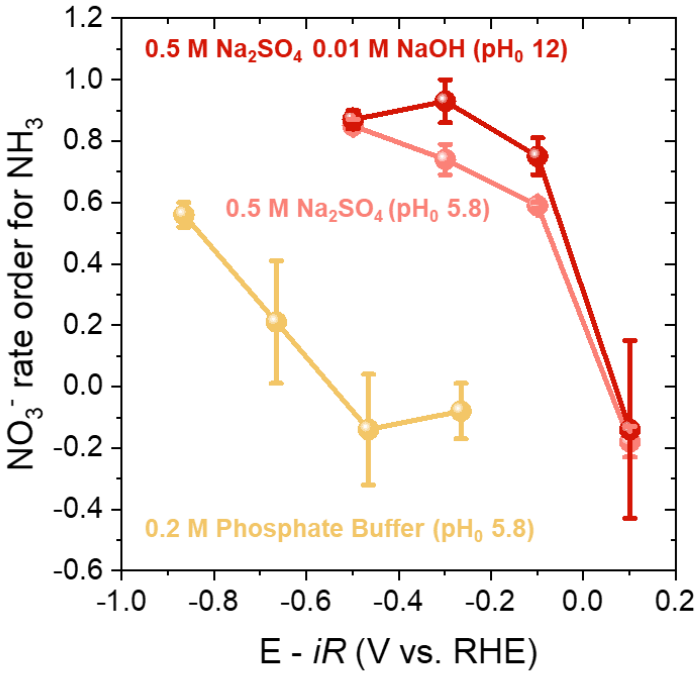

Figure A12. Relationship between nitrate rate orders for ammonia production and applied potential (in V vs. RHE) for alkalized (dark red), non-buffered (light red) 0.5 mol L^{-1} sodium sulfate, and 0.2 mol L^{-1} phosphate buffer (yellow) electrolytes. Data extracted from chronoamperometric using the as-prepared Cu/Cu_2O catalyst as working electrode for 10-min electrolysis varying [NO_3^-] from 5 to 50 mmol L^{-1}, stirred at 700 rpm.

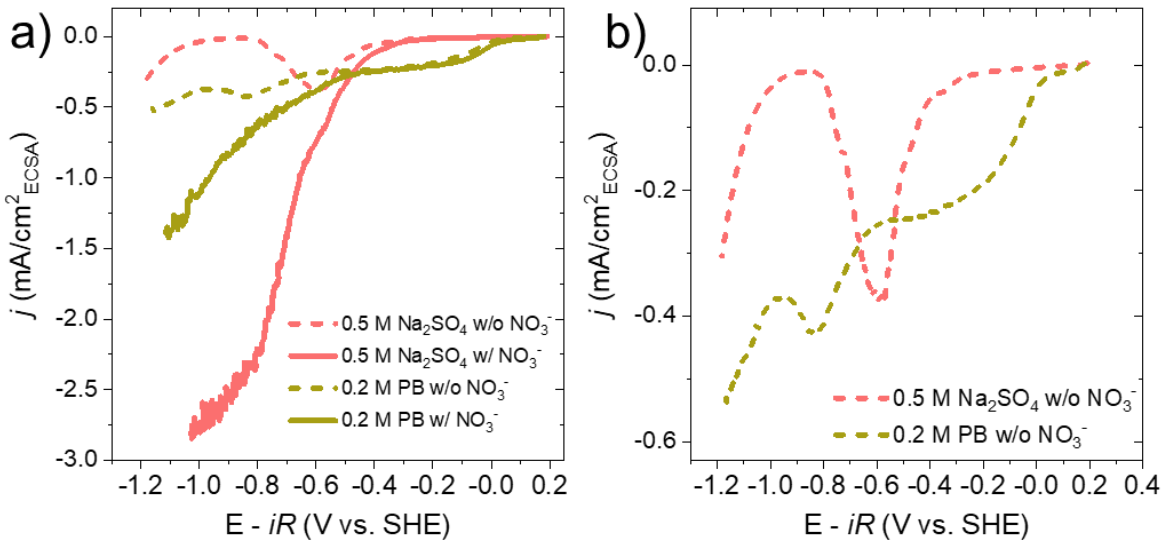

Figure A13. (a) Voltammetries from 0.2 to −1.2 V vs. SHE, scan rates of 20 mV s^{-1} for non-buffered (light red) 0.5 mol L^{-1} sodium sulfate, and 0.2 mol L^{-1} phosphate buffer (yellow) electrolytes the presence (solid lines) and absence (dashed lines) of 0.05 mol L^{-1} $NaNO_3$. (b) Zoom of voltammetries region to identify peaks related to Cu_2O reduction.

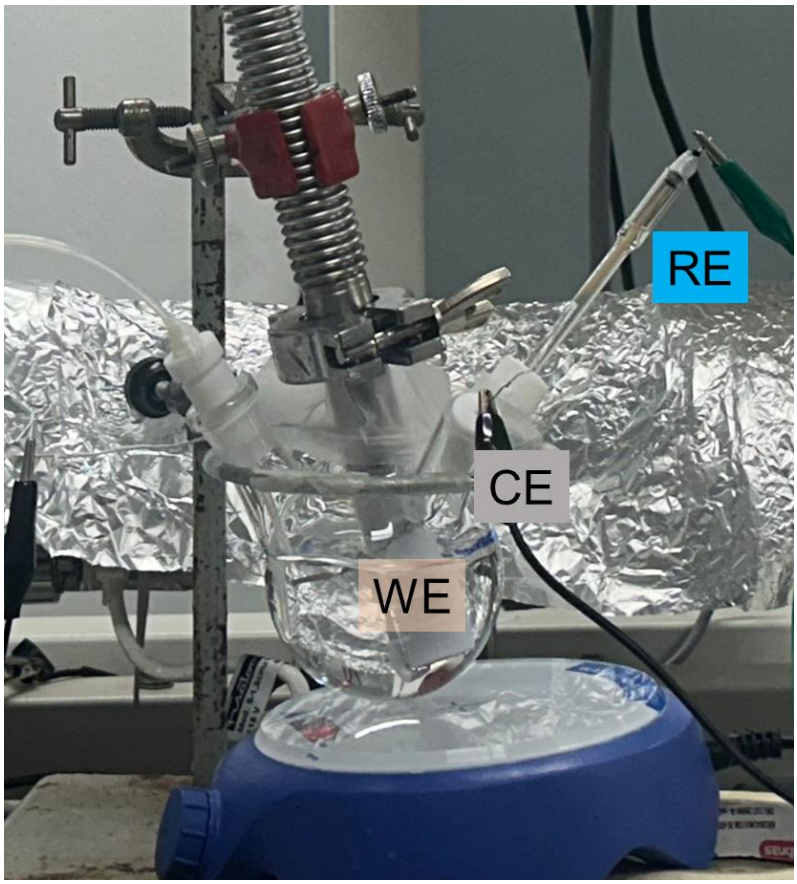

Figure A14. Photo of the electrochemical cell used for DEMS experiments indicating its components.

Gabriel Floriano Costa

+55 (19) 99737-5713 | gabrielflorianocosta@gmail.com

ORCID Google Scholar

EDUCATION

2019 – 2024	**PhD in Physical-Chemistry, *in progress*** *University of Campinas*, UNICAMP, Campinas, Brazil *Thesis:* On the activity of copper-based materials for electrocatalytic nitrate reduction to ammonia *Supervisor:* Raphael Nagao de Sousa. Grantee of the São Paulo Research Foundation, FAPESP, Brazil
2022 – 2023	**PhD internship abroad** *University of Michigan*, Ann Arbor, U. S. A. *Supervisor:* Nirala Singh *Project:* Ammonia electrosynthesis from nitrate reduction: flow cell and *in-situ* Raman spectroscopic studies Grantee of the São Paulo Research Foundation, FAPESP, Brazil
2015 – 2019	**Bachelor of Chemistry** *University of Campinas*, UNICAMP, Campinas, Brazil
2018 – 2019	**Undergraduate Internship** *Brazilian Nanotechnology National Laboratory*, Campinas, Brazil *Supervisor:* Renato S. Lima *Project:* Development of microfluidic electrochemical sensors.

SUMMARY

- Experience with DEMS, *in-situ* Raman and XANES spectroscopies, RDE, flow-cell reactors, electrochemical sensors, and Li-oxygen batteries.
- 5 accepted articles in peer-reviewed journals and 8 attendances in scientific conferences.
- 1-year experience as a graduate student instructor for undergraduate courses.
- 4 Reviewer activities for the *Journal of Energy Chemistry.*

PUBLICATIONS

1. **Costa, G. F.;** Winkler, M.; Mariano, T.; Pinto M. R.; Messias I.; Souza Jr. J. B. S.; Neckel I.; Santos M. F. C.; Tormena C. F.; Singh, N.; Nagao R. Identifying the active site of Cu/Cu_2O for electrocatalytic nitrate reduction reaction to ammonia. *Chem Catalysis* **2024**, 100850.

2. Messias, I.; Winkler, M.; **Costa, G. F.;** Mariano, T.; Souza Jr. J. B. S.; Neckel I.; Figueiredo, M.C.; Singh, N.; Nagao R. The role of structural and compositional changes of Cu_2O nanocubes in nitrate electroreduction to ammonia. *Under review.*

3. Parma, E.; **Costa, G. F.;** Nagao, R. Modeling Li-Ion Battery Voltage Oscillations and the Impact of Exchange Current Density on Oscillation Properties. *The Journal of Physical Chemistry C,* **2022,** *126*, *29*, 11900-11906.

4. Pinto, M. R.; **Costa, G. F**.; Machado, E. G.; Nagao, R. Self-organization in Electrochemical Synthesis as a Methodology towards New Materials. *ChemElectroChem* **2020**, *7*, 2979. (FRONT COVER)

5. Silva, G. S.; Oliveira, L. P.; **Costa, G. F.*;** Giordano, G. F.; Nicoliche, C. Y. N.; Silva, A. A.; Khan, L. U.; Silva, G. H.; Gobbi, A. L.; Silveira, J. V.; Filho, A. G. S.; Schleder, G. R.; Fazzio, A.; Martinez, D. S. T.; Lima, R. S. Ordinary Microfluidic Electrodes Combined with Bulk Nanoprobe Produce Multidimensional Electric Double-layer Capacitances Towards Metal Ion Recognition. *Sensors and Actuators B: Chemical*, **2020,** *305*, 127482. ***Shared first authorship.**

6. Nicoliche, C. Y. N.; **Costa, G. F.,** Gobbi, A. L.; Shimizu, F. M.; Lima, R. S. Pencil Graphite Core for Pattern Recognition Applications. *Chemical Communications,* **2019**, *32,* 4623-4626.

COURSES

- **ISE Satellite Student Regional Symposium on Electrochemistry and Paulo Teng An Sumodjo School of Electrochemistry**, organized by Chemistry Institute of the University of São Paulo, USP (30 h) – December 2021. *Online.*

- **Ricardo Rodrigues School of Synchrotron Light (ER2LS),** organized by Brazilian Synchrotron Light Laboratory (LNLS), from National Center for Research in Energy and Materials, CNPEM (72 h) – July 2021. *Online.*

CONFERENCES

Oral presentations:

- **Costa, G. F.;** Winkler, M.; Mariano, T.; Pinto M. R.; Messias I.; Souza Jr. J. B. S.; Neckel I.; Santos M. F. C.; Tormena C. F.; Singh, N.; Nagao R. Identifying the Active Site of Cu/Cu_2O for Electrocatalytic Nitrate Reduction Reaction to Ammonia with in-situ Spectroscopies. **33rd LNLS Annual User's Meeting (RAU).** Campinas/SP – Brazil. November 2024.
- **Costa, G. F.;** Winkler, M.; Mariano, T.; Pinto M. R.; Messias I.; Souza Jr. J. B. S.; Neckel I.; Santos M. F. C.; Tormena C. F.; Singh, N.; Nagao R. Identifying the Active Site of Cu/Cu_2O for Electrocatalytic Nitrate Reduction Reaction, **24th Simpósio Brasileiro de Eletroquímica e Eletroanalítica.** Porto Alegre/RS – Brasil, October 2023
- **Costa, G. F.;** Pinto, M. R.; Messias, I; Junior, J; Singh, N.; Nagao, R. Tracking Copper Oxidation State during Nitrate Electrochemical Reduction Reaction. **243rd ECS Meeting**. Boston/MA, U.S.A. May 2023
- **Costa, G. F.;** Pinto, M. R.; Messias, I; Junior, J; Singh, N.; Nagao, R. The role of Cu/Cu_2O Composite in Nitrate Electrochemical Reduction: an *in-situ* Investigation. **44th Annual Spring Symposium of The Michigan Chapter of the North American Catalysis Society.** Ann Arbor/MI, U.S.A. May 2023

Poster presentations:

- **Costa, G. F.;** Winkler, M.; Mariano, T.; Pinto M. R.; Messias I.; Souza Jr. J. B. S.; Neckel I.; Santos M. F. C.; Tormena C. F.; Singh, N.; Nagao R. On the activity of Cu-based materials for electrocatalytic nitrate reduction to ammonia. **MATSUS Spring 2024 Conference.** Barcelona – Spain, March 2024.
- **Costa, G. F.;** Pinto, M. R.; Messias, I; Nagao, R., Ammonia Synthesis via Nitrate Electrochemical Reduction at Cu/Cu_2O. **23rd Simpósio Brasileiro de Eletroquímica e Eletroanalítica,** 2021, Online.
- **Costa, G. F.;** Machado, E.; Carpanedo, T. Anchieta, C.; Doubek, G.; Nagao, R. Seeking for Electrochemical Instabilities in Lithium-oxygen Batteries Using Halides as Redox Mediator. **239th ECS Meeting**, 2021, Online.
- **Costa, G. F.;** Machado, E.; Carpanedo, T. Anchieta, C.; Doubek, G.; Nagao, R. Electrochemical Instabilities in Lithium-oxygen Batteries: The Role Redox Mediator. **71st Annual Meeting of the International Society of Electrochemistry.** 2020, Online.